Novel Radionuclides for Theranostics at the Bern Medical Cyclotron

Inaugural dissertation
of the Faculty of Science,
University of Bern

presented by

Gaia Dellepiane

from Italy

Supervisor of the doctoral thesis:
Prof. Dr. Saverio Braccini

Albert Einstein Center for Fundamental Physics
Laboratory for High Energy Physics

Novel Radionuclides for Theranostics at the Bern Medical Cyclotron

Inaugural dissertation
of the Faculty of Science,
University of Bern

presented by

Gaia Dellepiane

from Italy

Supervisor of the doctoral thesis:
Prof. Dr. Saverio Braccini

Albert Einstein Center for Fundamental Physics
Laboratory for High Energy Physics

Accepted by the Faculty of Science.

Bern, 20.03.2023

The Dean
Prof. Dr. Marco Herwegh

Contents

Introduction

Physics has always played a predominant role in the development of modern medicine. Since the discovery of X-rays by Wilhelm Conrad Röntgen and of radioactivity by Henri Bequerel and Marie Curie in the late 19th century, ionizing radiations have been increasingly applied in the diagnosis and treatment of oncological diseases. In particular, radioactive isotopes are used in nuclear medicine to label biologically active molecules that are injected into the patient for diagnostic or therapeutic purposes.

The birth of nuclear medicine dates back to 1913, when George de Hevesy carried out the first study on animals and plants using natural radioisotopes as tracers. The number of radionuclides available with possible application in medicine grew rapidly with the invention of the cyclotron in 1930 by Ernest Lawrence, which made possible their artificial production.

In 1936 at the University of California, Berkley, John Lawrence administered to a 28-year-old woman suffering from leukaemia a dose of ^{32}P produced with the cyclotron developed by his brother Ernest. This was the first time that a cyclotron-produced radioisotope was used to treat a human patient and set the stage for targeted radionuclide therapy.

Today, more than 40 million nuclear medicine procedures are performed each year and, according to the International Atomic Energy Agency (IAEA), in 2021 there were more than 1300 cyclotron facilities worldwide dedicated to the production of radionuclides.

Over the last few decades, research in medical applications of physics and nuclear medicine has focused on the development of radiopharmaceuticals that enable the combination of diagnostics and targeted therapy, using radionuclides suitable for both purposes or radioisotope pairs with identical or very similar chemical characteristics.

This new approach, called theranostics from the crasis of therapy and diagnostics, allows to monitor simultaneously the disease development, the radiation distribution in the organ of interest, and the treatment effectiveness. The possibility of predicting whether a patient will benefit from the therapy is the basis of personalized nuclear medicine. For this to be possible, the availability of novel radionuclides in quantity and quality suitable for clinical applications is of paramount importance and represents an actual scientific challenge.

One of the best solutions is the cyclotron irradiation of solid targets, which constitutes the motivation for this PhD work.

The experiments reported in this thesis were performed at the Bern medical cyclotron laboratory in the framework of the project 'PHOtonuclear Reaction (PHOR): Breakthrough Research in Radionuclides for Theranostics', funded by the Swiss National Science Foundation (Grant CRSII5 180352). This project is based on the collaboration between the Albert Einstein Centre (AEC) - Laboratory for High Energy Physics (LHEP), the Department of Chemistry, Biochemistry and Pharmacy (DCBP) of the University of Bern and the Swiss Federal Institute of Metrology (METAS).
The results obtained in this PhD work also involved the collaboration between AEC-LHEP, the Paul Scherrer Institute (PSI) and the Institute of Radiation Physics (IRA) of the Lausanne University Hospital (CHUV).

This thesis consists of a first monographic part divided into three chapters and a second part in which some selected publications I authored are reprinted.

In the first chapter, radiopharmaceuticals are briefly introduced, focusing on the physical and nuclear characteristics that radionuclides intended for diagnostic and therapeutic applications must have. A description of the theranostic approach and an overview of the most promising radionuclides for this purpose are also provided.
In the second chapter, the Bern medical cyclotron laboratory is presented, focusing on the 18 MeV cyclotron and its out-ports for research purposes, namely the Beam Transport Line (BTL) and the Solid Target Station (STS), the latter connected to the cyclotron through a novel magnetic device for beam focusing. The main instruments used for the experiments are introduced, together with the methodologies for measuring the beam energy, the cross sections and for determining the production yield. These methods and the respective instrumentation were developed by our group with my contribution. In particular, this chapter describes a method I elaborated to disentangle the different nuclear contributions from the production cross section when a radionuclide is produced by more than one reaction.
The third chapter is devoted to the novel medical radionuclides that I studied at the Bern medical cyclotron. I investigated several of the main theranostic and non-standard radioisotopes that can be produced with an 18 MeV medical cyclotron with solid targets. These include the widely used diagnostic radionuclides ^{68}Ga and ^{99m}Tc, the promising SPECT radioisotope ^{155}Tb, the therapeutic ^{165}Er and ^{167}Tm and the theranostic pairs ^{61}Cu/^{67}Cu, ^{64}Cu/^{67}Cu and ^{44}Sc/^{47}Sc. This chapter reports in particular on the cross section measurements of the nuclear reactions involved, which are of paramount importance for the optimization of radioisotope production. The studies performed on the basis

of these measurements are also described, which made it possible to determine the experimental conditions that maximize the radionuclide yield and purity. Finally, the results of the first production tests are presented.
This first part is complemented by an appendix, where unpublished cross section results are reported.

In the second part, the following selected publications, of which I am the first author or a co-author, are reprinted:

1. **G. Dellepiane**, P. Casolaro, C. Favaretto, P. V. Grundler, I. Mateu, P. Scampoli, Z. Talip, N. P. van der Meulen and S. Braccini, *Cross section measurements of terbium radioisotopes for an optimized ^{155}Tb production with an 18 MeV medical PET cyclotron*, Applied Radiation and Isotopes, 184 (2022); 110175.

2. S. Braccini, T. S. Carzaniga, **G. Dellepiane**, P. V. Grundler, P. Scampoli, N. P. van der Meulen and D. Wüthrich, *Optimization of ^{68}Ga production at an 18 MeV medical cyclotron with solid targets by means of cross section measurements of ^{66}Ga, ^{67}Ga and ^{68}Ga*, Applied Radiation and Isotopes, 186 (2022); 110252.

3. **G. Dellepiane**, P. Casolaro, I. Mateu, P. Scampoli, N. Voeten and S. Braccini, *^{47}Sc and ^{46}Sc cross section measurements for an optimized ^{47}Sc production with an 18 MeV medical PET cyclotron*, Applied Radiation and Isotopes, 189 (2022); 110428.

4. **G. Dellepiane**, P. Casolaro, I. Mateu, P. Scampoli, N. Voeten and S. Braccini, *Cross section measurements for an optimized ^{61}Cu production at an 18 MeV medical cyclotron from natural Zn and enriched ^{64}Zn solid targets*, Applied Radiation and Isotopes, 190 (2022); 110466.

5. **G. Dellepiane**, P. Casolaro, I. Mateu, P. Scampoli and S. Braccini, *Alternative routes for ^{64}Cu production using an 18 MeV medical cyclotron in view of theranostic applications*, Applied Radiation and Isotopes, 191 (2023); 110518.

6. **G. Dellepiane**, P. Casolaro, A. Gottstein, I. Mateu, P. Scampoli and S. Braccini, *Study of ^{67}Cu optimized production based on cross section measurements of ^{67}Cu and ^{64}Cu using an 18 MeV medical cyclotron*, Applied Radiation and Isotopes, 195 (2023); 110737.

During my PhD, I also contributed to the following publications:

1. S. Braccini, C. Belver-Aguilar, T. S. Carzaniga, **G. Dellepiane**, P. D. Häffner, P. Scampoli, *Novel irradiation methods for theranostic radioisotope production with solid targets at the Bern medical cyclotron*, 22nd International Conference on Cyclotrons and their Applications, Cyclotrons2019, Cape Town, South Africa (2019).

2. M. Capogni, M. Capone, A. Pietropaolo, A. Fazio, **G. Dellepiane**, R. Falconi, A. Colangeli, S. Palomba, G. Valentini, M. Fantuzi, R. Faccini, A. Pizzuto, *^{64}Cu production by 14 MeV neutron beam*, Journal of Neutron Research, 22 (2020); 257.

3. N. P. van der Meulen, R. Hasler, Z. Talip, P. V. Grundler, C. Favaretto, C. A. Umbricht, C. Müller, **G. Dellepiane**, T. S. Carzaniga, S. Braccini, *Developments toward the Implementation of ^{44}Sc production at a medical cyclotron*, Molecules, 25 (2020); 4706.

4. **G. Dellepiane**, C. Belver-Aguilar, T. S. Carzaniga, P. Casolaro, P. D. Häffner, P. Scampoli, M. Schmid and S. Braccini, *Research on theranostic radioisotope production at the Bern medical cyclotron*, Il Nuovo Cimento C, 44 (2021); 130.

5. **G. Dellepiane**, P. Casolaro, P. D. Häffner, I. Mateu, P. Scampoli, N. Voeten, E. Zyaee, S. Braccini, *Instruments and methods for theranostic radioisotope production at the Bern medical cyclotron*, 5th International Conference on Technology and Instrumentation in Particle Physics, TIPP2021, Online format (2021).

6. P. D. Häffner, C. Belver-Aguilar, P. Casolaro, **G. Dellepiane**, P. Scampoli, S. Braccini, *An active irradiation system with automatic beam positioning and focusing for a medical cyclotron*, Applied Sciences 11.6 (2021); 2452.

7. P. Casolaro, P. D. Häffner, **G. Dellepiane**, I. Mateu, P. Scampoli, N. Voeten, E. Zyaee, S. Braccini, *An Automatic Focalization System for Enhanced Radioisotope Production with Solid Targets*, 10th International Beam Instrumentation Conference, IBIC2021, Pohang, Online format (2021).

8. C. Favaretto, Z. Talip, F. Borgna, P. V. Grundler, **G. Dellepiane**, A. Sommerhalder, H. Zhang, R. Schibli, S. Braccini, C. Müller, N. P. van der

Meulen, *Cyclotron production and radiochemical purification of terbium-155 for SPECT imaging*, EJNMMI Radiopharmacy and Chemistry 6 (2021); 37.

9. **G. Dellepiane**, P. Casolaro, P. D. Häffner, I. Mateu, P. Scampoli, N. Voeten, E. Zyaee, S. Braccini, *New methods for theranostic radioisotope production with solid targets at the Bern medical cyclotron*, 1st Applied Nuclear Physics Conference, ANPC2021, Prague, Czech Republic (2021).

10. M. Capogni, M. Capone, A. Colangeli, **G. Dellepiane**, A. Fazio, M. Frisoni, M. Pillon, A. Pietropaolo, *The ^{64}Zn-based production route to ^{64}Cu $\beta^{\pm}$ emitter using accelerator-driven 14 MeV fusion neutrons*, EPL, 137 (2022); 64001.

11. J. Anders, S. Braccini, T. S. Carzaniga, P. Casolaro, M. Chatterjee, **G. Dellepiane**, L. Franconi, L. Hasler, A. Ilg, I. Mateu, F. Meloni, C. Merlassino, A. Miucci, R. Müller, M. Raimondi, M. Weber, *A facility for radiation hardness studies based on a medical cyclotron*, Journal of Instrumentation 17.04 (2022); P04021.

12. **G. Dellepiane**, *Activity measurements of a ^{64}Cu sample activated by a 14 MeV neutron beam*, Il Nuovo Cimento C, 45 (2022); 084.

13. S. Musy, P. Casolaro, **G. Dellepiane**, A. Berger, S. Braccini, R. Purtschert, *Quantification of ^{37}Ar emanation fractions from irradiated natural rock samples and field applications*, Journal of Environmental Radioactivity, 251-252 (2022); 106966.

14. S. Braccini, P. Casolaro, **G. Dellepiane**, I. Mateu, L. Mercolli, A. Pola, D. Rastelli, P. Scampoli, *Neutron fields at high- and low-energy particle accelerators: a novel experimental approach based on the DIAMON spectrometer*, Scientific Reports (2022).

15. M. T. Durán, F. Judget, Y. Nedjadi, C. Bailat, P. V. Grundler, Z. Talip, N. P. van der Meulen, P. Casolaro, **G. Dellepiane**, S. Braccini, *Half-life measurement of ^{44}Sc and ^{44m}Sc*, Applied Radiation and Isotopes, 190 (2022); 110507.

16. **G. Dellepiane**, P. Casolaro, I. Mateu, P. Scampoli and S. Braccini, *New developments for theranostic radioisotope production with solid targets at*

the Bern medical cyclotron, 28th International Nuclear Physics Conference, INPC2022, Cape Town, South Africa (2022).

17. **G. Dellepiane**, P. Casolaro, I. Mateu, P. Scampoli and S. Braccini, *Novel solid target and irradiation methods for theranostic radioisotope production at the Bern medical cyclotron*, 30th Conference of the International Nuclear Target Development Society, INTDS2022, PSI Villigen, Switzerland (2022).

18. F. Juget, M. T. Durán, Y. Nedjadi, Z. Talip, P. V. Grundler, C. Favaretto, P. Casolaro, **G. Dellepiane**, S. Braccini, C. Bailat, N. P. van der Meulen, *Activity measurement of ^{44}Sc and calibration of activity measurement instruments on production sites and clinics*, Molecules, 28 (2023); 1345.

19. S. Braccini, T. S. Carzaniga, P. Casolaro, **G. Dellepiane**, L. Franconi, I. Mateu, P. Scampoli, M. Schmid, *A two-dimensional non-destructive beam monitoring detector for ion beams*, accepted for publication by Applied Science MDPI.

20. S. Palomba, **G. Dellepiane**, R. Falconi, R. Faccini, A. Fazio, M. Capogni, M. Capone, A. Colangeli, P. De Felice, A. Vannozzi, A. Pietropaolo, *Assessment of impurity production upon 14 MeV fusion neutron irradiation of natural and isotopic ^{100}Mo samples*, submitted to European Physical Journal Plus.

21. P. Casolaro, **G. Dellepiane**, A. Gottstein, I. Mateu, P. Scampoli, S. Braccini, *Ultra-high dose rate dosimetry with miniaturized scintillation detectors coupled to optical fibers*, submitted to Scientific Reports.

Furthermore, I will be co-author in the following papers in preparation:

- **G. Dellepiane** et al., *Cross section measurement of thulium radioisotopes with an 18 MeV medical PET cyclotron for an optimized ^{165}Er production*, in preparation for submission to Applied Radiation and Isotopes.

- **G. Dellepiane** et al., *Derivation of nuclear contributions to Tb radioisotope cross sections using different enriched materials*, in preparation for submission to Applied Radiation and Isotopes.

- E. Renaldin et al., *Cyclotron production of ^{167}Tm for medical applications*, in preparation for submission to Pharmaceuticals.

The results reported in this thesis were presented at the following international conferences:

- 106th National Congress of the Italian Physics Society (SIF2020), Online format, 14-18 September 2020. Oral presentation.

- IEEE Day 2020, Online format, 6 October 2020. Oral presentation.

- 5th International Conference on Technology and Instrumentation in Particle Physics (TIPP2021), Online format, 24-28 May 2021. Poster presentation.

- 1st Applied Nuclear Physics Conference (ANPC2021), Prague, Czech Republic, 12-17 September 2021. Oral presentation.

- 107th National Congress of the Italian Physics Society (SIF2021), Online format, 13-17 September 2021. Oral presentation.

- International Conference on Radiation in Various Field of Research (RAD2022), Herceg Novi, Montenegro, 13-17 June 2022. Oral presentation.

- 6th Theranostic World Congress (TWC2022), Wiesbaden, Germany, 24-26 June 2022. Poster presentation.

- Annual Meeting of the Swiss Physical Society (SPS2022), Fribourg, Switzerland, 27-30 June 2022. Oral presentation.

- 18th Workshop on Targetry and Target Chemistry, Whistler, Canada, 21-16 August 2022. Oral presentation.

- 28th International Nuclear Physics Conference, Cape Town, South Africa, 11-16 September 2022. Oral presentation.

- 30th World Conference of the International Nuclear Target Development Society, Villigen, Switzerland, 25-30 September 2022. Oral presentation.

The oral contributions presented at the 106th and 107th National Congress of the Italian Physical Society were awarded respectively as one of the best presentations of the congress and first best presentation in the Biophysics and Medical Physics section.

PART

I

Monograph

CHAPTER 1

Radionuclides in Nuclear Medicine and Theranostics

Nuclear medicine is a branch of medicine that makes use of radioactive compounds, or radiopharmaceuticals, to diagnose and treat a wide range of diseases, in particular of oncological nature. Unlike radiotherapy with particle accelerators, in nuclear medicine the radiation is not administered from outside the body, but it is introduced into the patient by injecting the radioactive compound.

In general, a radiopharmaceutical is composed of three elements: a vector molecule that targets specific organs, tissues or cells in the human body, a radionuclide that provides the radiation component, and a linker in between that forms a stable chemical connection.
The vector molecule consists of a small organic or inorganic molecule, a peptide, a protein including antibodies, antibody fragments or a nanoparticle. It is mainly chosen according to the physiological function of the target [1].
In case of radiometal-labelled radiopharmaceuticals, whose application is becoming predominant due to the wide range of physico-chemical properties of these radionuclides, the vector molecule is linked to the radiometal by means of a bifunctional chelator (BFC) [2].
The physical characteristics of the marker radioisotope, such as the half-life and the type and energy of radiation emitted, determine whether the radiopharmaceutical is used for diagnostics (molecular imaging) or radionuclide therapy.

This chapter provides a summary of the main physical properties required for radioisotope applications in nuclear medicine. The physical principles underlying molecular imaging techniques and radionuclide therapy are briefly discussed. Finally, the theranostic approach is described and an overview of promising radionuclides for such application, which is the main focus of this thesis, is presented.

The purpose of molecular imaging is to study the in vivo metabolism and biochemistry of the investigated organs and tissues by detecting the radiotracer accumulation, without any pharmacological effect to the patient. The radionuclides used are γ or β^+ emitters for Single Photon Emission Computed Tomography (SPECT) or Positron Emission Tomography (PET), respectively, with half-life usually ranging between 1 and 24 h.
SPECT imaging is based on the detection of single photons emitted by the radionuclide by means of detectors rotating around the patient, in order to acquire multiple projections that allow for a three-dimensional reconstruction. Photon energies between 100 and 200 keV are required to obtain an optimal image [3]. The predominant radioisotope used in SPECT imaging is ^{99m}Tc, produced by molybdenum-technetium generators. Nearly 80% of the radiopharmaceuticals currently used for SPECT diagnostics in nuclear medicine are ^{99m}Tc complexes or ^{99m}Tc-labelled biomolecules [4].
PET imaging is based on the detection of 511 keV photons emitted in coincidence and back-to-back as a result of the electron-positron annihilation process, in order to obtain high-precision three-dimensional images of the injected radiopharmaceutical distribution. PET radionuclides are ideally characterized by a high branching ratio of low-energy positrons, in order to obtain a high spatial resolution image with good sensitivity, without the emission of other particles that would increase the dose absorbed by the patient. Moreover, any emitted γ-ray characterized by an energy within the coincidence window of the scanner (300-650 keV) [5], would reduce its coincidence-count-rate performance and decrease the quality of the image. Currently, the radionuclide most commonly used for PET is ^{18}F, produced with biomedical cyclotrons dedicated to radionuclide production. In particular, the glucose analogue [^{18}F]-FDG accounts for more than 90% of PET examinations worldwide [6].

Radionuclide therapy (RNT) is based on the delivery of cytotoxic levels of radiation to the site of disease, with the aim of selectively killing cancer cells while minimizing damage to normal cells. The biological effects of RNT depend on the nature of the exposed area and on the radiation used. For this reason, relative biological effectiveness (RBE) was introduced, defined as the biological damage caused by a given radiation compared to a reference one, for the same absorbed energy. The difference depends mainly on how the radiation transfers its energy to the tissue, described by the Linear Energy Transfer (LET).
Therapeutic radionuclides can be divided in three subgroups: β^-, α and Auger-electron emitters.
β^- particles are characterized by low LET (about 0.2 keV/μm) and cause biological effects mainly through single-strand breaks and the formation of chemically active free radicals. Consequently, the presence of high radionuclide concentrations within the target site is necessary to achieve therapeutic effects [7].
Their range of action of 0.5-12 mm in soft tissue ensures a sufficient dose

delivery to kill cells in a massive lesion. The so-called crossfire effect can be an advantage in treating bulky tumours, but leads to potential damage to surrounding healthy tissue.
For the treatment of small metastatic tumour lesions, α particles are particularly suitable as they travel distances of the order of 40-100 μm in the tissue, by losing up to 1000 times more energy than β^- particles [8]. The LET of about 100 keV/μm implies that the average distance between two successive ionization events is comparable to the distance between the two strands of the cell's DNA, leading to a high frequency of double breaks and thus high RBE [9].
Auger electrons have high LET (4-26 keV/μm) but short range of 2-500 nm in tissue, which limits most of their effects within single cells. To achieve high lethality it is therefore necessary for the radionuclide to be transported within the cell and preferably incorporated into the DNA [10].
Nowadays, β^--emitting radionuclides are the most common for RNT [11], mainly due to their wide availability. Besides ^{131}I, which is the current leader for thyroid cancer treatment [12], a promising radioisotope for clinical applications is the reactor-produced ^{177}Lu [13, 14].

Since the 1990s, several laboratories have studied the possibility of combining diagnostic with radionuclide therapy, setting the stage for the concept of theranostics [15, 16]. The theranostic approach is based on using the same chemical compound labelled with a diagnostic and a therapeutic radionuclide, which have identical kinetics and reactivity and undergo the same metabolic processes. Given this assumption, the analysis of the radiopharmaceutical distribution in the patient's body, obtained by molecular imaging, demonstrates the tumour uptake and enables precise estimation of the dose absorbed due to the therapeutic agent, both in the target lesion (therapeutic effect) and in the surrounding healthy tissue (side effects) [17]. This allows to predict whether the patient will benefit from a therapeutic treatment on the basis of nuclear imaging data, paving the way to the concept of personalized nuclear medicine.
For the biological behaviour to be nearly identical, the diagnostic and therapeutic radionuclide must be of the same or chemically analogous element. As an example, ^{68}Ga-labelled PET radiotracers are currently widely used in combination with their ^{177}Lu, ^{90}Y or, more recently, ^{255}Ac-labelled [18] counterparts for radionuclide therapy [19].
Besides ^{68}Ga, other longer-lived PET radiometals, such as ^{43}Sc, ^{44}Sc, ^{61}Cu, ^{64}Cu and ^{86}Y, are gaining increasing attention because they present a matched therapeutic partner (^{47}Sc, ^{67}Cu and ^{90}Y, respectively). In addition, the longer half-life offers simplified logistics compared to ^{68}Ga and allows slower metabolic processes to be followed.
In the field of therapeutic radionuclides, there is growing interest in β^- emitters whose decay is accompanied by the release of low-energy γ-rays (e.g. ^{47}Sc and ^{67}Cu), which would allow for SPECT imaging to detect the radiopharmaceutical

distribution during treatment.
The main theranostic pairs currently under study or in early adoption in clinical applications are listed in Table 1.1.

The availability of novel radionuclides in quantity and quality suitable for clinical settings is of paramount importance for the development of personalized nuclear medicine and remains a scientific challenge. In this respect, one of the best solutions is the use of dedicated biomedical cyclotrons [20] equipped with a solid target station, which I investigated during my PhD work.

This thesis was carried out in the framework of a research program ongoing at the 18 MeV Bern medical cyclotron laboratory, aimed at optimizing the production of novel radionuclides for medical applications with solid targets. As reported in detail in Chapter 3, I studied the cyclotron-production of several theranostic radioisotopes (highlighted in bold in Table 1.1), of the widely used ^{99m}Tc for SPECT imaging and of the non-standard therapeutic radionuclides ^{165}Er and ^{167}Tm.

Imaging (PET/SPECT)	Therapy
^{43}Sc, ^{44}**Sc**	^{47}**Sc**
^{61}**Cu**, ^{64}**Cu**	^{67}**Cu**
^{68}**Ga**	^{90}Y, ^{177}Lu, ^{225}Ac
^{83}Sr	^{89}Sr
^{86}Y	^{90}Y
^{110}In	^{111}In
^{124}I	^{131}I
^{152}Tb, ^{155}**Tb**	^{149}Tb, ^{161}Tb

Table 1.1: Most promising theranostic pairs under study or in early adoption. The radionuclides highlighted in bold have been investigated in the framework of this thesis.

References

[1] K. J. H. George et al. “Expanding the PET radioisotope universe utilizing solid targets on small medical cyclotrons”. In: *RSC Adv.* 11.49 (2021), pp. 31098–31123. DOI: 10.1039/D1RA04480J.

[2] E. W. Price and C. Orvig. “Matching chelators to radiometals for radiopharmaceuticals”. In: *Chem Soc Rev* 43.1 (2014), pp. 260–290. DOI: 10.1039/c3cs60304k.

[3] K. Vermeulen et al. “Design and Challenges of Radiopharmaceuticals”. In: *Seminars in nuclear medicine* 49.5 (2019), pp. 339–356. DOI: 10.1053/j.semnuclmed.2019.07.001.

[4] S. Chakraborty and S. Liu. “^{99m}Tc and ^{111}In Labeling of Small Biomolecules: Bifunctional Chelators and Related Coordination Chemistry”. In: *Current Topics in Medicinal Chemistry* 10.11 (2010), pp. 1113–1134. DOI: 10.2174/156802610791384243.

[5] H. A. Williams et al. “A comparison of PET imaging characteristics of various copper radioisotopes”. In: *European Journal of Nuclear Medicine and Molecular Imaging* 32.12 (2005). DOI: 10.1007/s00259-005-1906-9.

[6] M. E. Crestoni. “Radiopharmaceuticals for Diagnosis and Therapy”. In: *Reference Module in Chemistry, Molecular Sciences and Chemical Engineering*. Elsevier, 2018. DOI: 10.1016/B978-0-12-409547-2.14205-2.

[7] A. I. Kassis and S. J. Adelstein. “Radiobiologic principles in radionuclide therapy”. In: *Journal of Nuclear Medicine* 46 (2005), pp. 4–12.

[8] G. Kramer-Marek and J. Capala. “The role of nuclear medicine in modern therapy of cancer”. In: *Tumor Biology* 33.3 (2012), pp. 629 –640. DOI: 10.1007/s13277-012-0373-8.

[9] J. P. Pouget and J. Constanzo. “Revisiting the Radiobiology of Targeted Alpha Therapy”. In: *Frontiers in Medicine (Lausanne)* 27.8 (2021), p. 692436. DOI: 10.3389/fmed.2021.692436.

[10] B. J. B. Nelson et al. “Targeted Alpha Therapy: Progress in Radionuclide Production, Radiochemistry, and Applications”. In: *Pharmaceutics* 13.1 (2020), pp. 49 –75. DOI: 10.3390/pharmaceutics13010049.

[11] J. Lau et al. “Application of Cleavable Linkers to Improve Therapeutic Index of Radioligand Therapies”. In: *Molecules* 27.15 (2022), pp. 4959–4972. DOI: 10.3390/molecules27154959.

[12] V. R. McCready. “Radioiodine – the success story of Nuclear Medicine”. In: *Eur J Nucl Med Mol Imaging* 44 (2017), 179—182. DOI: 10.1007/s00259-016-3548-5.

[13] A. Dash et al. “Production of ^{177}Lu for Targeted Radionuclide Therapy: Available Options”. In: *Nucl Med Mol Imaging* 49.2 (2015), pp. 85–107. DOI: 10.1007/s13139-014-0315-z.

[14] R. Mikolajczak et al. “Radiometals for imaging and theranostics, current production, and future perspectives”. In: *J Labelled Comp Radiopharm* 10.62 (2019), pp. 615–634. DOI: 0.1002/jlcr.3770.

[15] A. M. Zimmer et al. “Comparative pharmacokinetics of In-111 and Y-90 B72.3 in patients following single dose intravenous administration”. In: *Antib Immunoconjug Radiopharm* 5 (1992), pp. 285–294.

[16] F. Rösch et al. “The Beginning and Development of the Theranostic Approach in Nuclear Medicine, as Exemplified by the Radionuclide Pair ^{86}Y and ^{90}Y”. In: *Pharmaceuticals (Basel)* 10 (2 2017), pp. 56 –84. DOI: 10.3390/ph10020056.

[17] K. Mishiro et al. “Radiotheranostics with radiolanthanides: Design, development strategies, and medical applications”. In: *Coordination Chemistry Reviews* 383 (2019), pp. 104–131. DOI: doi.org/10.1016/j.ccr.2018.12.005.

[18] C. Kratochwil et al. “^{225}Ac-PSMA-617 for PSMA-Targeted α-Radiation Therapy of Metastatic Castration-Resistant Prostate Cancer”. In: *Journal of Nuclear Medicine* 57.12 (2016), pp. 1941–1944. DOI: 10.2967/jnumed.116.178673.

[19] A. Türler. “Matched Pair Theranostics: Medicinal Chemistry and Chemical Biology Highlights”. In: *CHIMIA* 73.11 (2019), p. 947. DOI: 10.2533/chimia.2019.947.

[20] S. Braccini. “Compact medical cyclotrons and their use for radioisotope production and multi-disciplinary research”. In: *21st International Conference on Cyclotrons and their Applications (CYC2016), Zurich, Switzerland*. 2017, pp. 229–234. DOI: 10.18429/JACoW-Cyclotrons2016-TUD01.

CHAPTER 2

Instruments and Methods for Novel Radionuclides at the Bern Medical Cyclotron

2.1 The Bern medical cyclotron laboratory

The Bern cyclotron laboratory is the result of the SWAN (SWiss hAdroN) project, a collaboration between the Bern University Hospital (Inselspital), the University of Bern and private institutions. This project, started in 2007, aimed at realizing a combined medical and research centre able to provide the most cutting-edge technologies in medical imaging and cancer radiation therapy [1].
The cyclotron laboratory was built in 2011 in the Inselspital campus to host industrial radionuclide production for PET diagnostics and multidisciplinary research activities. The AEC-LHEP group on medical applications of particle physics of the University of Bern is engaged in research in various fields, in collaboration with several national and international institutions such as the DCBP radiochemistry group of the University of Bern, the Paul Scherrer Institute (PSI) and CERN. Commercial production of radiopharmaceuticals is handled by the spin-off company SWAN Isotopen AG.

To allow both academic research and industrial production running in parallel, the cyclotron was equipped with a 6.5-m-long external beam line that transports the beam to a secondary bunker with independent access. In 2015 a solid target station was also installed on the cyclotron to enhance research into novel radioisotope production.

The facility features an underground area, where the cyclotron, the beam line and the physics laboratory are located, and an upper floor with three

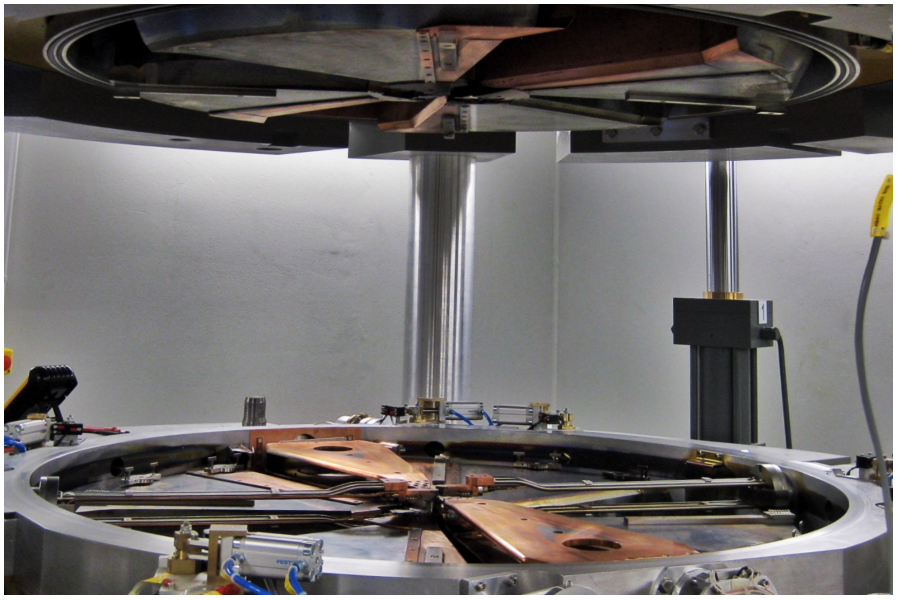

Figure 2.1: The Bern medical cyclotron open during maintenance.

GMP (Good Manufacturing Practice) laboratories for radiotracer production and one laboratory fully dedicated to research activities in radiochemistry and radiopharmacy [2].

The IBA Cyclone 18/18 HC cyclotron

The Bern medical cyclotron laboratory features an IBA Cyclone 18/18 HC cyclotron, shown in Figure 2.1, whose main technical characteristics are reported in Table 2.1.

To enhance the commercial production reliability, the machine is equipped with two H^- ion sources so that the production can restart immediately in the event of failure of one of the two. The sources are internal cold-cathode Penning Ionization Gauge (PIG), characterized by two cathodes placed at each end of a cylindrical anode (*chimney*) and by a strong magnetic field along the cylindrical axis. A plasma discharge is generated between the electrodes, predominantly confined by the strong magnetic field [3]. The ions are extracted through a slit on the anode side because of the electric field that exists between the chimney and an additional electrode (*puller*) outside the slit [4].

To optimize the vertical focusing and longitudinal phase stability of the accelerated ions, the cyclotron is divided into four 60° sectors at high magnetic field (*hills*) that alternate with four 30° sectors at low magnetic field (*valleys*). This configuration implies that the orbits are not circular and has led to the need

Constructor	Ion Beam Applications (IBA), Belgium
Type	Cyclone 18/18 HC
Accelerated particles	H^- (D^- on option)
Energy [MeV]	18 (9 for D^-)
Maximum current [μA]	150 (40 for D^-)
Ion sources	2 internal PIG H^-
Extraction ports	8
Extraction	Carbon foil stripping
Strippers	2 per extraction port
Isotope production targets	6 ^{18}F - Liquid Targets, NIRTA Solid Target Station
Beam Transport Line (BTL)	6.5 m long; 2 quadrupole magnets; XY steering magnet

Table 2.1: Main characteristics of the Bern medical cyclotron [2].

for precise adjustment of the cyclotron dipole magnetic field by means of an iterative procedure [5].
Considering the average magnetic field B of 1.4 T, the cyclotron frequency ν_c can be estimated as:

$$\nu_c = \frac{qB}{2\pi m} \approx 21 \text{ MHz} \tag{2.1}$$

where q and m are the charge and the mass of the proton, respectively.
Acceleration takes place in four gaps located at the boundaries of two radio-frequency (RF) cavities (*dees*), applying a potential

$$V(t) = V_{RF} \sin(2\pi\nu_{RF} t) \tag{2.2}$$

where V_{RF} is the RF peak voltage, ν_{RF} is its frequency and t is time.
For acceleration to occur, the RF frequency must be proportional to the cyclotron frequency

$$\nu_{RF} = h\nu_c \tag{2.3}$$

where h is a natural number, called RF harmonic. Since the cyclotron is equipped with two dees, only even harmonics of the cyclotron frequency lead to acceleration. When accelerating H^- ions, the RF system of the Bern cyclotron operates in second harmonic, with ν_{RF} = 42 MHz.
The energy gained by the ions per turn, ΔE_k, is given by

$$\Delta E_k = 2qNV_{RF} \sin(h\frac{\alpha}{2}) \tag{2.4}$$

where $N = 2$ is the number of dees and $\alpha = 30°$ is the azimuthal dee angular length. Considering an average RF peak voltage of 30 kV, the energy gain per revolution is about 60 keV, so the H^- ions must travel about 300 turns to reach the nominal energy of 18 MeV and be extracted.

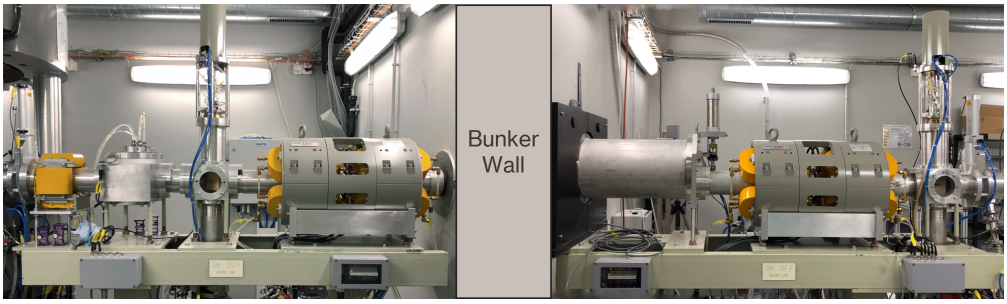

Figure 2.2: Schematic view of the 6.5-m-long Beam Transport Line.

The extraction is achieved by the stripping method, with an efficiency of nearly 100%. For this purpose, 5-μm-thick pyrolytic carbon extraction foils [6], mounted in pairs of two on a rotating carousel, are used. This solution allows rapid substitution of a damaged stripper by simply rotating the carousel, without opening the cyclotron. The angle of the stripper with respect to the beam can be adjusted to optimize extraction, which takes place in one of the eight cyclotron out-ports with currents of up to 150 μA.

The Beam Transport Line

The Beam Transport Line (BTL) of the Bern medical cyclotron is the main instrument for pursuing research activities in various fields, such as particle detectors, radiation biology, radiation hardness studies [7], neutron dosimetry [8], and, in particular, cross section measurements and the study of new radioisotopes for medical applications. For this purpose, it is necessary to be able to obtain beams of different sizes (from a few millimiters to about a few centimeters in diameter on target) and intensities (from nA to the maximum current of 150 μA), and to have an extensive knowledge of the beam characteristics.

A schematic view of the BTL is shown in Figure 2.2. It consists of two horizontal-vertical (H-V) quadrupole doublets, an XY steering magnet, two beam viewers to measure the current, and a movable cylindrical neutron shutter to prevent neutron penetration into the beam-line vault during the production of radioisotopes. The two quadrupoles, the first located in the cyclotron bunker and the latter in the second bunker, can focus the beam down to one millimeter and defocus it up to several centimeters. The steering magnet can bend the 18 MeV beam of maximum ±7 mrad horizontally and/or vertically. Vertical and horizontal alignment of the BTL elements was performed using lasers, and a 95% transmission of the beam was achieved.

To optimize the extraction of the beam to the BTL, a special asymmetrical carousel (Figure 2.3) was designed and mounted. The different length of the

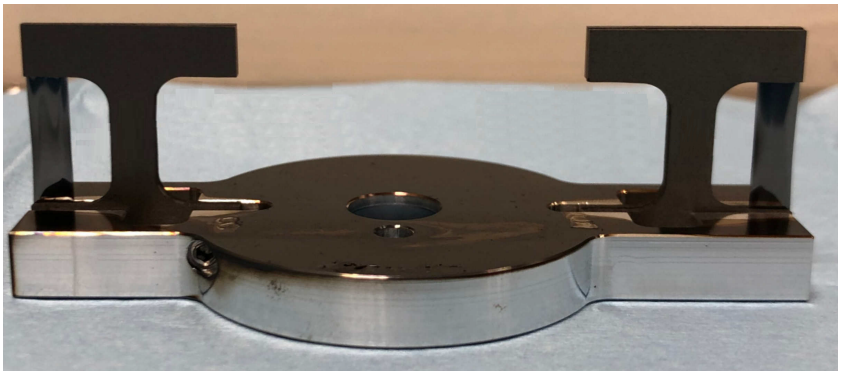

Figure 2.3: Modified carousel for an optimized beam extraction to the BTL.

arms allow the beam to be extracted at different orbits, affecting the output energy [9].

Beam stability down to the pA range was achieved with a procedure developed by our group, based on tuning the ion source, the radio-frequency and the current in the main coil [10]. A minimum current of approximately 1 pA was achieved with this method, about seven orders of magnitude lower than the current for which medical cyclotrons are normally optimized.

The Solid Target Station

To produce radionuclides from solid material targets, an IBA NIRTA Solid Target Station (STS) was installed on the out-port 7 of the cyclotron (Figure 2.4). The STS has an 8-mm-diameter collimator to provide a beam of controlled diameter, which is water-cooled in order to dissipate the full beam power (500 W) in case the beam is completely off-centered or defocalized.

The collimator and the body of the STS are connected to two electrometers (B29885A Keysight) to measure the current online during the irradiation. The effective current hitting the target material was assessed by measuring the 2D beam profiles with radiochromic films [11], as described later in this chapter.

The STS was designed to irradiate a platinum or gold disc, 24 mm in diameter and 2 mm thick, on which the target material is electroplated. To limit overheating during the irradiation, the disc is water-cooled and helium-cooled on the back and the front side, respectively. The helium cooling loop is separated from the cyclotron vacuum by a 25-mm-diameter disc called *vacuum window*. The vacuum window degrades the energy of the beam passing through it, so the appropriate thickness and material must be selected to optimize radionuclide production. Considering the nominal energy of the Bern medical cyclotron, the

Figure 2.4: The STS installed on the out-port 7 of the Bern medical cyclotron.

highest achievable energy in the STS outport is 17.8 MeV, if a 10 μm vacuum window in Havar is mounted.

Since the production of many interesting radionuclides is performed by irradiating materials that cannot be electrodeposited but are available in form of powder or solid foil, a specific magnetic target capsule was conceived and constructed by our group.

The target coin The capsule, called *coin*, has the same external dimensions as an ordinary disc but it is made of two aluminum or niobium halves kept together by small permanent magnets (Figure 2.5), allowing for quick and easy opening and closing also inside a hot cell. To optimize the radionuclide production, the material and the thickness of the front-end are used to adjust the energy of protons reaching the target. A 6-mm-diameter foil or compressed powder pellet is placed in a pocket of the back-end, the depth of which can be modified to ensure good thermal contact between the irradiated material and the front-end of the coin. An O-ring is embedded in the back-end to prevent the leakage of any molten material or gas produced during the irradiation. The back-side of the coin is also necessary to completely stop the protons, in order not to activate the water-cooling system.

During my PhD, I contributed to the design and realization of several coins, the characteristics of which were optimized for the specific application.

Because the cyclotron is used overnight for radionuclide production, the radia-

Figure 2.5: The two halves of the coin target (24 mm diameter, 2 mm thick).

tion level inside the bunker is always very high and the entry of operators can lead to radio-protection concerns. For this reason, the STS was customized to insert and eject the target without opening the cyclotron bunker [12].

The Hyperloop The loading of the station is performed by means of a mechanical transfer system, called Hyperloop, developed and implemented by the LHEP workshop with my contribution. The coin is inserted into a loading station shuttle outside the bunker (Figure 2.6-a), paying attention to the direction of the front-end to be irradiated, and driven over the STS by means of a cable. It then falls into the STS through a conduit, narrow enough not to allow its rotation (Figure 2.6-b), and gets locked in the irradiation position.

The Solid Target Transfer System After the irradiation, the target is transferred from the bunker area by means of a pneumatic Solid Target Transfer System (STTS) by TEMA Sinergie (Figure 2.7-a). The system consists of a rotating plate that can hold up to 6 shuttles, an automatic manipulator to de-cap the shuttle, and a tube connected to the STS. The irradiated coin falls inside the shuttle placed under the irradiation unit and can be sent either to one hot cell in the nearby GMP radio-pharmacy, where the chemical processes are performed, or to a receiving station located in the BTL bunker (Figure 2.7-b) for further analysis or for transport to external research laboratories. The receiving station consists mainly of a tube through which the shuttle drops into a lead pot. It is equipped with a remote camera to follow the delivery procedure from the cyclotron control room, an automatic lead pot closure system, and a CZT (Cadmium Zinc Telluride) detector to perform spectrometric analysis of the irradiated target. The detector, described later in this chapter, is mounted on a programmable step motor that allows it to be positioned up to 40 cm from the target [13].
This novel system was developed by our group with my contribution and allows measuring the activity produced right after the End of Beam (EoB).

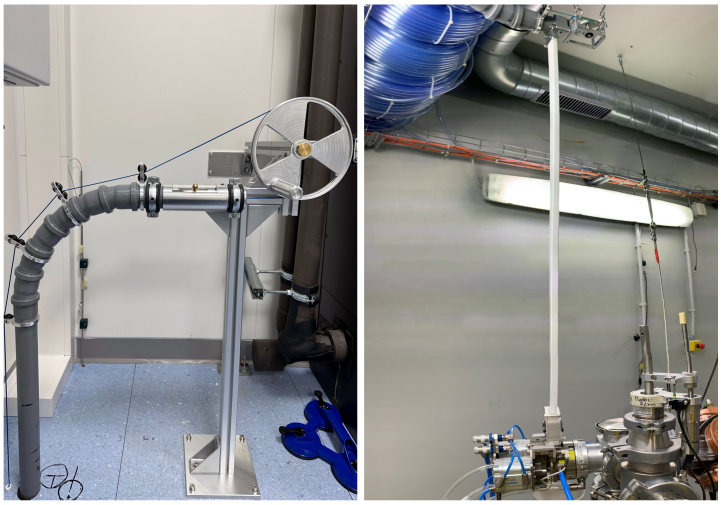

(a) (b)

Figure 2.6: The loading station (a) and the final part (b) of the Hyperloop to load the STS.

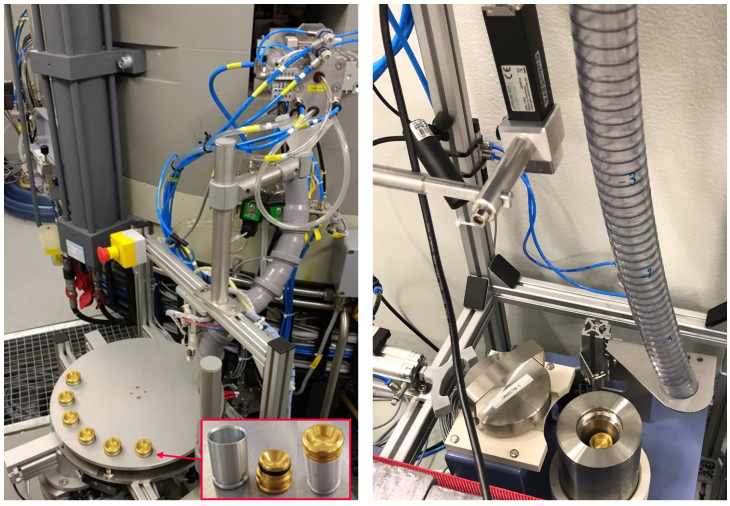

(a) (b)

Figure 2.7: (a) The STTS by Tema Sinergie with a shuttle in the inset. (b) The receiving station in the BTL bunker.

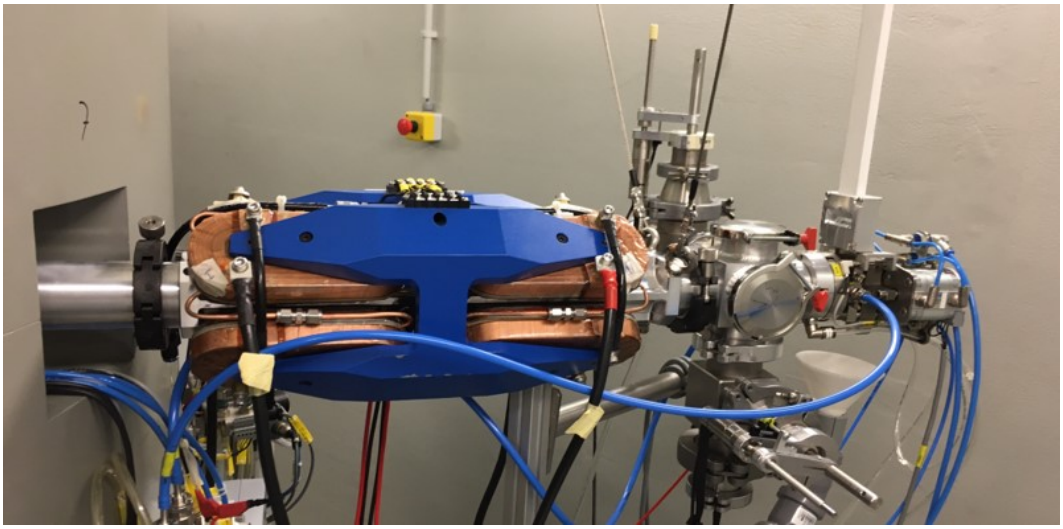

Figure 2.8: The Automatic Focusing System installed in the cyclotron bunker.

The Automatic Focusing System

If the STS is mounted on the out-port of the cyclotron without any optical device for beam steering and focusing, the extracted beam is characterized by a ~12 mm FWHM (Full Width Half Maximum) or more on target. This implies that about 75% of the extracted protons do not hit the 6-mm-diameter pellet, causing overheating during the irradiation and unwanted residual activity, which gives rise to radiation protection issues.

To limit unnecessary stress for the machine and enhance the irradiation performance, an Automatic Focusing System (AFS) was conceived, developed and recently tested [14].

The AFS consists of the Mini-PET Beamline (MBL) by D-Pace [15], a two-dimensional beam profiler (named UniBEaM and introduced in the next section) and a software feedback system. The MBL is a 50-cm-long magnet, embedding two quadrupole and two steering magnets within the same structure. The feedback system analyses the beam profiles measured by the UniBEaM and, if necessary, corrects the beam position and shape by varying the current in the power supplies of the MBL [16]. This is particularly important in the case of focused beams, since during the irradiation the magnetic dipole of the cyclotron heats up and causes small drifts in the beam position and size, which would considerably decrease the current on target.

Functional tests were successfully carried out by installing the AFS at the end of the BTL [17]. In particular, the focusing capabilities of the system were

demonstrated and a gain factor of about 20 was found in the radioisotope production using solid targets [18, 19].

The AFS was recently installed in front of the STS in the cyclotron bunker (Figure 2.8) and the first tests are currently ongoing. In this regard, I contributed significantly to the optimization of the irradiation procedure. The configuration that optimizes the beam transmission was determined by varying the stripper angle and the MBL magnet parameters and by measuring the current hitting the coin and the collimator.

To verify that the beam was centered and to assess the current actually hitting the 6-mm pellet, a gafchromic film was inserted in a coin and irradiated. As shown in Figure 2.9-a, the front part of the coin had a 9-mm-diameter hole to prevent the beam from being degraded or scattered. The gafchromic film was then scanned (Figure 2.9-b) to determine the 2D beam profile. The intensity of the beam in the two axes as a function of position is shown in Figure 2.10.
It can be observed that, although not perfectly circular, the beam is centered on target and has a constant intensity within 8%. In this configuration, the current hitting the 6-mm pellet can be determined by considering the ratio between the areas and it is characterized by an average uncertainty of about 10%.

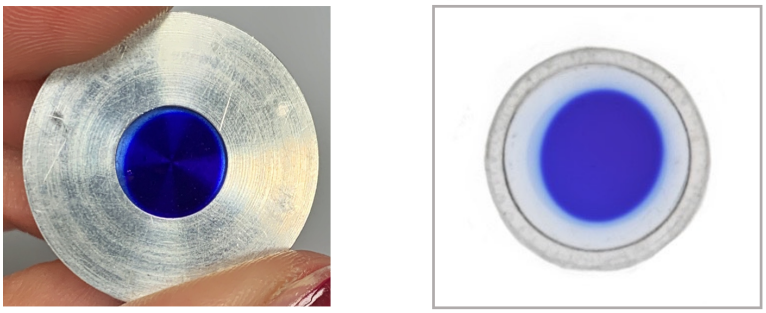

Figure 2.9: (a) Gafchromic film inserted into a coin with a 9-mm diameter hole in the front part. (b) Scanning of the gafchromic film.

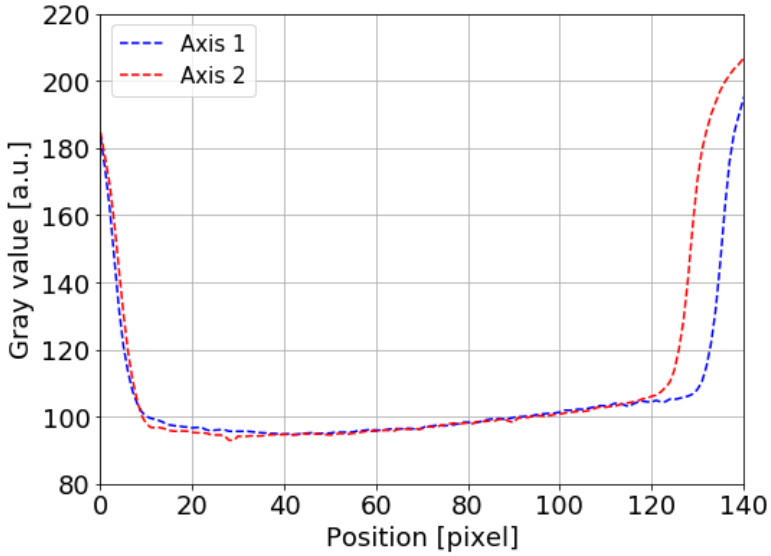

Figure 2.10: Beam intensity in the horizontal and vertical plane as a function of the position.

The UniBEaM detector

To accurately know the position, intensity and shape of the beam in real time during experiments, our group designed and built a non-destructive beam monitoring detector named UniBEaM (Universal Beam Monitor) [20]. It is based on a Ce or Sb doped silica scintillating fiber moving transversely through the beam by means of a high-precision motor. The scintillation light produced by the passage of charged particles is transmitted to a photon detector, whose electronic signal is then digitized. The scintillating fiber is coupled to a commercial optical fiber several meters long to transport the signal with negligible attenuation. This solution allows the electronics and other radiation-sensitive devices to be placed outside the bunker, avoiding possible damage due to neutron irradiation. The motor step size and the acquisition time between steps can be adjusted according to the experiment. Typical values are 250 μm and 10 ms, respectively. At each step, the digitized signal is reported on real time as a function of the position of the fiber to visualize the beam profile. The working principle and the main components of the UniBEam are reported in Figure 2.11.

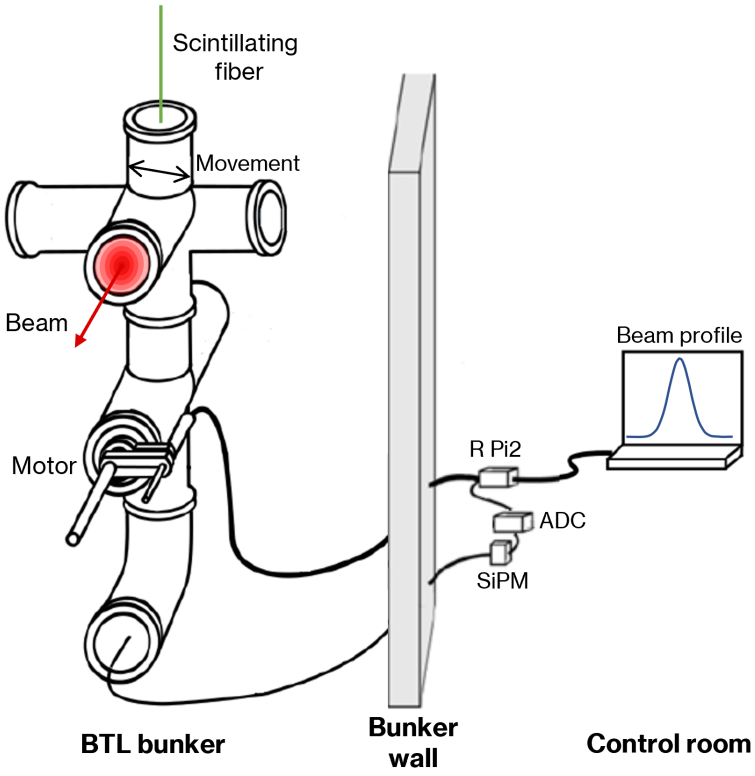

Figure 2.11: Schematic view of the working principle and main components of the UniBEaM detector.

Figure 2.12: Commercial version of the UniBEaM detector, produced by D-Pace.

The UniBEaM has been successfully tested with a continuous 18 MeV proton beam in the current range from 1 pA to 20 μA [21].
A commercial version of the UniBEaM, based on two fibers to investigate the horizontal and vertical planes simultaneously, was licensed to D-Pace [22]. This two-dimensional version of the UniBEaM was used for the cross section measurements reported in this thesis and it is shown in Figure 2.12.

Detectors for γ spectrometry

The HPGe detector The Bern medical cyclotron laboratory is equipped with a High-Purity Germanium (HPGe) detector to perform spectrometric analysis of irradiated targets and precisely determine the produced activity. The HPGe, shown in Figure 2.13-a and Figure 2.13-b, is a N-type from Mirion Technologies (Canberra) with coaxial geometry and with the sensitive volume shielded by 10 cm of lead. The detector is characterized by a non-paralyzable dead time and it is coupled to a preamplifier and to a Lynx® digital signal analyzer. The spectrum of the source is acquired with the Genie2K [23] software in the case of a single measurement and with the Excel2Genie [24] Microsoft Excel application for repeated measurements. The analysis is carried out with the InterSpec software [25], developed by the Sandia National Laboratories.

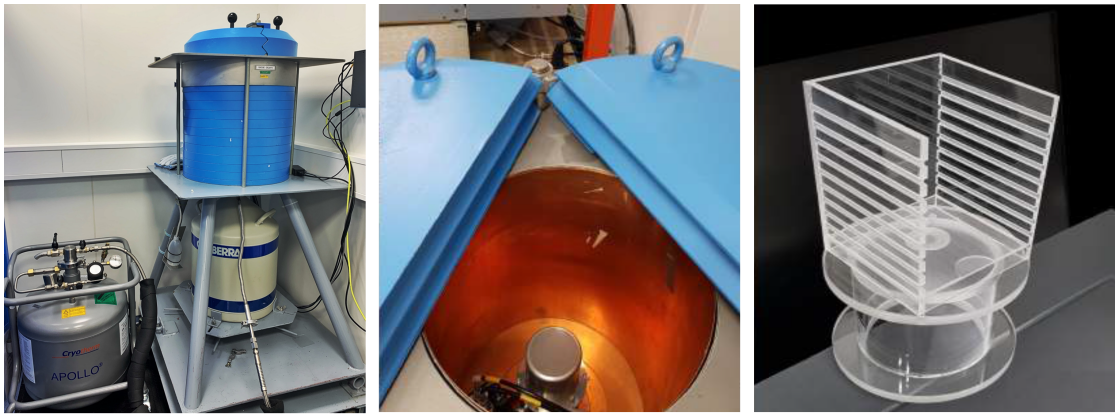

Figure 2.13: The HPGe detector closed (a) and open (b); the plexiglass ladder for dead-time optimization (c).

The efficiency calibration was performed with a multi-γ source (Czech Metrology Institute, source number 201020-1800042, 2020), presenting several elements (^{241}Am, ^{109}Cd, ^{139}Ce, ^{57}Co, ^{60}Co, ^{137}Cs, ^{113}Sn, ^{85}Sr and ^{88}Y). The calibration source was measured at distances up to 10 cm from the detector, thanks to a custom-designed plexiglass ladder with equally spaced levels 1 cm apart (Figure 2.13-c).
This solution ensures that the targets are precisely centered with respect to the crystal and allows to optimize the dead-time of the detector by changing their distance. A second 1-m-high scale was constructed to measure very high activities without saturating the detector. In this case, the efficiency calibration was performed every 10 cm.

The detector efficiency, ϵ_{HPGe}, is a function of the distance of the source, d, and of the energy of the γ considered, E_γ, and can be calculated with the following formula:

$$\epsilon_{HPGe}(d, E_\gamma) = \frac{A_{HPGe}(t)}{A(t_0)} \frac{\lambda RT}{1 - e^{-\lambda RT}} \cdot e^{\lambda(t-t_0)} \tag{2.5}$$

where $A_{HPGe}(t) = C(t)/LT$ is the background-corrected count rate (in counts/s) of the analyzed γ-peak, with $C(t)$ the peak area at the time t and LT live time of the measurement , $A(t_0)$ is the photon activity of the γ-line at the reference date, $\frac{\lambda RT}{1 - e^{-\lambda RT}}$ and $e^{\lambda(t-t_0)}$ are correction factors for the measurement duration and the cooling time, respectively, with λ the decay constant of the given radionuclide and RT the real time of the measurement.

At each level of the ladder, the measured efficiencies as a function of the γ

energies are fitted with the following function [26]

$$\epsilon_{HPGe}(E_\gamma) = \frac{1}{E_\gamma} \cdot \sum_{i=1}^{6} p_i \log^{i-1} E_\gamma \tag{2.6}$$

using a parametric least-squares fit. The photon energies E_γ are the error-free parameters and p_i the fitting parameters.

The experimental uncertainties in the efficiency calibration procedure include the error on the radionuclide activities at the reference time (up to 1.5%) and the statistical error in the net peak areas (about 1%). All the contributions were summed in quadrature to obtain the overall uncertainty of the measured efficiencies. The efficiency uncertainties at γ energies different from the calibration source ones are retrieved from the parametric least-squares fit.

The CZT detector A second detector for γ spectrometry is embedded in the receiving station in the BTL bunker, in order to have a benchmark of the produced activity before shipping the irradiated target to other laboratories for radiochemical processing. In this case, the detector must be able to measure the high activity produced without saturating, it must be small enough to be integrated into the receiving station, and it must be able to work at room temperature. On the basis of these considerations, a Cadmium-Zinc-Telluride (CZT) semiconductor detector from GBS Elektronik GmbH (Cube527E) was chosen. The main characteristics of the CZT detector are reported in Table 2.2.

The spectrum of the source is acquired with the WinSPEC software and analyzed with a specially developed Python script. This program reads the raw data provided by the detector, identifies and analyzes the photo-peaks in the spectrum and provides the activity of the corresponding radionuclides.

The linearity of the energy response and the energy resolution of the CZT were verified by placing the multi-γ calibration source in contact with the detector surface. In particular, a resolution of about 2% was found for the peak at 661 keV, in good agreement with the value provided by the manufacturer (Table 2.2).
Since the multi-γ source was too weak to perform the efficiency calibration at different distances from the detector, I used a two-step procedure. Different materials were irradiated with the STS to produce several radionuclides (^{48}V, ^{61}Cu, ^{63}Zn, ^{66}Ga, ^{166}Tm) in high quantities and then measured with the CZT at the four positions provided by the programmable step motor (10, 20, 30 and 40 cm from the source). After an appropriate cooling time, the samples were measured with the HPGe detector and the resulting activities were actualized to the time frame of the CZT measurements.

Crystal size [mm^3]	500
FWHM @ 662 keV [%]	< 2.5
Channels	1024
PoE [W]	< 2
Dimensions [cm]	$11 \times 2.5 \times 2.5$
Weight [g]	150

Table 2.2: Main characteristics of the Cube527E detector from GBS Elektronic GmbH.

The efficiencies were then determined using Eq. 2.5 and Eq. 2.6.

The uncertainty of the measured activity varies between 6 and 10% for the different positions and the range of detectable activity is of the order of a few hundreds of MBq, depending on the particular radionuclide.

2.2 Methods for an optimized radionuclide production

Accurate knowledge of the energy of the pristine beam and of the cross section of the involved nuclear reactions is crucial for the production of novel medical radioisotopes, making it possible to optimize the radionuclide yield and prevent the production of unwanted radioisotopic impurities.

Beam energy measurement

At the out-port of the BTL, the extracted energy was accurately measured with different methods based on the assessment of the beam current after passive absorbers of different thicknesses [27], on a multi-leaf Faraday cup [28] and on Rutherford Backscattering Spectrometry [29]. A further apparatus based on the deflection of the beam by a dipole electromagnet allowed to study the beam energy as a function of several operational parameters of the cyclotron and provided a mean energy of (18.59 $\pm$ 0.14) MeV for a stripper angle of 97.1° [30].

Inside the cyclotron bunker, lack of space prevents the installation of experimental apparatus dedicated to the direct measurement of the beam energy and indirect measurement techniques must be used.

In order to measure the energy of the beam extracted to the STS out-port, I contributed to the development of a method based on the stacked-foil technique. The well known monitor reaction ^{nat}Ti(p,x)^{48}V was chosen for this purpose, being characterized by a particular shape so that the produced activity strongly depends on the beam energy [31]. Two 125 μm Nb energy degraders and six 25 μm natural Ti foils with a diameter of 13 mm were inserted in the coin pocket and irradiated. A specially designed coin with a 12-mm-diameter hole in the front-end was used to prevent the beam from degrading its energy or scattering. Each foil was then measured with the HPGe detector, to precisely assess the produced activity. The measured activities were then plotted as a function of the Ti foil's number for several initial energies and an iterative least-squares minimization method was applied to identify the initial energy that minimizes the sum of squared residuals.

This method was validated in the BTL and allowed to measure the energy of the beam extracted to the STS out-port, obtaining (17.78 $\pm$ 0.05) MeV for a stripper angle of 89.1°.

The beam energy measurement for different stripper angles is currently in progress and it will be published in a forthcoming paper, in which I will be one of the co-authors.

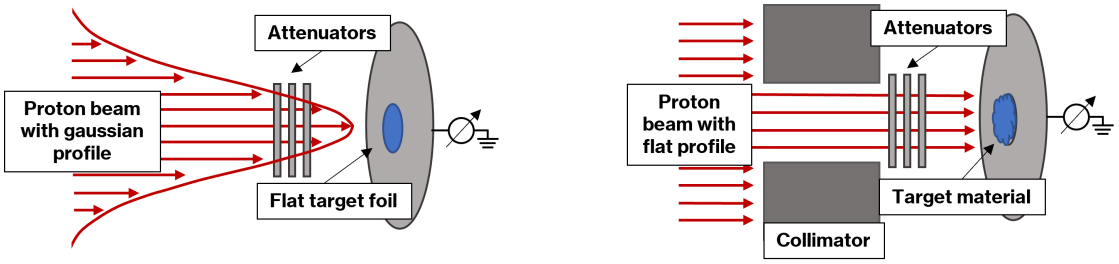

Figure 2.14: Schematic view of the cross section measurement technique in the case of the standard method (a) and the flat-beam method (b).

Production cross section measurement

The standard method to measure the cross sections is based on the irradiation of a homogeneously thick target with a beam of known energy, as schematically shown in Figure 2.14-a.
In this case, the beam shape plays no role and the cross section as a function of the input energy is defined as

$$\sigma(E) = A(t_{EoB}) \cdot \frac{q}{I} \cdot \frac{1}{dm/dS} \cdot \frac{m_{mol}}{N_A \beta \eta} \cdot \frac{1}{1 - e^{-\lambda t_i}} \tag{2.7}$$

where $A(t_{EoB})$ is the activity produced at the EoB, q is the elementary charge, I is the current on target, dm/dS is the target mass per unit surface, N_A is the Avogadro constant, β is the isotopic ratio of the target nucleus in the material, η its stoichiometric number and $\frac{1}{1 - e^{-\lambda t_i}}$ is a correction term which considers the decay of the radionuclide (with decay constant λ) during the irradiation time t_i.
The EoB activity is measured by γ spectrometry and is given by

$$A(t_{EoB}) = \frac{A_{det}(t)}{\epsilon \cdot BR} \cdot \frac{\lambda RT}{1 - e^{-\lambda RT}} \cdot e^{\lambda (t - t_{EoB})} \tag{2.8}$$

where $A_{det}(t)$ is the background-corrected count rate (in counts/s) of the analyzed γ-peak, ϵ is the efficiency of the detector for the analyzed γ-line, BR is its branching ratio, $\frac{\lambda RT}{1 - e^{-\lambda RT}}$ and $e^{\lambda (t - t_{EoB})}$ are correction factors for the measurement duration and the cooling time, respectively, with λ the decay constant of the given radionuclide and RT the real time of the measurement.

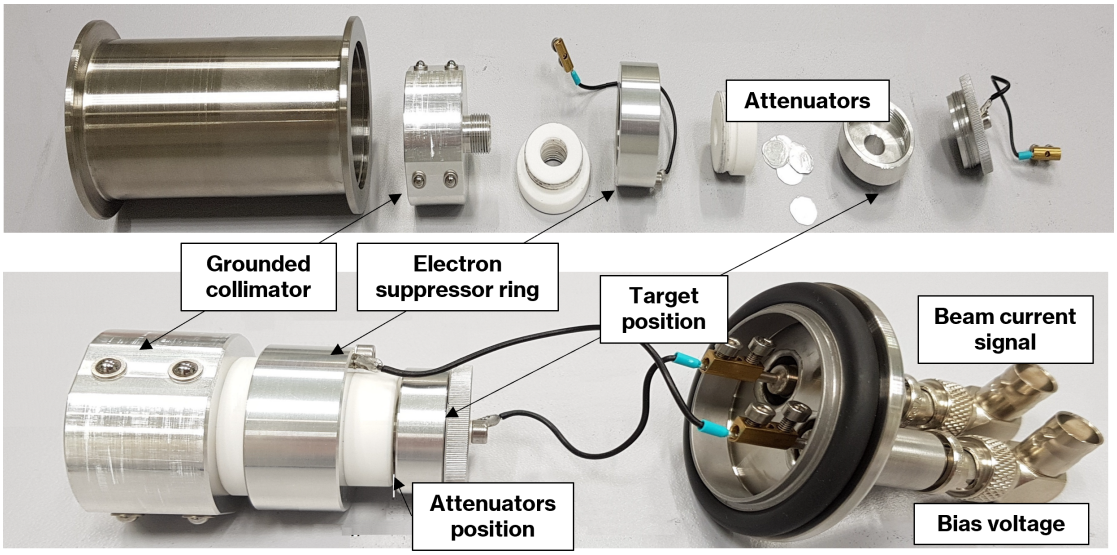

Figure 2.15: Target station for cross section measurements.

The standard method is suitable for target materials available in solid foil form, for which the target mass surface density is constant; in the case of powders, however, obtaining homogeneous thicknesses is very challenging and often impossible. For this reason, a new procedure based on the irradiation of the full target mass with a flat proton beam (Figure 2.14-b) was developed by our group [32].
In this case, the cross section depends on the total target mass m and on the current density dI/dS, and is given by the formula

$$\sigma(E) = A(t_{EoB}) \cdot \frac{q}{dI/dS} \cdot \frac{1}{m} \cdot \frac{m_{mol}}{N_A \beta \eta} \cdot \frac{1}{1 - e^{-\lambda t_i}} \tag{2.9}$$

The beam is flattened by the optical elements of the BTL and its position and shape are measured on-line with the UniBEaM detector. The beam current hitting the target is measured by means of a custom target station mainly composed of a 6 mm diameter collimator, an electron suppressor ring and a target holder (Figure 2.15). The collimator is grounded and provides a beam of controlled diameter, within which the beam flatness is obtained with an uncertainty of less than 5%. The electron suppressor ring is connected to a negative bias voltage in order to repel secondary electrons produced during the irradiation, that would increase the measured beam current. Current measurements on target are performed throughout each irradiation by connecting the target holder to an electrometer (B29885A Keysight). The conductive parts of the target station are kept together by insulator components. The beam energy is degraded by means of aluminum attenuator discs placed in front of the target and it is determined using the SRIM Monte Carlo code [33].

(a) (b) (c) (d)

Figure 2.16: Targets for cross section measurements: (a) empty aluminum disc; (b) deposition procedure; (c) disc pocket filled; (d) aluminum disc covered with a 13-μm-thick aluminum foil.

The produced activity is assessed by γ spectrometry with the HPGe detector.

The target consists of a 23 mm disc, usually made of aluminum, with a 4 mm diameter and 0.8 mm deep pocket in its center (Figure 2.16-a). The target material is deposited by sedimentation from a suspension of a few milligrams of powder in ultra-pure water or ethanol, which is then evaporated by means of a heating plate (Figure 2.16-b and Figure 2.16-c). The target mass is assessed with an analytical balance (Mettler Toledo AX26 DeltaRange). To prevent the material escape during the irradiation and the measurement procedure, the disc is covered by a 13-μm-thick aluminum foil (Figure 2.16-d). With this method, target thicknesses of a few tens of μm can be achieved and the beam energy can be considered constant within the uncertainties over the full irradiated mass.

Nuclear cross section calculation

When dealing with cross sections, it is necessary to distinguish between the nuclear (or reaction) cross section, which is independent from the isotopic composition of the irradiated material, and the production (or total) cross section, which depends on the percentage of the starting isotope in the irradiated material.

If the radionuclide of interest is produced by a single reaction (p,x), the total cross section is equal to the nuclear cross section (Eq. 2.9) multiplied by the isotopic percentage β of the target isotope in the irradiated material:

$$\sigma_{TOT} = \beta \cdot \sigma(p, x) \tag{2.10}$$

If, on the other hand, the radionuclide is produced by several reactions starting from isotopes with different abundances, the total cross section is given by a linear combination of the nuclear cross sections and can be measured with Eq. 2.9 by setting $\beta = 1$.
In the case of two reactions (p,x) and (p,y) starting from the i-th and j-th isotope,

respectively, the production cross section is given by

$$\sigma_{TOT} = \beta_i \cdot \sigma(p,x) + \beta_j \cdot \sigma(p,y) \tag{2.11}$$

and it can only be compared with other experimental data if they were obtained from a material with the same isotopic abundance, as in the case of natural abundance.

To disentangle the two nuclear contributions to the production cross section, I developed a method based on the inversion of a linear system of equations. This method requires measuring the total cross section from as many materials with different isotopic composition as there are reactions involved in the production of the radionuclide of interest.
In the case of two reactions (p,x) and (p,y), considering two materials A and B with different known isotopic compositions, the following linear system holds for a given beam energy E:

$$\begin{cases} \sigma^A_{TOT} = \beta^A_i \cdot \sigma(p,x) + \beta^A_j \cdot \sigma(p,y) \\ \sigma^B_{TOT} = \beta^B_i \cdot \sigma(p,x) + \beta^B_j \cdot \sigma(p,y) \end{cases} \tag{2.12}$$

where the experimentally-measured production cross sections appear on the left side of the equations and the reaction cross sections to be determined on the right.

Study of production yield and radionuclidic purity

On the basis of the cross section measurements, it is possible to define the irradiation parameters that optimize the production by performing a study of the radionuclide yield and purity.

For an infinitely thick target, where the beam is completely stopped or degrades its energy to below the threshold for producing the measured product, it is possible to define the Thick Target Yield (TTY) as the producible activity per unit current and time.
The TTY for a given proton entry energy E is given in GBq/μAh and can be calculated using the following formula:

$$TTY(E) = \frac{A(t_{EoB})}{I \cdot t_i} = \frac{(1 - e^{-\lambda t_i})}{t_i} \cdot \frac{N_A \cdot \eta}{m_{mol} \cdot q} \int_{E_{th}}^{E} \frac{\sigma(E')}{S_p(E')} dE' \tag{2.13}$$

where $A(t_{EoB})$ is the activity produced at the EoB, I the current on target, t_i the irradiation time, $(1 - e^{-\lambda t_i})$ is the saturation factor defining the competition between production and radioactive decay (defined by the decay constant λ) during the irradiation, N_A the Avogadro constant, m_{mol} the average molar mass of the target material, η the number of target atoms of the desired species per

molecule, q the charge of the projectile, $\sigma(E')$ the cross section as a function of the proton kinetic energy E', $S_p(E')$ is the mass stopping power for the target material and E_{th} is the threshold energy of the considered reaction. The mass stopping power is calculated using SRIM [33].

For an irradiation much longer than the half-life of the produced radionuclide ($\lambda t_i >> 1$), an equilibrium is reached whereby longer irradiation does not correspond to an increase in production. In this case, the thick target saturation yield TTY_{sat} is defined as the activity produced per unit current and is measured in $GBq/\mu A$. The TTY_{sat} is used as a reference to optimize the production process by setting and ideal irradiation time.

If a thin target is used, so that the protons are not stopped therein, the production yield $Y(E)$ can be defined as

$$Y(E) = TTY(E) - TTY(E_{out}) \tag{2.14}$$

where E_{out} is the proton energy after the target, determined using SRIM [33].

Given a sample containing a mixture of N radioisotopes, the purity of the radionuclide of interest X is given by

$$P_X = \frac{A_X}{\sum_i^N A_i} \tag{2.15}$$

where A_i is the activity of the i-th radionuclide.

References

[1] S. Braccini et al. "The cyclotron laboratory and the RFQ accelerator in Bern". In: *AIP Conference Proceedings* 1530 (2013), pp. 189–196. DOI: 10.1063/1.4812922.

[2] S. Braccini. "The new Bern PET cyclotron, its research beam line, and the development of an innovative beam monitor detector". In: *AIP Conference Proceedings* 1525 (2013), pp. 144–150. DOI: 10.1063/1.4802308.

[3] N. Savard et al. "Development of a Penning Ion Source Test Stand for Production of Alpha Particles". In: 10 (2019), pp. 1932–1935. DOI: 10.18429/JACoW-IPAC2019-TUPTS004.

[4] W. Kleeven. "Injection and extraction for cyclotrons". In: *CAS 2005 - CERN Accelerator School: Small Accelerators* (2006), pp. 271–296.

[5] S. Braccini. *Particle Accelerators and Detectors for medical Diagnostics and Therapy*. 2016. DOI: 10.48550/ARXIV.1601.06820.

[6] V. Colard. "Stripping member, a stripping assembly and a method for extracting a particle beam from a cyclotron". In: *US Patent* 8432090B2 (2013).

[7] J. Anders et al. "A facility for radiation hardness studies based on a medical cyclotron". In: *Journal of Instrumentation* 17.04 (2022), P04021. DOI: 10.1088/1748-0221/17/04/p04021.

[8] S. Braccini et al. "A novel experimental approach to characterize neutron fields at high- and low-energy particle accelerators". In: *Scientific Reports* 12 (1 2022), p. 16886. DOI: 10.1038/s41598-022-21113-7.

[9] S. Braccini. "Compact medical cyclotrons and their use for radioisotope production and multi-disciplinary research". In: *21st International Conference on Cyclotrons and their Applications (CYC2016), Zurich, Switzerland*. 2017, pp. 229–234. DOI: 10.18429/JACoW-Cyclotrons2016-TUD01.

[10] M. Auger et al. "Low current performance of the Bern medical cyclotron down to the pA range". In: *Meas. Sci. Technol.* 26 (2015). DOI: 10.1088/0957-0233/26/9/094006.

[11] P. Casolaro. "Radiochromic Films for the Two-Dimensional Dose Distribution Assessment". In: *Applied Sciences* 11.5 (2021). ISSN: 2076-3417. DOI: 10.3390/app11052132.

[12] G. Dellepiane et al. "New methods for theranostic radioisotope production with solid targets at the Bern medical cyclotron". In: *EPJ Web Conf.* 261 (2022), p. 05006. DOI: 10.1051/epjconf/202226105006.

[13] G. Dellepiane et al. “Research on theranostic radioisotope production at the Bern medical cyclotron”. In: *IL NUOVO CIMENTO C* 44 (2021). DOI: 10.1393/ncc/i2021-21130-6.

[14] S. Braccini et al. “Novel Irradiation Methods for Theranostic Radioisotope Production With Solid Targets at the Bern Medical Cyclotron”. In: *22nd International Conference on Cyclotrons and their Applications (CYC2019), Cape Town, South Africa*. 2020, pp. 127–131. DOI: 10.18429/JACoW-Cyclotrons2019-TUA02.

[15] M. Dehnel et al. “An integrated self-supporting Mini-Beamline for PET cyclotrons”. In: *20th International Conference on Cyclotrons and their Applications (CYC2013), Vancouver, BC, Canada*. 2013, pp. 251–253.

[16] P. D. Häffner et al. “A Novel Automatic Focusing System for the Production of Radioisotopes for Theranostics”. In: *12th International Particle Accelerator Conference (IPAC2021), Online format*. 2021, pp. 2480–2482. DOI: 10.18429/JACoW-IPAC2021-TUPAB408.

[17] P. Casolaro et al. “An Automatic Focalization System for Enhanced Radioisotope Production with Solid Targets”. In: *10th International Beam Instrumentation Conference (IBIC2021), Online Format*. 2021, pp. 150–153. DOI: 10.18429/JACoW-IBIC2021-MOPP38.

[18] P. D. Häffner et al. “An Active Irradiation System with Automatic Beam Positioning and Focusing for a Medical Cyclotron”. In: *Applied Sciences* 11.6 (2021). DOI: 10.3390/app11062452.

[19] P. D. Häffner. “Beam characterisation studies and development of a novel irradiation system at the Bern medical cyclotron”. PhD thesis. University of Bern, Switzerland, 2021.

[20] S. Braccini et al. “A beam monitor detector based on doped silica and optical fibres”. In: *Journal of Instrumentation* 7.02 (2012), T02001–T02001. DOI: 10.1088/1748-0221/7/02/t02001.

[21] M. Auger et al. “A detector based on silica fibers for ion beam monitoring in a wide current range”. In: *Journal of Instrumentation* 11.03 (2016), P03027–P03027. DOI: 10.1088/1748-0221/11/03/p03027.

[22] D. E. Potkins et al. “A low-cost beam profiler based on cerium-doped silica fibers”. In: *Proceedings of CAARI-16, Physics Procedia*. Vol. 70. 2017, pp. 215 –222. DOI: 10.1016/j.phpro.2017.09.061.

[23] Mirion Technologies. *GENIE 2000 - Basic Spectroscopy Software*. Last access 12 October 2022. URL: https://www.mirion.com/products/genie-2000-basic-spectroscopy-software.

[24] A. Forgács et al. “Excel2Genie: A Microsoft Excel application to improve the flexibility of the Genie-2000 Spectroscopic software”. In: *Applied Radiation and Isotopes* 94 (2014), pp. 77–81. DOI: 10.1016/j.apradiso.2014.07.005.

[25] Sandia National Laboratories. *InterSpec - spectral radiation analysis software*. Last access 12 October 2022. URL: https://sandialabs.github.io/InterSpec/.

[26] M. A. Hammed et al. “Analytical peak fitting for gamma-ray spectrum analysis with Ge detectors”. In: *Nuclear Instruments and Methods in Physics Research Section A: Accelerators, Spectrometers, Detectors and Associated Equipment* 334.2 (1993), pp. 543–550. DOI: 10.1016/0168-9002(93)90819-4.

[27] K. P. Nesteruk et al. “A system for online beam emittance measurements and proton beam characterization”. In: *Journal of Instrumentation* 13.01 (2018), P01011. DOI: 10.1088/1748-0221/13/01/p01011.

[28] K. P. Nesteruk et al. “Measurement of the Beam Energy Distribution of a Medical Cyclotron with a Multi-Leaf Faraday Cup”. In: *Instruments* 3.1 (2019). ISSN: 2410-390X. DOI: 10.3390/instruments3010004.

[29] L. Campajola et al. “Measurement of the proton beam energy of a medical cyclotron based on Rutherford Back-scattering Analysis”. In: *Nuclear Instruments and Methods in Physics Research Section B: Beam Interactions with Materials and Atoms* 440 (2019), pp. 114–117. DOI: 10.1016/j.nimb.2018.12.017.

[30] P. D. Häffner et al. “Study of the Extracted Beam Energy as a Function of Operational Parameters of a Medical Cyclotron”. In: *Instruments* 3.4 (2019). DOI: 10.3390/instruments3040063.

[31] S. J. C. do Carmo et al. “Simple, Immediate and Calibration-Free Cyclotron Proton Beam Energy Determination Using Commercial Targets”. In: *Instruments* 3.1 (2019). ISSN: 2410-390X. DOI: 10.3390/instruments3010020.

[32] T. S. Carzaniga et al. “Measurement of ^{43}Sc and ^{44}Sc production cross-section with an 18 MeV medical PET cyclotron”. In: *Applied Radiation and Isotopes* 129 (2017), pp. 96 –102. DOI: 10.1016/j.apradiso.2017.08.013.

[33] J. F. Ziegler and J. M. Manoyan. “The stopping of ions in compounds”. In: *Nucl. Instrum. Methods B* 35 (2013), p. 215. URL: http://www.srim.org.

CHAPTER 3

Novel Medical Radionuclides and their Optimized Production with Solid Targets

As discussed in Chapter 1, the availability of novel radionuclides for theranostics is of paramount importance for the development of nuclear medicine. In contrast with the production of standard radioisotopes with liquid targets, as ^{18}F, the production of such radionuclides in quantity and quality suitable for clinical applications is challenging and remains an open issue.

A possible solution is the use of medical cyclotrons equipped with a solid target station, which however requires the careful investigation of several aspects:

- Nuclear data: the knowledge of the cross sections involved is crucial for setting the energy range that optimizes the production yield and the radionuclidic purity. Data available in the literature are sometimes lacking or inconsistent.
- Proper and cost effective targetry: the use of rare and expensive isotopically enriched materials, usually available in powder form, is often required. It is therefore important to carefully design the target to be irradiated.
- Irradiation techniques: the knowledge of the beam characteristics is of paramount importance when dealing with small solid targets. The position and shape of the beam must be monitored during the irradiation and corrected, if necessary, to keep the beam on target and avoid unwanted activation of the system. The precise measurement of the pristine beam energy and of the cross sections involved allows to optimize the radionuclidic purity. The target must be contained in special capsules during the irradiation and properly cooled to prevent overheating.

- Chemical processing: the chemical separation procedure should be as simple as possible and provide no-carried-added (n.c.a) products [1]. Recovery techniques aimed at recycling the enriched material should be developed.

- Radiolabeling and quality control: a highly efficient radiolabeling process should be established. The final product must meet the quality criteria set by the European Pharmacopoeia, which cover radiochemical purity, specific activity, radionuclidic purity and chemical purity.

During my PhD, I focused on the first three aspects which deal with physics. In particular, I contributed significantly to enhance the knowledge of nuclear data by measuring for the first time several of the nuclear reaction cross sections to produce novel radionuclides for medical applications, especially for theranostics. On the basis of the results obtained, I performed a detailed study of the radioisotopic impurities formed during the irradiation, in order to assess the conditions that optimize the radionuclide production.
I investigated both diagnostic (β^+ and γ emitters) and therapeutic (β^- and Auger-electron emitters) radionuclides that are promising in nuclear medicine and can be produced with solid targets using an 18 MeV cyclotron.

This chapter reviews the medical applications of each radioisotope, while focusing mainly on the cross section measurements of the selected nuclear reactions and on the optimization of the production procedures. The detailed description of the experiments and of the data analysis can be found in the cited papers, in which I am the first author or one of the authors.

With regard to β^+ emitters, the production of ^{68}Ga by proton irradiation of solid zinc targets is described. ^{68}Ga is a clinically approved radionuclide with almost ideal characteristics for PET imaging and, for this reason, it is used as a comparison term for the other PET radiometals produced in this PhD work, namely ^{44}Sc, ^{61}Cu and ^{64}Cu. It is important to mention that, due to its unique decay pattern, ^{64}Cu also finds application in the therapeutic field, earning the name of theranostic agent [2]. In the case of SPECT imaging, the cyclotron-based production route of ^{99m}Tc and ^{155}Tb from molybdenum and gadolinium targets, respectively, is investigated.
In the field of therapeutic radionuclides, the production of the β^- emitters ^{47}Sc and ^{67}Cu, promising alternatives to the clinically established ^{177}Lu, and of the Auger-electron emitters ^{165}Er and ^{167}Tm is proposed.

The radionuclides I investigated are presented according to their atomic number. The nuclear information provided was retrieved from the Live Chart of Nuclides website by IAEA [3]. The natural isotopic composition of the elements were retrieved from the Table of Isotopic Compositions of the Elements by CIAAW [4].

The results obtained in this study for cross section measurements were compared with the TENDL-2021 predictions [5] and with the experimental data available in the literature and accessible via the EXFOR database [6].
In accordance with the findings of Takács et al. [7], the values presented by Levkovski in Ref. [8] are scaled by a factor 0.8, on the basis of the currently accepted value of the monitor reaction that was used in the original work. In this chapter, the corrected reference is cited as Levkovski 1991*.

3.1 Scandium radioisotopes

The true theranostic pairs ^{43}Sc/^{47}Sc and ^{44}Sc/^{47}Sc are considered among the most promising for the future of personalized nuclear medicine. This thesis focuses on ^{44}Sc and ^{47}Sc, as the production of ^{43}Sc was previously investigated at the Bern medical cyclotron [9].

^{44}Sc [$t_{1/2}$ = 3.97 h, $\bar{E}_{\beta^+}$ = 632 keV (94.3%), E_γ = 1157 keV (99.9%); 1499 keV (0.91%)] is a β^+ emitter with interesting decay properties for PET imaging and it was proposed as an alternative to ^{68}Ga for pre-therapeutic imaging and monitoring the response to radionuclide therapy [10]. Its half-life of about 4 h makes it suitable to label molecules with a relatively long biological half-life, covering several hours after the administration of the radioactive compound [11]. Furthermore, it would allow centralized production and cost-efficient distribution of ^{44}Sc-labelled radiopharmaceuticals to distant PET centers.
Due to the almost simultaneous emission of high-energy γ-rays, ^{44}Sc was proposed as a candidate for a new nuclear imaging technique based on $\beta^+\gamma$ coincidences [12]. This technique would lead to improved image resolution, allowing the dose required for the examination to be reduced [13] and thus compensating for the increased dose absorbed by the patient due to the 1157-keV-γ-ray emission.

^{47}Sc [$t_{1/2}$ = 3.349 d, E_{β^-} = 162 keV (100%), E_γ = 159 keV (68.3%)] is a low-energy β^- emitter that could be suitable for RNT. The 159-keV γ-ray emission that follows the decay allows for SPECT imaging during treatment to detect the radiotracer distribution. From a physical and chemical point of view, ^{47}Sc is similar to the clinically-established ^{177}Lu [$t_{1/2}$ = 6.64 d, E_{β^-} = 134 keV (100%), E_γ = 113 keV (6.2%); 208 keV (10.4%)]. However, its much shorter half-life would make ^{47}Sc ideal for labeling small-molecular-weight targeting ligands with a relatively fast blood clearance [14].

Many ^{44}Sc and ^{47}Sc production routes are reported in the literature, as shown in Table 3.1. Among them, the reactions ^{44}Ca(p,n)^{44}Sc, ^{48}Ca(p,2n)^{47}Sc and ^{48}Ca(p,pn)^{47}Ca $\rightarrow$ ^{47}Sc were also investigated at the Bern medical cyclotron in a previous research project [9, 15].

Impinging particle	Target	Route
p	^{44}Ca	^{44}Ca(p,n)^{44}Sc [9, 10, 16]
	^{46}Ca	^{46}Ca(p,γ)^{47}Sc
	^{48}Ca	^{48}Ca(p,2n)^{47}Sc, ^{48}Ca(p,pn)^{47}Ca $\rightarrow$ ^{47}Sc [15–17]
	^{47}Ti	^{47}Ti(p,α)^{44}Sc [18]
	^{48}Ti	^{48}Ti(p,2p)^{47}Sc [16]
	^{50}Ti	^{50}Ti(p,α)^{47}Sc [18]
	^{45}Sc	^{45}Sc(p,2n)^{44}Ti $\rightarrow$ ^{44}Sc [19, 20]
d	^{44}Ca	^{44}Ca(d,2n)^{44}Sc [16]
	^{46}Ca	^{46}Ca(d,n)^{47}Sc
	^{49}Ti	^{49}Ti(d,α)^{47}Sc
α	^{42}Ca	^{42}Ca(α,d)^{44}Sc [21]
	^{44}Ca	^{44}Ca(α,x)^{47}Sc [22]
γ	^{48}Ca	^{48}Ca (γ,n)^{47}Sc [23]
	^{48}Ti	^{48}Ti(γ,p)^{47}Sc [24, 25]
n	^{46}Ca	^{46}Ca(n,γ)^{47}Sc [14, 26]
	^{48}Ca	^{48}Ca(n,2n)^{47}Ca $\rightarrow$ ^{47}Sc
	^{47}Ti	^{47}Ti(n,p)^{47}Sc [26–28]

Table 3.1: Main production routes for ^{44}Sc and ^{47}Sc reported in the literature.

With reference to the production of ^{44}Sc from enriched ^{44}Ca, during my PhD I was involved in targetry optimization, testing two new target preparation methods. Infact, despite the use of $CaCO_3$ targets for ^{44}Sc production is widely reported in the literature [10, 16], this material was found to be unsuitable for irradiations at the Bern medical cyclotron due to radioprotection issues. During the irradiation, the increase of the pellet temperature caused the decomposition of $CaCO_3$ into CaO and CO_2, leading to a progressive rise in pressure inside the coin and allowing the radioactive gas ^{13}N, produced by the ^{16}O(p,α)^{13}N reaction, to escape from the coin. The air contamination in the cyclotron bunker caused the ventilation to shut down, stopping the irradiation.
For this reason, it was necessary to investigate the use of different materials.

In the framework of a collaboration with PSI, the use of CaO pellets, obtained from thermal decomposition of $CaCO_3$, was tested. As shown in Figure 3.1, the use of CaO targets was found to be an improvement, with the amount of gas released not exceeding the quantity of ^{41}Ar produced during normal ^{18}F production (100-150 kBq/m^3). However, the handling of these targets still requires special care. Due to the high hygroscopicity of CaO, the pellet must be prepared and stored under Ar atmosphere and irradiated as soon as possible to prevent it from swelling (Figure 3.2).

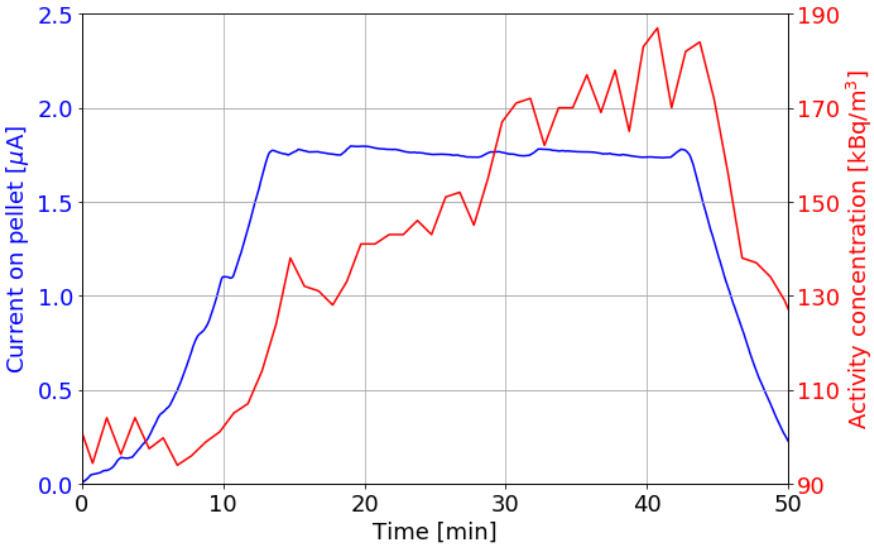

Figure 3.1: Exhaust radioactivity in air of the cyclotron bunker during a typical irradiation of a CaO target for ^{44}Sc production.

Figure 3.2: Example of CaO pellet exposed to air.

Radioisotope	$t_{1/2}$	Decay mode: [%]	E_γ [keV]	BR [%]
^{43}Sc	3.891*(12)* h	ec + β^+: 100	372.9*(3)*	22.5*(7)*
^{44}Sc	3.97*(4)* h	ec + β^+: 100	1499.46*(2)*	0.908*(15)*
^{44m}Sc	58.61*(10)* h	IT: 98.8	271.240*(10)*	86.75*(6)*
^{46}Sc	83.79*(4)* d	β^-: 100	889.277*(3)*	99.984*(1)*
^{47}Sc	3.3492*(6)* d	β^-: 100	159.381*(15)*	68.3*(4)*

Table 3.2: Decay properties and main γ emissions of scandium radioisotopes. The values in parentheses are the uncertainties referred to the last digits of the value.

A series of irradiations were successfully carried out, producing several GBq of ^{44}Sc. In particular, about 15 GBq of ^{44}Sc were produced for the first time with a medical cyclotron by irradiating a 0.5-mm-thick 97.0% enriched ^{44}CaO pellet with about 26 μAh.

The produced activity was shipped to PSI to undergo radiochemical dissolution and separation procedures [10], resulting in high radionuclidic and chemical purity. The ^{44}Sc eluate was then used for a preclinical study, labelling the PSMA-ALB-02 ligand [29] and successfully performing imaging studies with a small animal PET/CT scanner [30]. The detailed description of the production tests, the radiochemical procedures and the preclinical applications of ^{44}Sc-PSMA-ALB-02 can be found in Ref. [31], which I co-authored.

Pellets produced with the same procedure were used in the context of a collaboration with PSI and IRA to precisely determine the half-life of ^{44}Sc and of its metastable state ^{44m}Sc (Table 3.2).

Two samples of ^{44}Sc solution with different activity concentrations, produced and purified at PSI, were sent to IRA and accurately measured under metrological conditions using different methodologies. An aliquot of less concentrated solution was sent to the Bern medical cyclotron laboratory to be measured with the HPGe detector. I repeatedly measured the sample for about 70 h, changing the distance from the detector over time so that the counts frequency was low enough to limit the negative effects of pile up and random summing.

I calculated the half-life of ^{44m}Sc by fitting the experimental data with the simple exponential decay equation:

$$A_{44m}(t) = A_{44m}(t_0)e^{-\lambda_{44m}t} \tag{3.1}$$

resulting in λ_{44m} = (3.29 $\pm$ 0.01)$\cdot 10^{-6}$ s^{-1}.

To determine the ^{44}Sc half-life, it was necessary to account for the contribution to its activity of ^{44m}Sc, decaying into the ground state through internal transition. For this reason, I fitted the measured activities with the Bateman equation

$$A_{44}(t) = A_{44}(t_0)e^{-\lambda_{44}t} + \frac{\lambda_{44}}{\lambda_{44} - \lambda_{44m}} A_{44m}(t_0)(e^{-\lambda_{44m}t} - e^{-\lambda_{44}t}) \qquad (3.2)$$

where λ_{44m} is a constant parameter equal to the previously obtained value.
The result of the fit 3.2 was λ_{44} = (4.75 ± 0.02)·10^{-5} s^{-1}.
The experimental data and fit curves are presented in Figure 3.3 with their corresponding residuals. In the case of ^{44}Sc, the data measured after 20 h were discarded due to the low statistics of the 1499 keV emission.
My findings were compatible with the values measured at IRA, confirming the validity of the HPGe calibration.

This study provided a half-life of 58.7*(3)* h and 4.042*(7)* h for ^{44m}Sc and ^{44}Sc, respectively. A detailed description of the activity measurements, the half-life determination and the uncertainty evaluation can be found in Ref. [32], which I co-authored.

In view of a wider application of cyclotron-produced ^{44}Sc in nuclear medicine, it is necessary to develop a methodology for the precise measurement of the produced activity and for the identification of possible Sc impurities in the sample. The activity measurements performed at IRA under metrological conditions were also used for the calibration of the dose calibrators at PSI. In this case, it was proved that the contribution of ^{44m}Sc can be neglected in activity determination performed with the dose calibrator, if the measurement is carried out within 12 h after the EoB. This corresponds to approximately three times the half-life of ^{44}Sc and it is longer than the expected time for medical application.

The detailed description of this work is reported in Ref. [33], which I co-authored.

A different kind of Ca target, produced by the University of Debrecen, Hungary, was tested for the production of ^{44}Sc at the Bern medical cyclotron in the framework of a collaboration between the two institutes.
In this case, to improve the heat conductivity of the target, 10 mg of natural $CaCO_3$ powder were mixed with 20 mg of natural Mg powder and pressed into a disc-shaped pellet (6 mm in diameter, 0.7 mm thick). It was then placed inside a coin and mailed to Bern without any special precautions in storing, which did not cause any swelling or fractures (Figure 3.4).

The pellet was irradiated with a constant current of about 4 μA for 37 min, during which a negligible release of radioactive gas was observed (Figure 3.5).

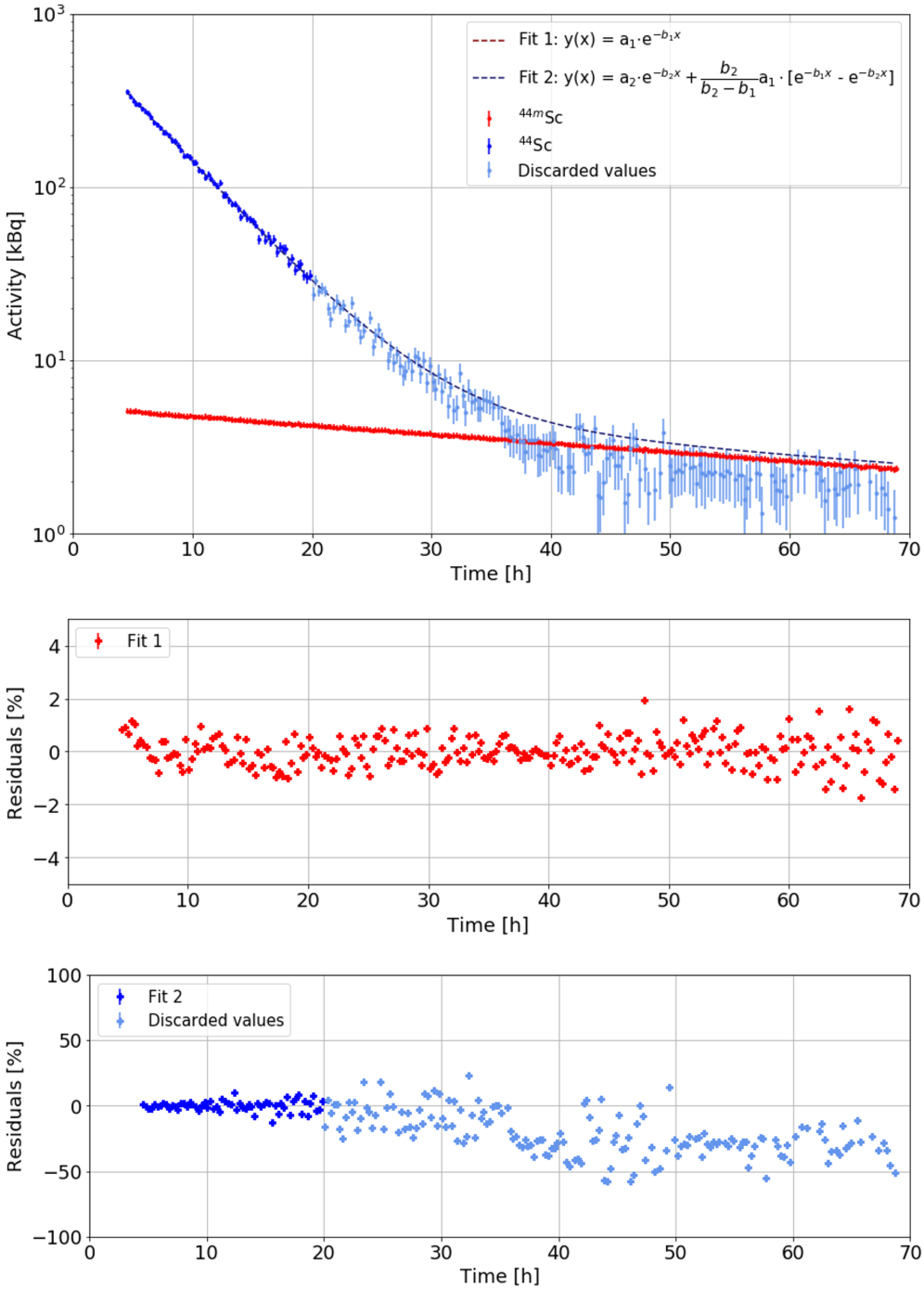

Figure 3.3: Activities of ^{44}Sc and ^{44m}Sc measured over time from the 1499 keV and 291 keV, respectively, and fit curves with the corresponding residuals.

The measured scandium radioisotope activities were compatible within the uncertainties with the predictions made on the basis of the experimental cross sections [9, 15].

Further studies are planned, in particular the use of enriched $^{44}CaCO_3$ for an optimized ^{44}Sc production.

Figure 3.4: Natural $Mg/CaCO_3$ pellet before irradiation.

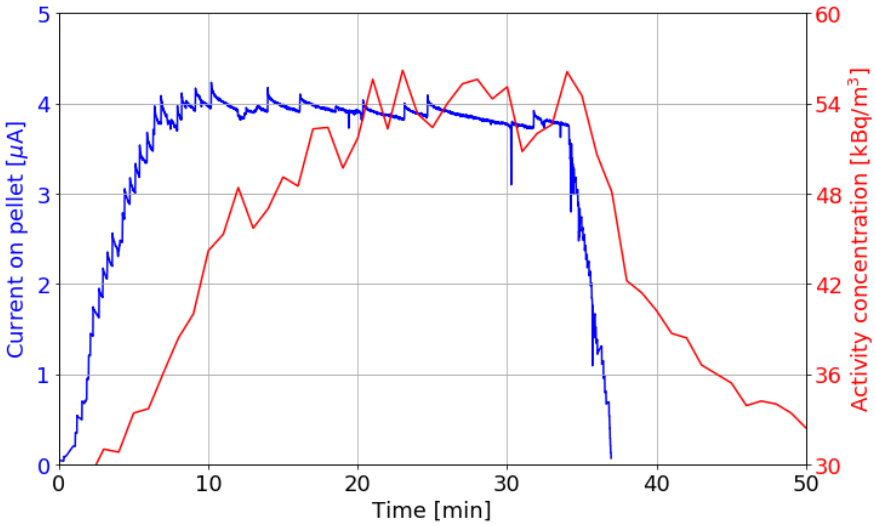

Figure 3.5: Exhaust radioactivity in air of the cyclotron bunker during the $Mg/CaCO_3$ target irradiation for ^{44}Sc production.

During my PhD, I also investigated the production of ^{44}Sc and ^{47}Sc by irradiating enriched ^{47}Ti and enriched ^{50}Ti targets, respectively, exploiting the ^{47}Ti(p,α)^{44}Sc and ^{50}Ti(p,α)^{47}Sc reactions. The isotopic compositions of the materials used in this study are reported in Table 3.3.

The results of the nuclear cross section measurements are shown in Figure 3.6-Figure 3.10, together with TENDL predictions [5] and the experimental data available in the literature [8, 34]. The unpublished cross section data of the ^{47}Ti(p,αn)^{43}Sc, ^{47}Ti(p,α)^{44}Sc, ^{47}Ti(p,α)^{44m}Sc, ^{47}Ti(p,2p)^{46}Sc and ^{48}Ti(p,2p)^{47}Sc reactions are reported in the Appendix for completeness.

	^{46}Ti	^{47}Ti	^{48}Ti	^{49}Ti	^{50}Ti
Natural Ti [%]	8.0	7.3	73.8	5.5	5.4
Enr. $^{47}TiO_2$ [%]	0.41	95.70	3.57	0.18	0.14
Enr. $^{50}TiO_2$ [%]	<0.01	<0.01	0.23	4.57	95.20

Table 3.3: Isotopic fractions of the natural Ti foil purchased by GoodFellow [35], the enriched $^{47}TiO_2$ and the enriched $^{50}TiO_2$ powders supplied by Isoflex [36].

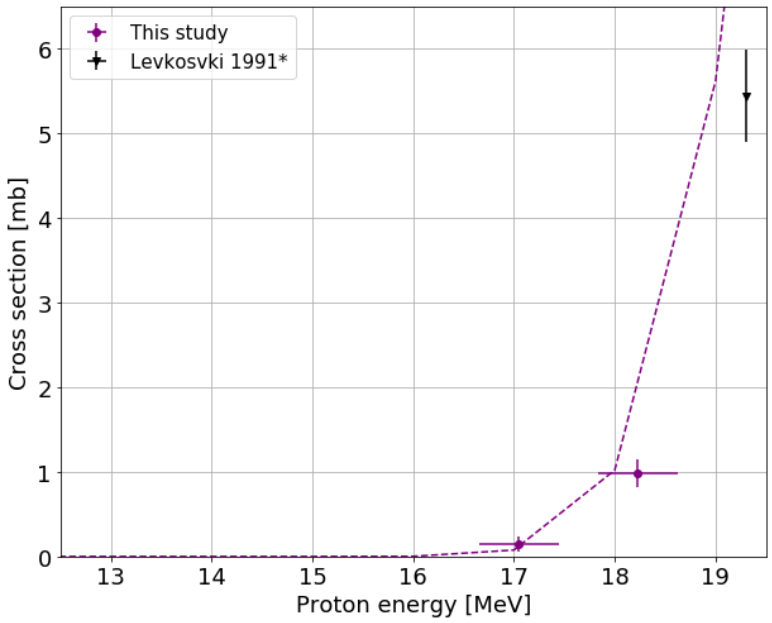

Figure 3.6: ^{47}Ti(p,αn)^{43}Sc reaction cross sections.

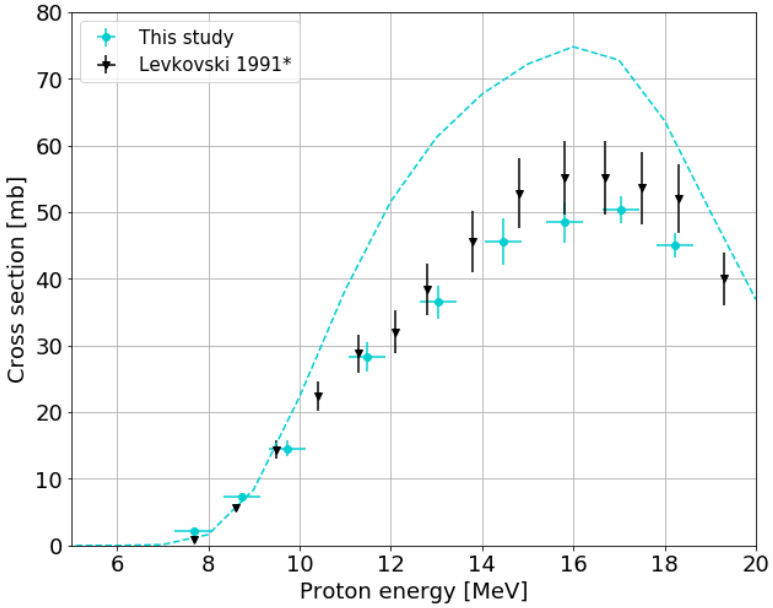

Figure 3.7: ^{47}Ti(p,α)^{44}Sc reaction cross sections.

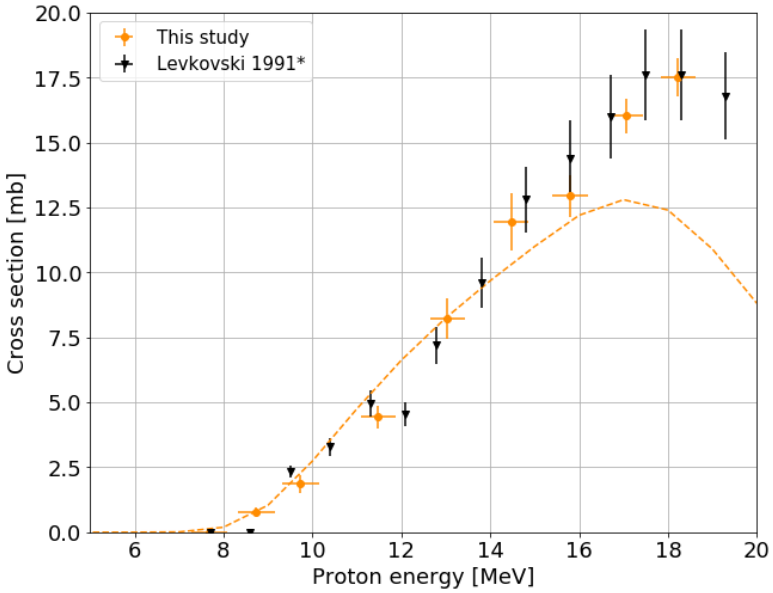

Figure 3.8: ^{47}Ti(p,α)^{44m}Sc reaction cross sections.

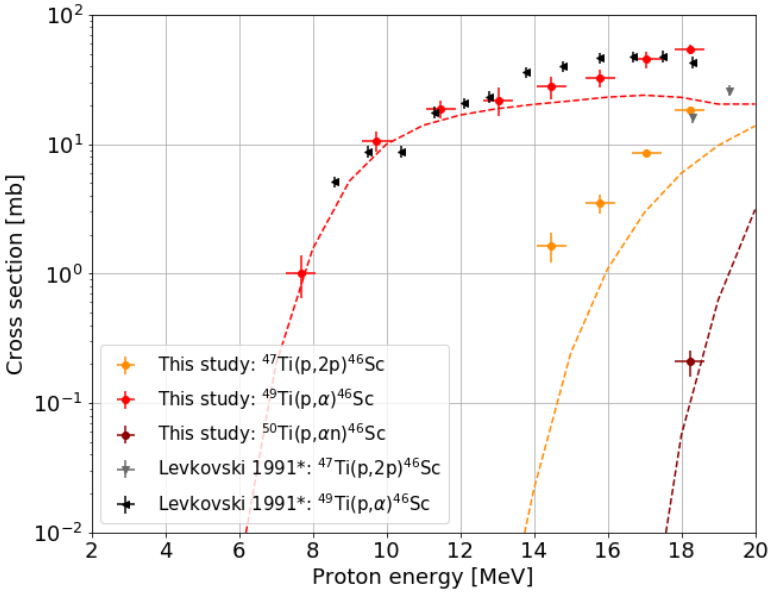

Figure 3.9: ^{47}Ti(p,2p)^{46}Sc, ^{49}Ti(p,α)^{46}Sc and ^{50}Ti(p,αn)^{46}Sc reaction cross sections.

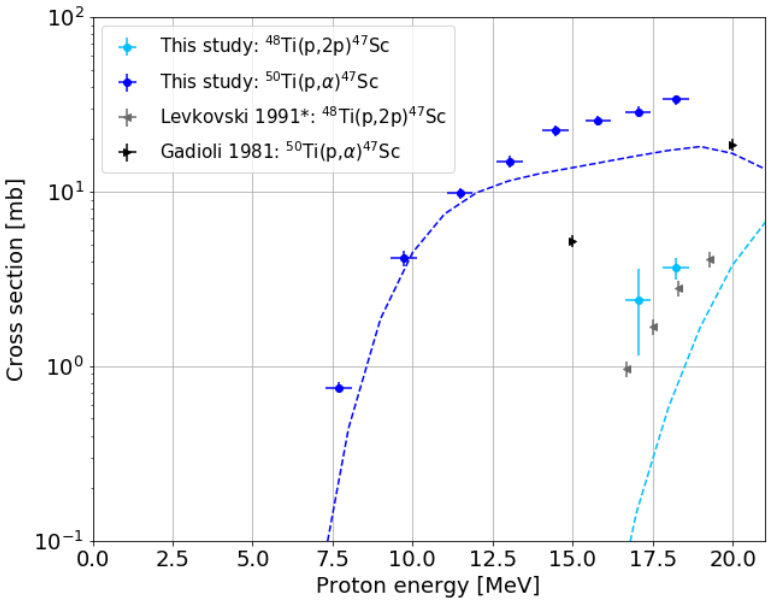

Figure 3.10: ^{48}Ti(p,2p)^{47}Sc and ^{50}Ti(p,α)^{47}Sc reaction cross sections.

To optimize the production of the radioisotope of interest, a study of the yield and the radionuclidic purity was carried out on the basis of the cross section measurements.

Scandium-44 The irradiation of a 95.70% enriched $^{47}TiO_2$ target results in the production of several scandium radioisotopes. Among them, ^{44m}Sc, ^{46}Sc and ^{47}Sc have longer half-lives than ^{44}Sc and cannot be removed from the sample by means of decay time.

As shown in Figure 3.11, the production of ^{46}Sc and ^{47}Sc can be minimized by setting the beam input energy below the threshold energy of the $^{47}Ti(p,2p)^{46}Sc$ and $^{48}Ti(p,2p)^{47}Sc$ reactions (Figure 3.9 and Figure 3.10, respectively). The latter contribution can be further reduced by considering higher enriched materials. The co-production of the metastable state ^{44m}Sc cannot be avoided and it represents the main impurity. The presence of this longer-lived metastable state leads to the decrease in radionuclidic purity over time, limiting the period of application of the labelled compound, and complicates patient dosimetry. ^{43}Sc has a half-life comparable to ^{44}Sc (Table 3.2) and is characterized by the high emission of low-energy positrons ($\bar{E}_{\beta^+}$ = 508 keV (70.9%); 632 keV (17.2%)) without any high-energy γ-ray. It therefore produces no image degradation effects nor does it lead to an increase in the dose absorbed by the patient. Despite these premises, further studies need to be carried out to determine how the presence of ^{43}Sc in the sample affects the imaging performance. For this reason, ^{43}Sc is considered as an impurity in the yield calculations below.

Figure 3.12 shows the ^{44}Sc TTY and the radionuclidic purity as a function of the entry energy. For an input energy of 15 MeV, which provides a good balance between production yield and radionuclidic purity, a ^{44}Sc TTY of 48 MBq/μAh with a purity of 98.2% can be achieved.

To obtain larger ^{44}Sc activities, longer irradiation times can be considered. In this case, however, the increased production of long-lived radionuclides, in particular ^{44m}Sc, must be taken into account (Figure 3.13).

The calculations based on the cross section measurements were confirmed by irradiating a 0.97-mm-thick enriched $^{47}TiO_2$ pellet in the BTL, by means of a modified version of the station used for cross section measurements.

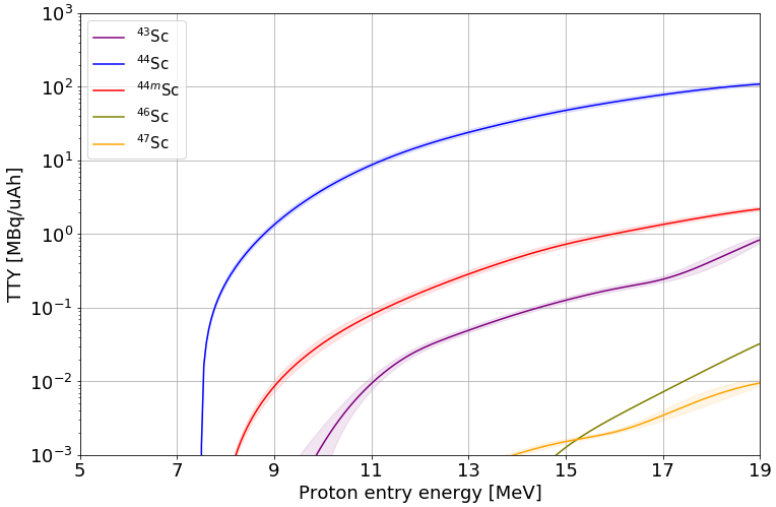

Figure 3.11: Thick target yield of Sc radioisotopes as a function of the proton entry energy. The bands correspond to the maximum and minimum yield derived from the measured cross sections.

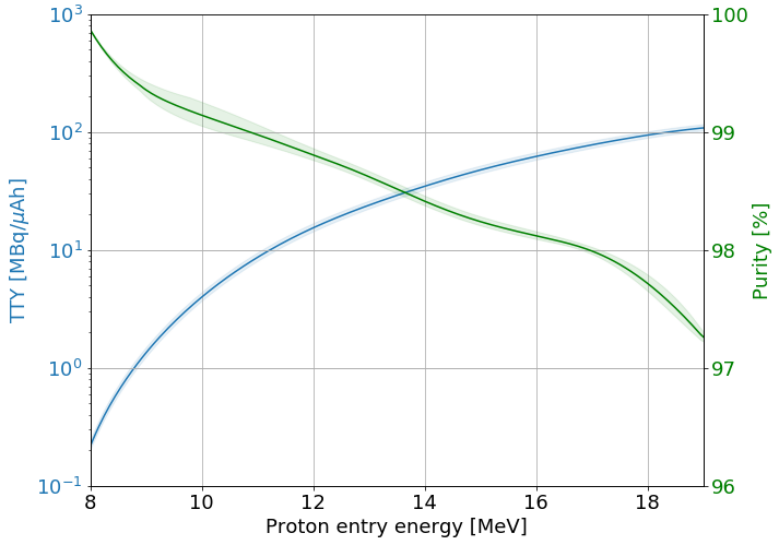

Figure 3.12: ^{44}Sc thick target yield and radionuclidic purity as a function of the proton entry energy. The bands correspond to the maximum and minimum yield derived from the measured cross sections.

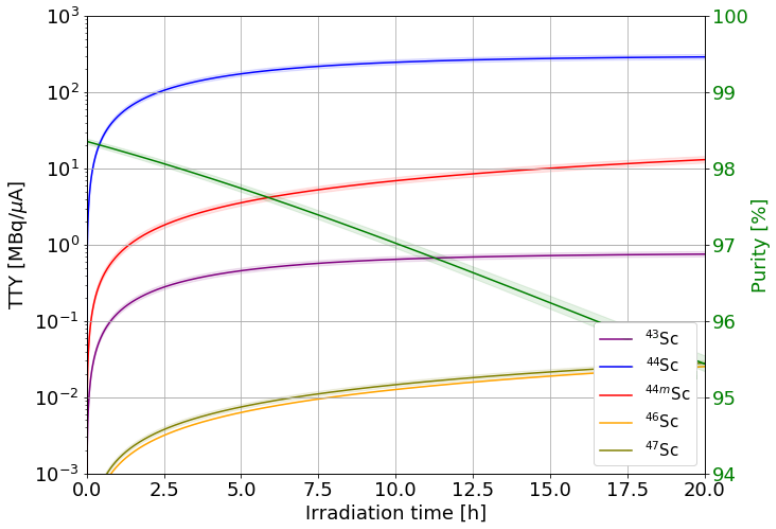

Figure 3.13: Thick target yield of Sc radioisotopes and radionuclidic purity as a function of the irradiation time. The bands correspond to the maximum and minimum yield derived from the measured cross sections.

The irradiation parameters, the activities produced and the radionuclidic purity at the EoB are reported in Table 3.4. The results obtained are shown in Figure 3.14 together with the predictions based on the cross section measurements, calculated under irradiation conditions.

Further production tests ad checks are planned. The results of this study will be published in a forthcoming paper, of which I will be the first author.

The ^{47}Ti(p,α)^{44}Sc reaction provides a lower production yield and radionuclidic purity compared to the ^{44}Ca(p,n)^{44}Sc. However, the higher isotopic abundance of ^{47}Ti compared to ^{44}Ca (7.4% vs. 2.1%) and the easier handling of the target could make this production route a promising alternative. Furthermore, according to the findings of Loveless et al. [18], TiO_2 targets can tolerate very high beam currents, allowing to achieve higher activities.

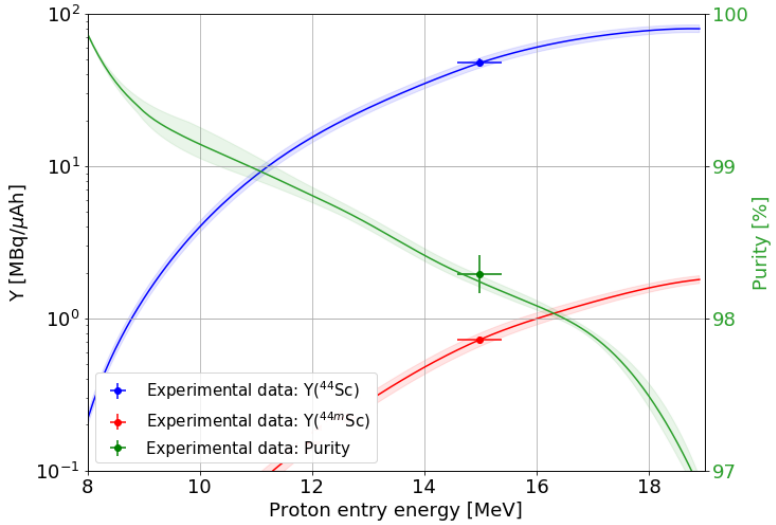

Figure 3.14: ^{44}Sc and ^{44m}Sc yields and radionuclidic purity calculated in our irradiation conditions compared to the experimental results. The bands correspond to the maximum and minimum yield derived from the measured cross sections.

E_{in} [MeV]	Q 10^{-3} [μAh]	Y(^{44}Sc) [MBq/μAh]	Y(^{44m}Sc) [MBq/μAh]	P(EoB) [%]
(15.0 ± 0.4)	0.63 ± 0.03	48 ± 3 *(47)*	0.73 ± 0.04 *(0.72)*	98.3 ± 0.1 *(98.2)*

Table 3.4: Irradiation parameters, ^{44}Sc and ^{44m}Sc yields and radionuclidic purity at the EoB, obtained irradiating the 95.70% enriched $^{47}TiO_2$ pellet. The values in parentheses are the yield calculations based on cross section measurements.

Scandium-47 By irradiating an enriched ^{50}TiO thick target, the maximum ^{47}Sc production yield can be obtained at the highest achievable proton energy. The radionuclidic purity is affected by the co-production of the long-lived ^{46}Sc, which increases for longer irradiation times.

According to our findings, a ^{47}Sc TTY of 249 MBq/μA with a purity of 99.2% can be achieved at saturation, assuming an input energy of 17.8 MeV (Figure 3.15). Considering these irradiation conditions, I investigated the variation of radionuclidic purity as a function of decay time in order to assess the impact of ^{46}Sc on the possible application period of the ^{47}Sc-labelled radiopharmaceutical.
From Figure 3.16 it can be seen that the purity remains above 99% for about 24 h after the EoB. At that time, the residual activity of ^{47}Sc is ~80%.

Although under the same irradiation conditions the ^{50}Ti(p,α)^{47}Sc reaction provides a lower yield than the ^{48}Ca(p,2n)^{47}Sc (0.25 GBq/μA vs. 12 GBq/μA), the radionuclidic purity is significantly higher (99% vs. 87%) [15]. Moreover, the higher natural isotopic abundance of ^{50}Ti compared to ^{48}Ca (5.4% vs. 0.19%) makes it more widely available at an affordable price.

To obtain higher activities, the use of more energetic proton beams (20–24 MeV) can be evaluated, as the ^{47}Sc cross section was found to be increasing at 18 MeV. In this case, however, the additional co-production of ^{46}Sc due to the ^{50}Ti(p,αn)^{46}Sc reaction must be taken into account. This contribution cannot be avoided by using higher enriched material and, according to TENDL [5], leads to an increase in the ^{46}Sc TTY from 4.8 kBq/μA to 58 kBq/μA, considering 18 and 24 MeV proton beams, respectively.

The calculations based on the cross section measurements were confirmed by irradiating a 0.28-mm-thick enriched $^{50}TiO_2$ pellet in the BTL. The target was placed in a special coin with a 7-mm-diameter hole in the front (Figure 3.17-a), in order not to degrade the beam energy.
To prevent the material from escaping during the irradiation, a 13-μm-thick aluminum foil was placed inside the coin (Figure 3.17-b), resulting in an input energy of (18.2 ± 0.4) MeV.

The irradiation parameters, the activities produced and the radionuclidic purity at the EoB are reported in Table 3.5. The results obtained are shown in Figure 3.18 together with the predictions calculated under irradiation conditions.

A more detailed description of the study about the ^{47}Sc production with solid targets carried out at the Bern medical cyclotron can be found in Ref. [37], of which I am the first author and which is reprinted in Part II of this thesis.

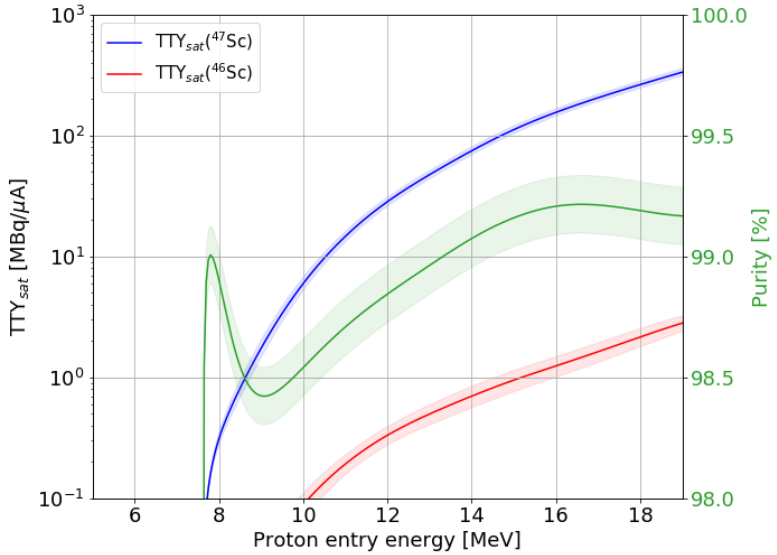

Figure 3.15: ^{47}Sc and ^{46}Sc thick target yields and radionuclidic purity at saturation as a function of the proton entry energy. The bands correspond to the maximum and minimum yield derived from the measured cross sections.

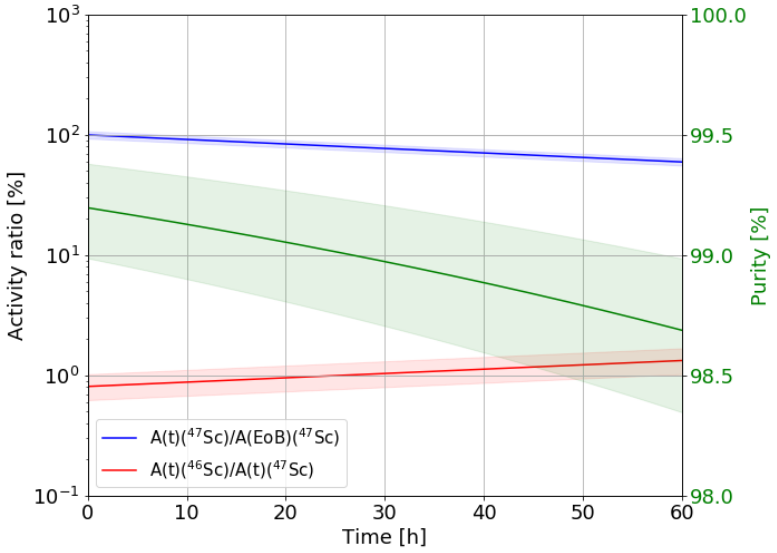

Figure 3.16: ^{46}Sc/^{47}Sc activity ratio, ^{47}Sc activity fraction and radionuclidic purity as a function of time. The EoB activities are calculated for an entry energy of 17.8 MeV at saturation. The bands correspond to the maximum and minimum yield calculated on the basis of the measured cross sections.

(a) (b)

Figure 3.17: (a) Coin with a 7-mm-diameter hole in the front, containing a 6-mm enriched $^{50}TiO_2$ pellet; (b) 13-μm-thick aluminum foil inserted in the coin to prevent the pellet leakage during the irradiation.

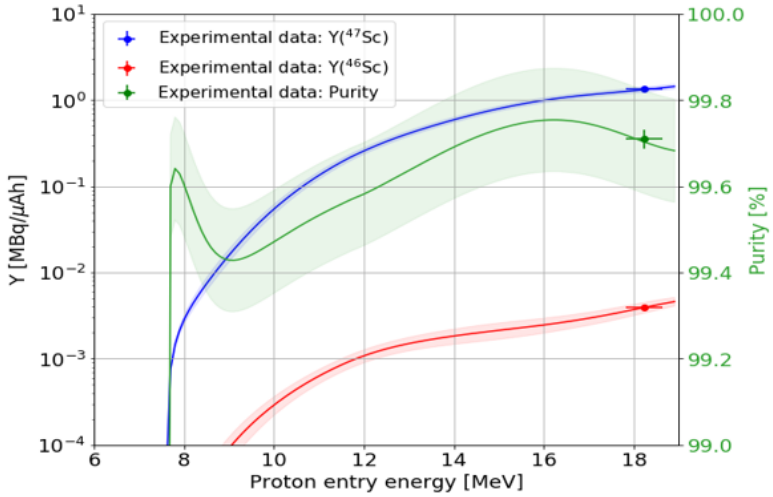

Figure 3.18: ^{47}Sc and ^{46}Sc yields and radionuclidic purity calculated under irradiation conditions and experimental results. The bands correspond to the maximum and minimum yield derived from the measured cross sections.

E_{in} [MeV]	Q 10^{-3} [μAh]	Y(^{47}Sc) [MBq/μAh]	Y(^{46}Sc) [MBq/μAh]	P(EoB) [%]
(18.2 ± 0.4)	3.9 ± 0.2	1.35 ± 0.07 *(1.33)*	0.0039 ± 0.0002 *(0.0039)*	99.71 ± 0.02 *(99.70)*

Table 3.5: Irradiation parameters, ^{47}Sc and ^{46}Sc yields and radionuclidic purity at the EoB, obtained irradiating the 95.20% enriched $^{50}TiO_2$ pellet. The values in parentheses are the yield calculations based on cross section measurements.

3.2 Copper radioisotopes

Copper is attracting increasing interest as it offers an almost unique selection of radioisotopes for imaging (^{60}Cu, ^{61}Cu, ^{62}Cu and ^{64}Cu) and targeted radionuclide therapy (^{64}Cu and ^{67}Cu), with a varying range of half-lives and decay modes (Table 3.6).

As part of my thesis, I focused on the production of ^{61}Cu, ^{64}Cu and ^{67}Cu, which form two of the most promising theranostic pairs, namely ^{61}Cu/^{67}Cu and ^{64}Cu/^{67}Cu.

Radioisotope	$t_{1/2}$	Decay mode: [%]	E_γ [keV]	BR [%]
^{60}Cu	23.7*(4)* min	ec + β^+: 100	826.4*(2)*	21.7*(11)*
^{61}Cu	3.339*(8)* h	ec + β^+: 100	282.956*(10)*	12.7*(20)*
^{62}Cu	9.67*(3)* min	ec + β^+: 100	1172.97*(10)*	0.342*(17)*
^{64}Cu	12.7006*(20)* h	ec + β^+: 61.5	1345.77*(6)*	0.472*(4)*
		β^-: 38.5	-	-
^{67}Cu	61.83*(12)* h	β^-: 100	184.577*(10)*	48.7*(3)*

Table 3.6: Decay properties and main γ emissions of copper radioisotopes. The values in parentheses are the uncertainties referred to the last digits of the value.

Among copper radioisotopes, ^{64}Cu is currently the most commonly used in clinical settings. It undergoes three different decays, namely electron capture (44.0%), β^- (38.5%) and β^+ (17.5%) decay, finding applications in both the diagnostic and therapeutic fields.
With regard to PET imaging, ^{64}Cu has a lower positron energy than ^{61}Cu (278 keV vs. 524 keV), leading to a better spatial resolution of the image, further enhanced by the absence of abundant γ-ray emissions. The lower abundance of emitted positrons (17.6% vs. 61% for ^{61}Cu) can be compensated by longer acquisition times. On the other hand, ^{61}Cu has no β^- emission, which contribute significantly to the radiation dose to the patient [38]. Furthermore, the 3.339 h half-life of ^{61}Cu fills the gap between ^{68}Ga (67.71 min) and ^{64}Cu (12.7006 h) and is favourable to study the kinetics of tracers that show maximum uptake 4 to 8 h post injection [39]. This makes ^{61}Cu particularly suitable for labelling small molecules which have fast biokinetics [40].

^{67}Cu is the longer-lived copper radioisotope and decays emitting a combination of low β^- particles [$\bar{E}_{\beta^-}$ = 121 keV (57%); 154 (22%); 189 (20%)] and γ-rays [E_γ = 185 keV (48.7%); 92 keV (23.1%)]. These characteristics make it suitable for RNT and allows for SPECT imaging to detect the radiotracer distribution during treatment. As ^{47}Sc, ^{67}Cu is similar to ^{177}Lu, however its shorter half-life (2.6 d

Impinging particle	Target	Route
p	^{61}Ni	^{61}Ni(p,n)^{61}Cu [42, 43]
	^{nat}Zn	^{nat}Zn(p,x)^{61}Cu [44–46]
	^{64}Zn	^{64}Zn(p,α)^{61}Cu [45]
	^{64}Ni	^{64}Ni(p,n)^{64}Cu [42, 47]
	^{66}Zn	^{66}Zn(p,2pn)^{64}Cu [48]
	^{67}Zn	^{67}Zn(p,α)^{64}Cu [49]
	^{68}Zn	^{68}Zn(p,αn)^{64}Cu [48, 50]
	^{65}Cu	^{65}Cu(p,pn)^{64}Cu
	^{68}Zn	^{68}Zn(p,2p)^{67}Cu [51, 52]
	^{70}Zn	^{70}Zn(p,α)^{67}Cu [50, 53, 54]
	^{68}Zn + ^{70}Zn	^{68}Zn(p,2p)^{67}Cu + ^{70}Zn(p,α)^{67}Cu [55]
d	^{nat}Ni	^{nat}Ni(d,x)^{61}Cu [56]
	^{nat}Zn	^{nat}Zn(d,x)^{64}Cu [50]
	^{70}Zn	^{70}Zn(d,x)^{67}Cu [57, 58]
α	^{nat}Ni	^{nat}Ni(α,x)^{61}Cu [59]
	^{59}Co	^{59}Co(α,2n)^{61}Cu [60, 61]
	^{64}Ni	^{64}Ni(α,p)^{67}Cu [62]
γ	^{65}Cu	^{65}Cu(γ,n)^{64}Cu [63]
	^{68}Zn	^{68}Zn(γ,x)^{70}Zn [64–66]
n	^{64}Zn	^{64}Zn(n,p)^{64}Cu [67–73]
	^{63}Cu	^{63}Cu(n,γ)^{64}Cu [67, 74]
	^{65}Cu	^{63}Cu(n,2n)^{64}Cu [72]
	^{67}Zn	^{67}Zn(n,p)^{67}Cu [68–71, 75]

Table 3.7: Main production routes for ^{61}Cu, ^{64}Cu and ^{67}Cu reported in the literature.

vs. 6.6 d) allows it to be used to label molecules with a faster washout from tumour tissues [41].

Many ^{61}Cu, ^{64}Cu and ^{67}Cu production routes are reported in the literature (Table 3.7). Nevertheless, the availability of ^{67}Cu in quantities and qualities suitable for clinical applications is still an open issue.

I investigated the possibility of producing these copper radionuclides from solid targets using an 18 MeV medical cyclotron, by measuring the cross section of the nuclear reactions involved. In particular, I studied the reaction ^{64}Zn(p,α)^{61}Cu by irradiating targets of natural Zn and enriched ^{64}Zn and comparing the impurities produced. For ^{64}Cu, I investigated alternative production methods to the very expensive ^{64}Ni(p,n)^{64}Cu reaction, namely ^{65}Cu(p,pn)^{64}Cu

	^{64}Zn	^{66}Zn	^{67}Zn	^{68}Zn	^{70}Zn
Natural Zn [%]	49.17	27.73	4.04	18.45	0.61
(*) Enr. ^{64}Zn [%]	99.40	0.39	0.04	0.17	<0.01
(**) Enr. ^{67}ZnO [%]	1.56	3.88	89.60	4.91	0.05
(**) Enr. ^{68}Zn [%]	0.99	0.81	0.38	97.80	0.02
(***) Enr. ^{70}ZnO [%]	0.02	0.01	0.02	1.20	98.75

Table 3.8: Isotopic fractions of the natural Zn powder purchased by GoodFellow [35] and the enriched Zn materials supplied by TRACE Sciences International [76] (*), Isoflex [36] (**) and CortecNet [77] (***).

	^{63}Cu	^{65}Cu
Enr. ^{65}CuO [%]	0.33	99.67

Table 3.9: Isotopic fractions of the enriched ^{65}CuO powder purchased by Isoflex [36].

and ^{67}Zn(p,α)^{64}Cu, which enable low and high ^{64}Cu specific activities, respectively. Finally, in the case of ^{67}Cu, I focused on the ^{70}Zn(p,α)^{67}Cu reaction by proton irradiation of enriched ^{70}ZnO targets.

By irradiating the materials reported in Table 3.8 and Table 3.9, I was able to measure all the cross sections of the nuclear reactions producing the investigated copper radioisotopes in the energy range of interest.

For ^{67}Cu, I developed a special data analysis procedure due to the production of ^{67}Ga through the ^{68}Zn(p,2n)^{67}Ga reaction. Although it does not affect the radionuclidic purity of ^{67}Cu, ^{67}Ga presents the same γ-lines and its contribution must be subtracted in the cross section calculations. Moreover, having a longer half-life, ^{67}Ga cannot be removed from the sample by means of decay time.

To correct the cross sections, I developed a method based on the inversion of a linear system of equations, considering the two most intense common γ-lines for ^{67}Cu and ^{67}Ga [E_γ = 93.3 keV (^{67}Ga: 38.8%, ^{67}Cu: 16.1%); E_γ = 184.6 keV (^{67}Ga: 21.4%, ^{67}Cu: 48.7%)].

By irradiating a sample at the proton energy E and by measuring the count rates $\rho(t)$ of the two peaks, the following linear system holds:

$$\begin{cases} \rho_{93}(t) = \sum_k A_k(t_0) \cdot \epsilon_{93} \cdot BR_{k,93} \cdot f_k \cdot e^{-\lambda_k t} \\ \rho_{185}(t) = \sum_k A_k(t_0) \cdot \epsilon_{185} \cdot BR_{k,185} \cdot f_k \cdot e^{-\lambda_k t} \end{cases} \tag{3.3}$$

where k = ^{67}Cu, ^{67}Ga, $A_k(t_0)$ is the EoB activity to be determined, ϵ is the HPGe efficiency for the given peak energy, BR_k is the branching ratio of the k-th

radionuclide referred to the given peak, $f_k = \frac{1 - e^{-\lambda_k \cdot RT}}{\lambda_k \cdot RT}$ and $e^{-\lambda_k t}$ are correction factors for the measurement duration and the cooling time, respectively, with λ_k the decay constant of the k-th radionuclide and RT the real time of the measurement.

The solution of the linear system allows to determine the EoB activity of the two radionuclides, from which the cross sections as a function of the proton energy E can be calculated using Eq. 2.9.

The results of the nuclear cross section measurements are shown in Figure 3.19-Figure 3.24, together with TENDL predictions [5] and the experimental data available in the literature [8, 44, 49, 50, 53, 78–83].

To optimize the production of the radionuclide of interest, a study of the yield and the radionuclidic purity was carried out on the basis of the measured cross sections.

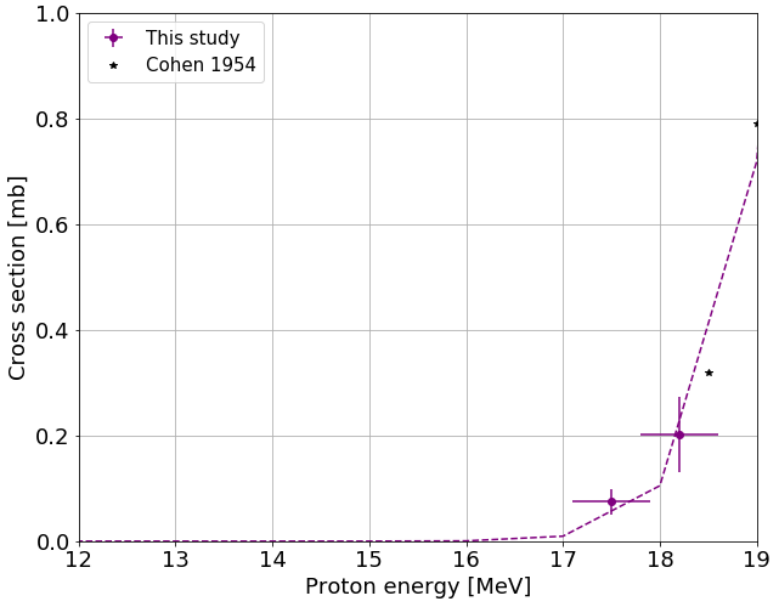

Figure 3.19: $^{64}Zn(p,\alpha n)^{60}Cu$ reaction cross section.

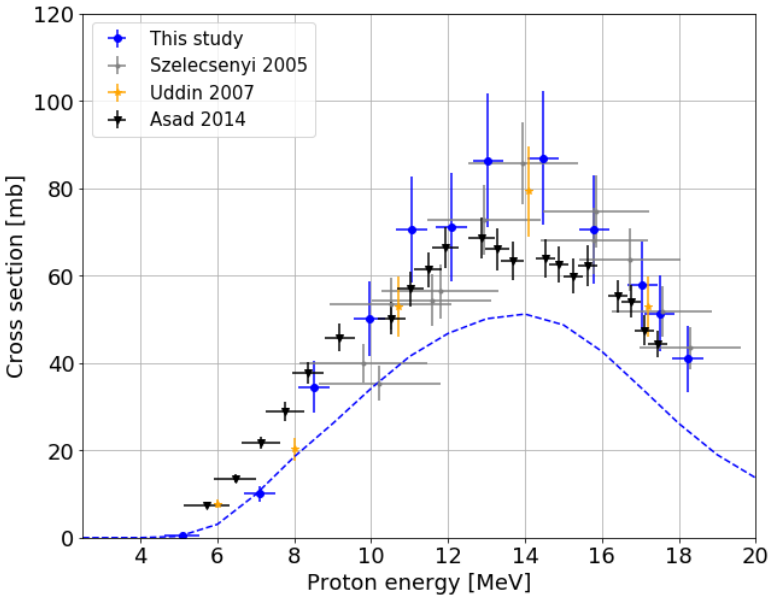

Figure 3.20: ^{64}Zn(p,α)^{61}Cu reaction cross section.

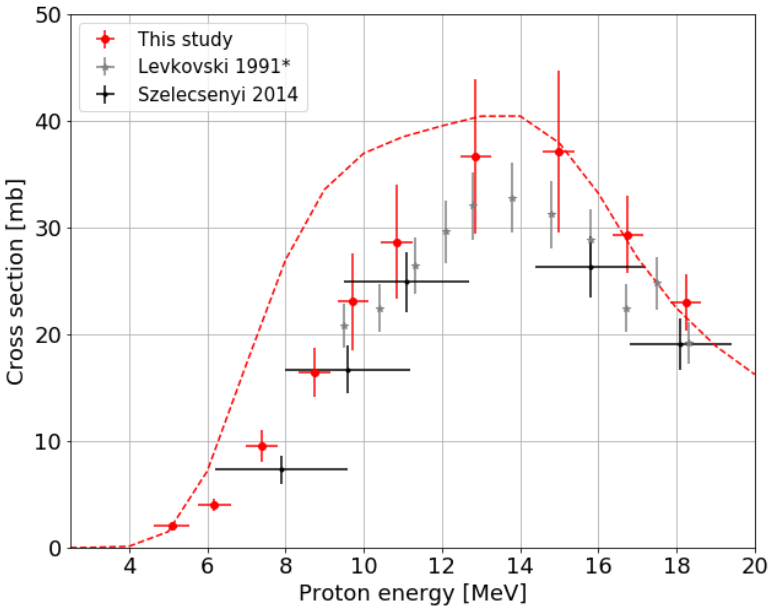

Figure 3.21: ^{67}Zn(p,α)^{64}Cu reaction cross section.

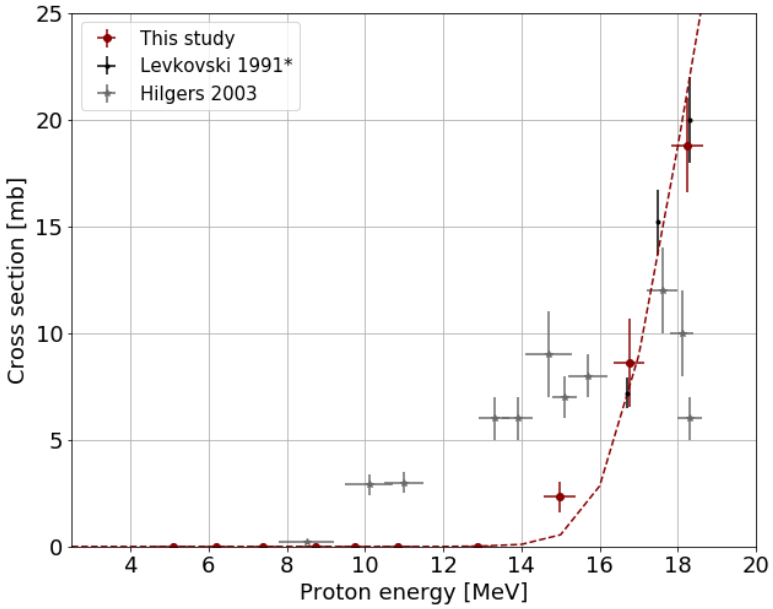

Figure 3.22: ^{68}Zn(p,αn)^{64}Cu reaction cross section.

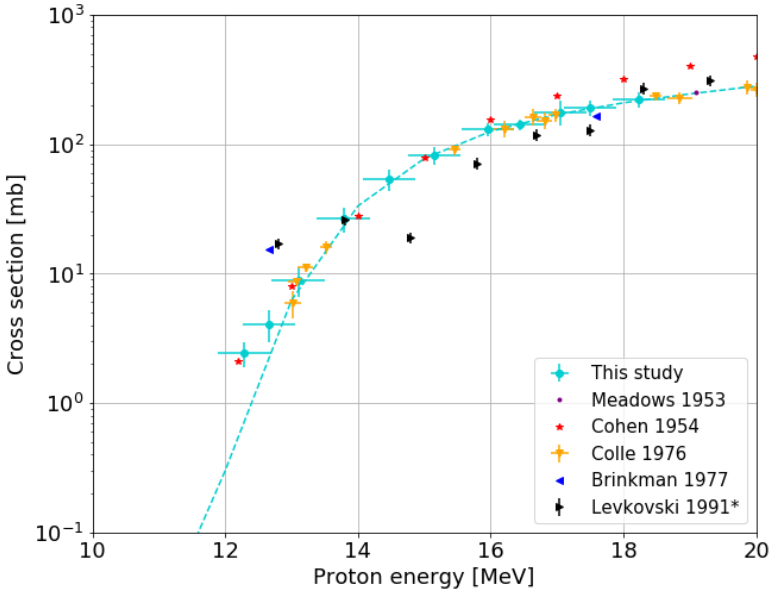

Figure 3.23: ^{65}Cu(p,pn)^{64}Cu reaction cross section.

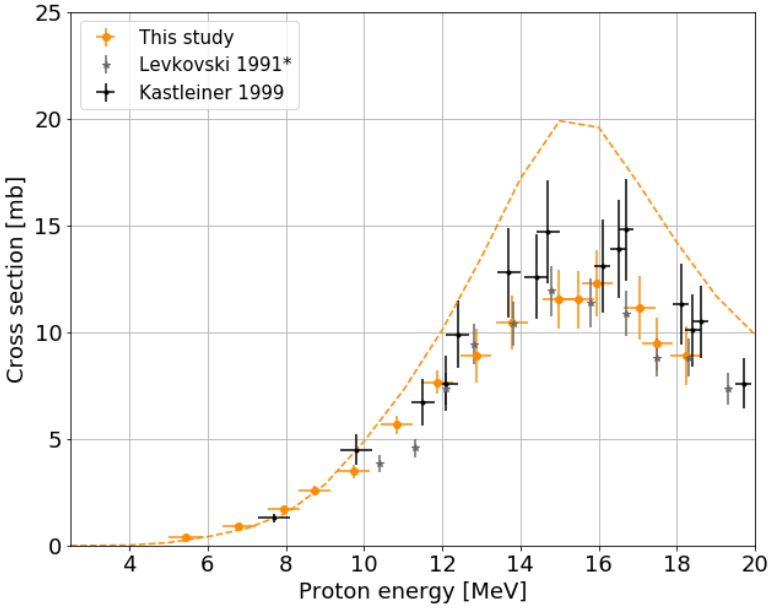

Figure 3.24: ^{70}Zn(p,α)^{67}Cu reaction cross section.

Copper-61 The TTY of the copper radioisotopes produced at saturation by irradiating a natural Zn and an enriched ^{64}Zn target and the radionuclidic purity are shown in Figure 3.25-a and Figure 3.25-b, respectively, as a function of the proton entry energy.
As the ^{64}Zn percentage in the natural material is about 49%, when using the enriched material the yield increases by just a factor 2. However, a significant difference is observed for radionuclidic purity. In the case of enriched ^{64}Zn, ^{61}Cu is the only copper radioisotope formed in the irradiation, as the production of the short-lived ^{60}Cu at high energies is negligible, and the radionuclidic purity remains constant over time. For natural Zn, on the other hand, the co-production of the relatively long-lived ^{64}Cu affects the radionuclidic purity, causing it to decrease over time and limiting the period of application of the labelled compound.

These calculations were confirmed by carrying out several production tests with the STS. Disc-shaped pellets of 6 mm diameter were prepared by compression of natural Zn and enriched ^{64}Zn powder and irradiated.

A series of irradiations at low currents were carried out to verify the correctness of the cross section measurements. A more detailed description and the results of these tests are reported in Ref. [84], of which I am the first author and which is reprinted in Part II of this thesis.

A second series of tests on enriched ^{64}Zn pellets was carried out at high currents to produce from 1 GBq to 2 GBq of ^{61}Cu. At that time, a 300 μm vacuum window in Nb was mounted in the STS, so the maximum input energy reachable was about 11.7 MeV.
The irradiation parameters and the obtained results are reported in Table 3.10. In the fourth test, at the EoB it was observed that the pellet was completely charred, as shown in Figure 3.26. This may explain the measured activity much lower than expected and highlights the need to optimize the target in view of possible routine industrial production of ^{61}Cu.

In the other cases, the produced activity was sent to DCBP for radiochemical treatments. The separation of ^{61}Cu from the zinc matrix and the other impurities was carried out by means of a two-step procedure based on the evaporation technique and extraction chromatography. A separation efficiency of about 88% was achieved and no other radionuclides were observed in the final product. ^{61}Cu was then used to label biomolecules with the DOTA chelator, resulting in a labelling yield of 97% [85]. These promising results demonstrated the feasibility of producing ^{61}Cu with a medical cyclotron.

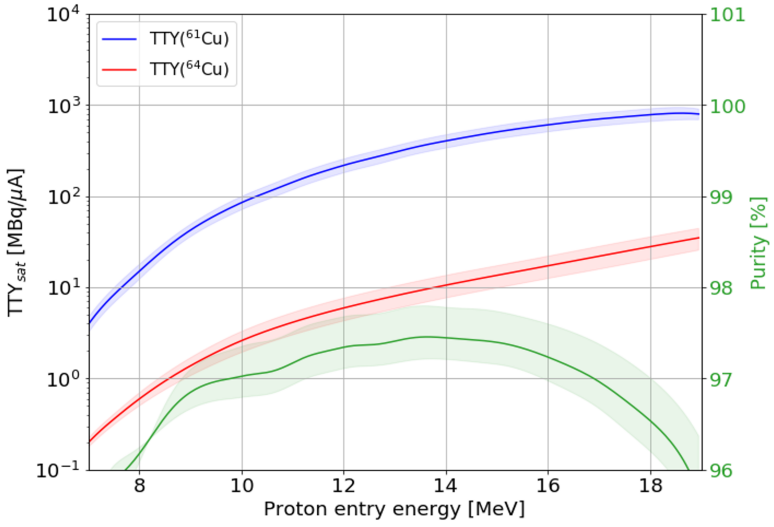

(a)

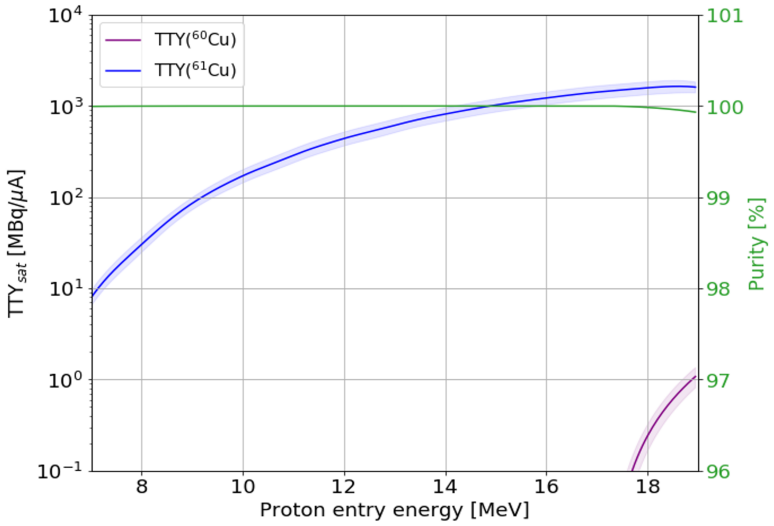

(b)

Figure 3.25: TTY of ^{61}Cu and of the related impurity for a natural Zn (a) and a 99.40% enriched ^{64}Zn (b) target. The bands correspond to the maximum and minimum yield calculated on the basis of the measured cross sections.

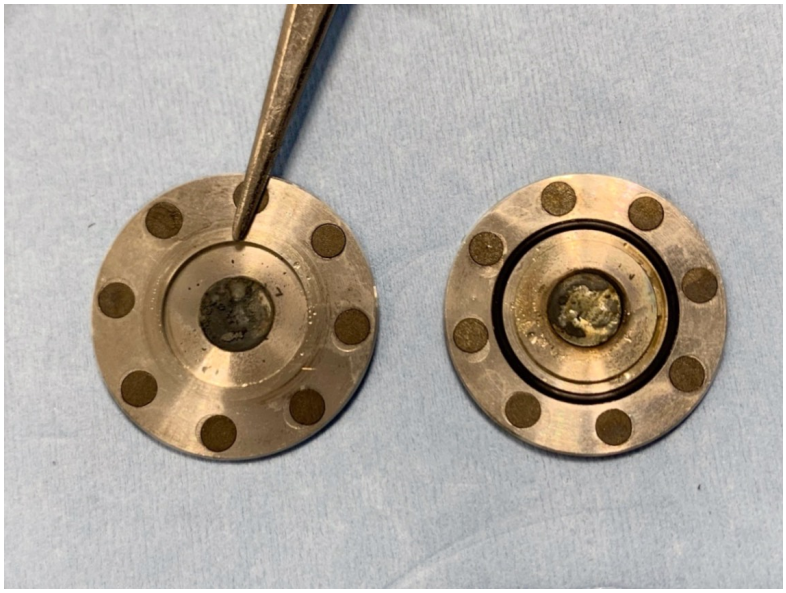

Figure 3.26: Coin target and enriched ^{64}Zn pellet after being irradiated with about 9.7 μA on pellet for almost 4.5 h (Irradiation 4 in Table 3.10).

Irradiation [#]	Δx pellet [μm]	E_{in} [MeV]	Q [μAh]	Y(^{61}Cu) [GBq/μAh]
1	345	11.6 ± 0.4	11 ± 1	0.079 ± 0.017 *(0.076)*
2	320	11.6 ± 0.4	11 ± 1	0.067 ± 0.015 *(0.076)*
3	330	11.7 ± 0.4	19 ± 2	0.064 ± 0.014 *(0.078)*
4	500	11.6 ± 0.4	42 ± 4	0.049 ± 0.011 *(0.076)*
5	490	11.7 ± 0.4	36 ± 4	0.075 ± 0.011 *(0.078)*

Table 3.10: Irradiation parameters, pellet thickness and ^{61}Cu yield obtained irradiating enriched 99.40% ^{64}Zn pellets. The values in parentheses are the yield calculations based on cross section measurements.

Copper-64 The ^{65}Cu(p,pn)^{64}Cu nuclear reaction enables the production of ^{64}Cu in carrier-added form, which results in low specific activity. The presence of non-radioactive copper in the final product leads to two major problems: overexposure of human subjects to copper that can lead to cytotoxicity, with a wide range of side effects; ^{65}Cu competes with ^{64}Cu in binding to the chelator, making it impossible to prepare receptor-specific radiopharmaceuticals. However, several studies have shown the possibility of using ^{64}Cu in the [^{64}Cu]$CuCl_2$ form for PET imaging [86–88], without any labelling procedure. In this case, ^{64}Cu in the carrier-added form can therefore be used, provided that the clinically relevant amount does not manifest any toxicity concerns due to "cold" copper.

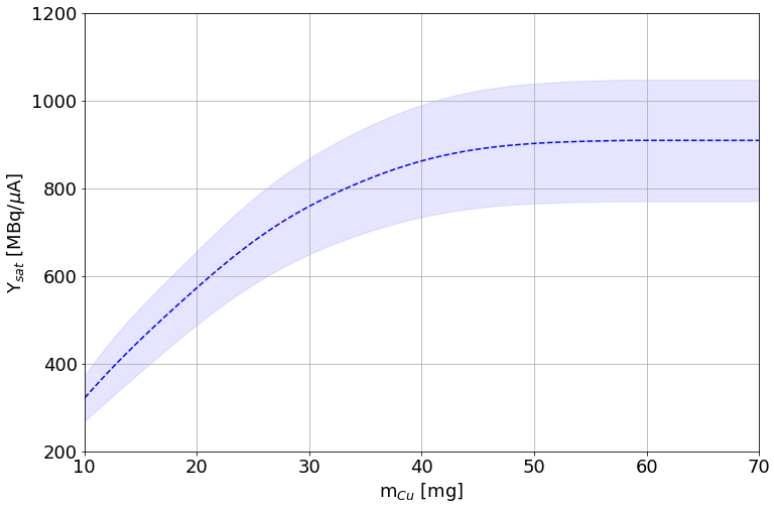

Figure 3.27: ^{64}Cu saturation yield as a function of the target copper mass, considering a 6-mm-diameter 99.67% enriched ^{65}CuO pellet. The proton entry energy is set to 17.8 MeV. The bands correspond to the maximum and minimum yield calculated on the basis of the measured cross sections.

To optimize the specific activity of ^{64}Cu, I carried out a study of the production yield under saturation condition as a function of the copper target mass, if a 6-mm-diameter pellet is used (Figure 3.27). The proton input energy is set at 17.8 MeV. According to our findings, a ^{64}Cu yield of 758 MBq/μA can be obtained by irradiating a 30-mg 99.67% enriched ^{65}Cu target. No other copper radioisotopes are produced. Considering a constant current on target of 10 μA, the average clinically relevant [^{64}Cu]$CuCl_2$ dose for PET imaging of 339 MBq [89, 90] corresponds to a copper intake of 0.02 mg Cu/kg for a 60 kg patient. This value is well below the copper overexposure limit of 5 mg Cu/kg body weight, above which toxic effects are reported in the literature [74, 91].

Since, according to TENDL [5], the ^{65}Cu(p,pn)^{64}Cu reaction cross section has a maximum at about 24 MeV, our result can be further improved by considering higher proton energies. Research or commercial cyclotrons that can provide at least 26 MeV protons can be evaluated for this purpose.

The irradiation of an enriched ^{67}Zn target allows to obtain ^{64}Cu in a no-carrier-added form; however, the eventual production of copper impurities, namely ^{61}Cu and ^{67}Cu, must be kept under control. In particular, the presence of the long-lived ^{67}Cu, which increases for longer irradiation times, could cause a decrease in the radionuclidic purity over time, limiting the application period of the ^{64}Cu-labelled radiopharmaceutical. For this reason, I considered the amount of ^{67}Cu produced irradiating a thick 89.60% enriched ^{67}ZnO target in saturation condition (Figure 3.28) and investigated its impact on the radionuclidic purity as a function of decay time (Figure 3.29). The proton energy was set to 17.8 MeV. According to our findings, a ^{64}Cu TTY of 479 MBq/μA with a purity EoB of about 96% can be achieved. The amount of ^{67}Cu produced is negligible, as its contribution remains below 0.1% for more than 50 h after the EoB.

For the impurity ^{61}Cu, a different consideration shall be made. In order to inject the patient with a radiopharmaceutical labelled exclusively with ^{64}Cu with a purity of more than 99%, it is necessary to wait at least 10 h to let ^{61}Cu decay. However, it is important to consider that ^{61}Cu is a β^+ emitter with a shorter half-life than ^{64}Cu, so it does not lead to a higher dose absorbed by the patient nor does it produce any image-degrading effects. Its presence in the sample may therefore not be a problem or even be a benefit. In fact, the difference in half-life between the two copper radioisotopes might allow the same radiopharmaceutical to be used to follow fast (^{61}Cu based) and slow (^{64}Cu based) metabolic processes. In support of this consideration, it is important to underline that radiopharmaceuticals for clinical applications containing a mixture of radioisotopes have already been approved. For example, in the case of ^{223}Ra, its therapeutic effect is based on the cascade of all the radionuclides produced in its decay [92]. It would therefore be interesting to investigate the simultaneous production of ^{64}Cu and ^{61}Cu and possible subsequent clinical applications.

For both production routes, several production tests were carried out to confirm the correctness of the predictions based on cross section measurements.

A more detailed description of the study performed on ^{64}Cu at the Bern medical cyclotron and the results of the production tests can be found in Ref. [93].
This paper, of which I am the first author, is reprinted in Part II of this thesis.

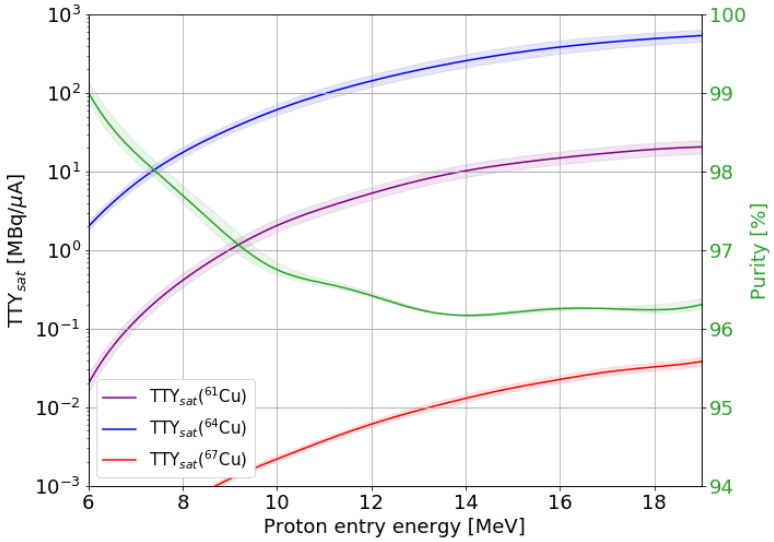

Figure 3.28: ^{64}Cu, ^{61}Cu and ^{67}Cu TTY and radionuclidic purity at saturation as a function of the proton entry energy. The bands correspond to the maximum and minimum yield calculated on the basis of the measured cross sections.

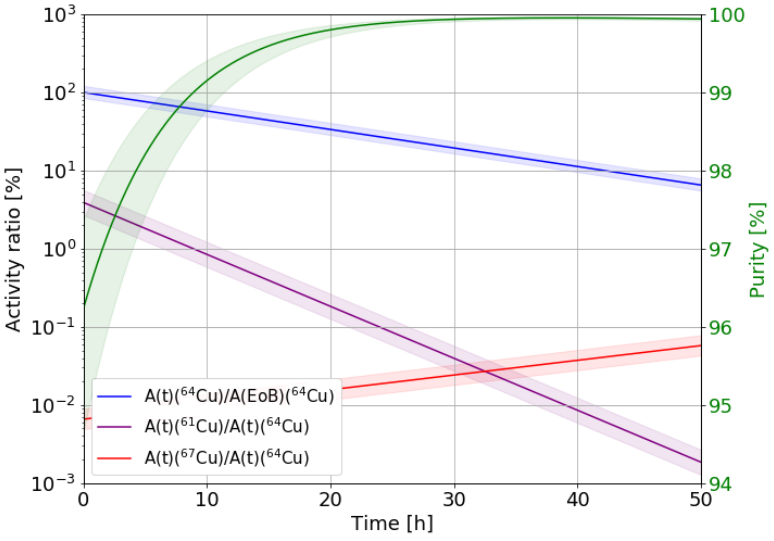

Figure 3.29: Copper radioisotopes activity ratios and radionuclidic purity as a function of time. The EoB activities are calculated at saturation for an entry energy of 17.8 MeV. The bands correspond to the maximum and minimum yield derived from the measured cross sections.

Copper-67 The yield and the radionuclidic purity of ^{67}Cu achievable irradiating an enriched ^{70}ZnO thick target depend on the energy of the proton beam entering the target, as reported in Figure 3.30-a. In particular, the threshold for the nuclear reaction ^{68}Zn(p,α)^{64}Cu lies at about 14 MeV; high-purity ^{67}Cu can therefore be obtained only at energies below this value, at the expenses of the yield. However, as ^{64}Cu has a considerably shorter half-life than ^{67}Cu, its production can be reduced by considering longer irradiation times.

According to our findings, a ^{67}Cu TTY of 154 MBq/μA with a radionuclidic purity of 99.5% can be achieved at saturation, as shown in Figure 3.30-b. The purity of the sample further increases during the time required for radiochemical processing, due to the decay of ^{64}Cu.
On the other hand, ^{64}Cu has been used in preclinical studies as a therapeutic radionuclide [87, 94] due to the emission of β^- particles, which would increase the dose absorbed by the tumour. Further studies would be required to establish the impact of ^{64}Cu from a dosimetry perspective.

These predictions based on the cross section measurements were confirmed by carrying out several production tests in the energy range (18.2-15.8) MeV, irradiating a 0.37-mm enriched ^{70}ZnO target. The irradiation parameters and the results obtained are reported in Table 3.11. The ^{67}Cu and ^{64}Cu production yields, calculated in our irradiation conditions, are reported in Figure 3.31 together with the radionuclidic purity as a function of the proton entry energy. The expected values are compared with the experimental results.

To the best of my knowledge, this was the first time that ^{64}Cu has been experimentally measured in the production route and energy range investigated, usually considered impurity-free [95].

A more detailed description of ^{67}Cu production with solid targets carried out at the Bern medical cyclotron can be found in Ref. [96], of which I am the first author and which is reprinted in Part II of this thesis.

Although the yield of ^{67}Cu achievable is rather low, modern medical cyclotrons can deliver very high beam currents (above 300 μA). This would make it possible to produce sufficient quantities of ^{67}Cu with the radionuclidic purity suitable surely for clinical trials and for therapeutic application in nuclear medicine. In this respect, the results achieved in this study confirm the predictions reported by Kastleiner et al. [53] and represent an important step forward in the use of low energy cyclotrons for the production of ^{67}Cu. However, the behaviour of the target under high-current irradiation would need to be investigated. Further studies are planned for this purpose.

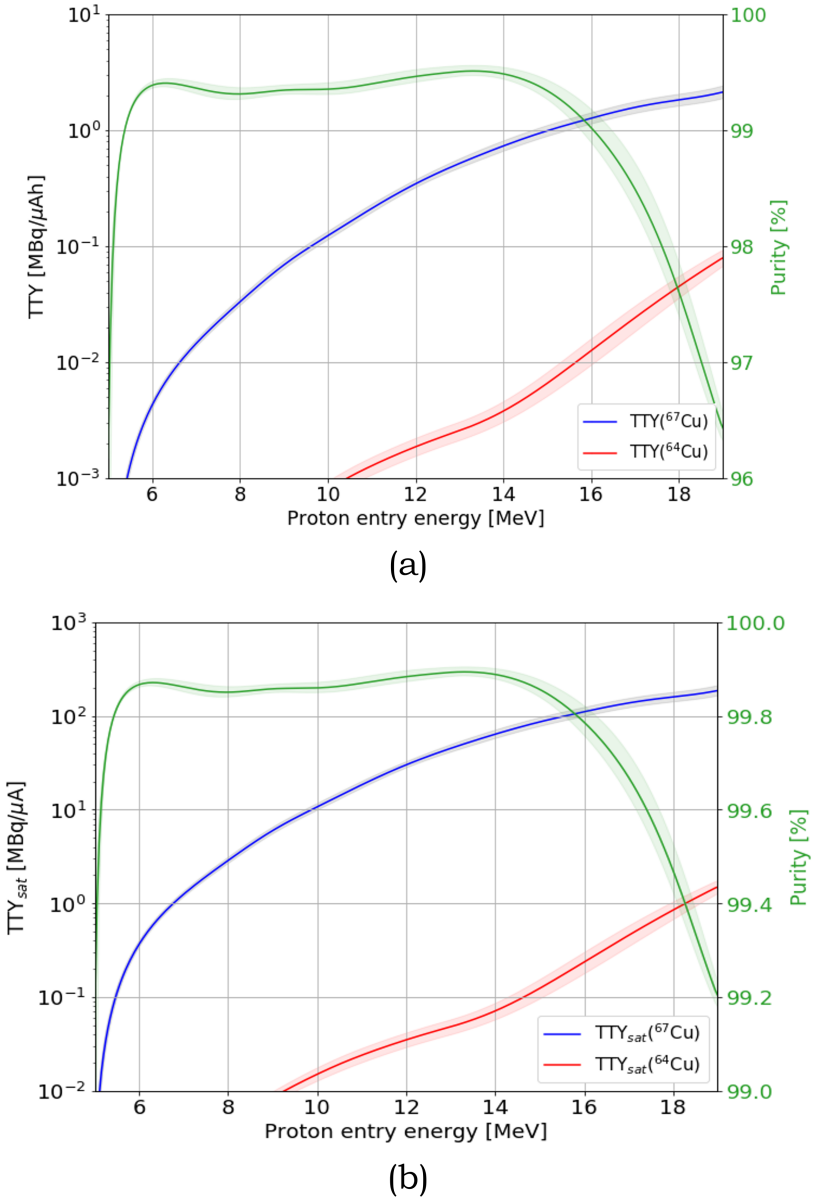

Figure 3.30: ^{67}Cu and ^{64}Cu TTY and radionuclidic purity for an irradiation time of 1 h (a) and at saturation (b) as a function of the proton entry energy. The bands correspond to the maximum and minimum yield calculated on the basis of the measured cross sections.

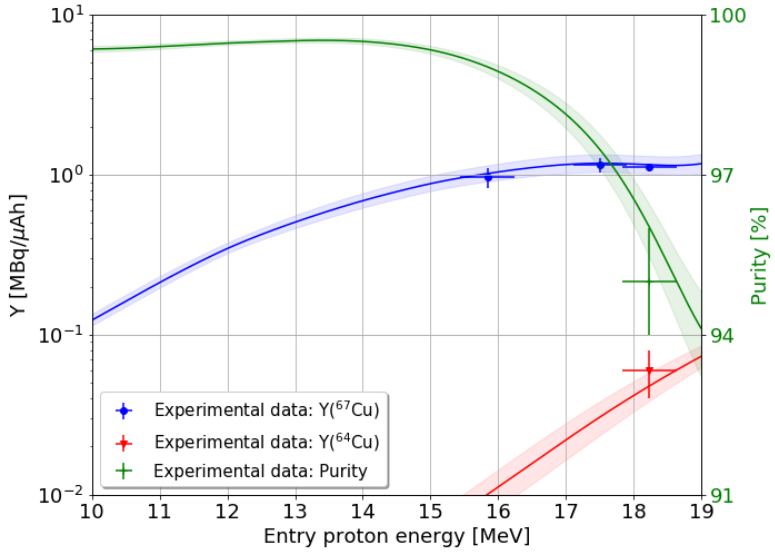

Figure 3.31: ^{67}Cu and ^{64}Cu yields and radionuclidic purity calculated in our irradiation conditions from the cross section measurements compared to the experimental results. The bands correspond to the maximum and minimum yield calculated on the basis of the measured cross sections.

Irradiation [#]	E_{in} [MeV]	Q 10^{-3} [μAh]	Y(^{67}Cu) [MBq/μAh]	Y(^{64}Cu) [MBq/μAh]	P(EoB) [%]
1	(15.8 ± 0.4)	7.9 ± 0.8	0.96 ± 0.14 *(1.02)*	No Signal *(0.01)*	~100 *(99)*
2	(17.5 ± 0.4)	1.7 ± 0.2	1.15 ± 0.12 *(1.18)*	No Signal *(0.03)*	~100 *(98)*
3	(18.2 ± 0.4)	37.7 ± 1.8	1.11 ± 0.07 *(1.15)*	0.06 ± 0.02 *(0.05)*	95 ± 1 *(96)*

Table 3.11: Irradiation parameters, ^{67}Cu and ^{64}Cu yields and radionuclidic purity at the EoB, obtained irradiating the 0.37-mm-thick 98.75% enriched ^{70}ZnO pellet. The values in parentheses are the yield calculations based on the cross section measurements.

3.3 Gallium-68

^{68}Ga [$t_{1/2}$ = 67.71 min, $\bar{E}_{\beta^+}$ = 836 keV (87.7%), E_γ = 1077 keV (3.2%)] is a β^+ emitter widely used in nuclear medicine for PET imaging. Together with the therapeutic β^- emitters ^{177}Lu and ^{90}Y, ^{68}Ga forms a theranostic pair used to label PSMA ligands (e.g. PSMA-11) or somatostatin analogues (eg. DOTATOC, DOTATATE), for the diagnosis and treatment of prostate cancer and NeuroEndocrine Tumours (NET), respectively.

Currently, ^{68}Ga is mainly obtained via ^{68}Ge/^{68}Ga generators. However, their scarce availability, high price and limited produced radioactivity per elution are a major barrier for a wider use of ^{68}Ga-based diagnostic radiotracers. To cope with growing demand, production with biomedical cyclotrons could be a valid solution [97].

I investigated the ^{68}Zn(p,n)^{68}Ga nuclear reaction by irradiating enriched ^{68}Zn targets. This production route was already reported in the literature using either liquid [98, 99] or solid targets [100, 101]. Despite the clear advantages of using liquid targets, such as saving time for target preparation and post-irradiation dissolution, the production yield is significantly lower than with solid targets. In both cases, gallium impurities are co-produced during the irradiation and must be kept under control, namely ^{67}Ga, obtained from the ^{68}Zn(p,2n)^{67}Ga and ^{67}Zn(p,n)^{67}Ga reactions, and ^{66}Ga, obtained via the ^{67}Zn(p,2n)^{66}Ga and ^{66}Zn(p,n)^{66}Ga reactions.

The main characteristics of gallium radioisotopes are reported in Table 3.12.

Radioisotope	$t_{1/2}$	Decay mode: [%]	E_γ [keV]	BR [%]
^{68}Ga	67.71*(8)* min	ec + β^+: 100	1077.34*(5)*	3.22*(3)*
^{67}Ga	3.2617*(5)* d	ec: 100	93.310*(5)*	38.81*(3)*
^{66}Ga	9.49*(3)* h	ec + β^+: 100	1039.220*(3)*	37.0*(20)*

Table 3.12: Decay properties and main γ emissions of gallium radioisotopes. The values in parentheses are the uncertainties referred to the last digits of the value.

To maximize ^{68}Ga production yield and radionuclidic purity, I measured the cross sections of the nuclear reactions involved as a function of the proton energy by irradiating natural Zn and enriched ^{68}Zn samples. In the case of the enriched material, the cross sections were measured by irradiating few μm-thick enriched ^{68}Zn solid discs (marked as A in Table 3.13), so that the samples could be removed from the target holder during measurements with the HPGe. In fact, the aluminum disc described in Section 2.2 contains traces of natural zinc, that

	^{64}Zn	^{66}Zn	^{67}Zn	^{68}Zn	^{70}Zn
Natural Zn [%]	49.17	27.73	4.04	18.45	0.61
Enr. ^{68}Zn (A) [%]	0.99	0.81	0.38	97.80	0.02
Enr. ^{68}Zn (B) [%]	0.01	0.10	0.61	99.26	0.02

Table 3.13: Isotopic fractions of the natural Zn powder purchased by GoodFellow [35], the enriched ^{68}Zn foil by TRACE Sciences International [76] (A) and the enriched ^{68}Zn powder by Isoflex [36] (B).

would lead to a systematic error in cross section measurements, in particular for the reactions starting from isotopes with a low percentage in the enriched material (e.g. ^{66}Zn(p,n)^{66}Ga).

The contributions of the two nuclear cross sections involved in the production of ^{66}Ga and ^{67}Ga were disentangled using the method that I developed, as described in Section 2.2.

The results of the nuclear cross section measurements are reported in Figure 3.32 - Figure 3.36, together with TENDL predictions [5] and the experimental data available in the literature [8, 102, 103].

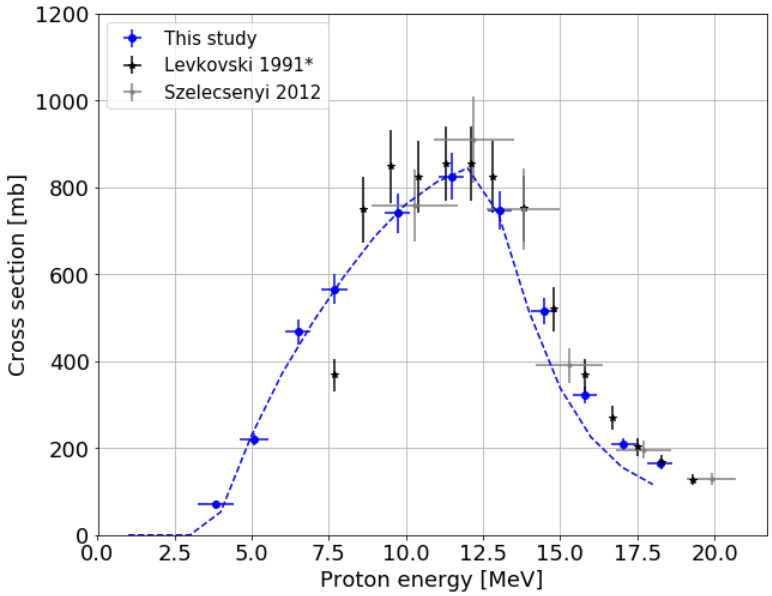

Figure 3.32: ^{68}Zn(p,n)^{68}Ga reaction cross section.

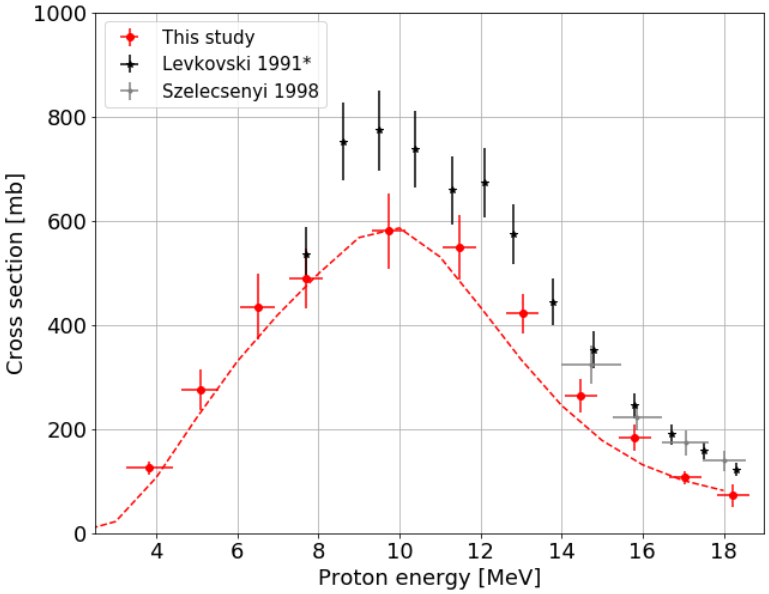

Figure 3.33: ^{67}Zn(p,n)^{67}Ga reaction cross section.

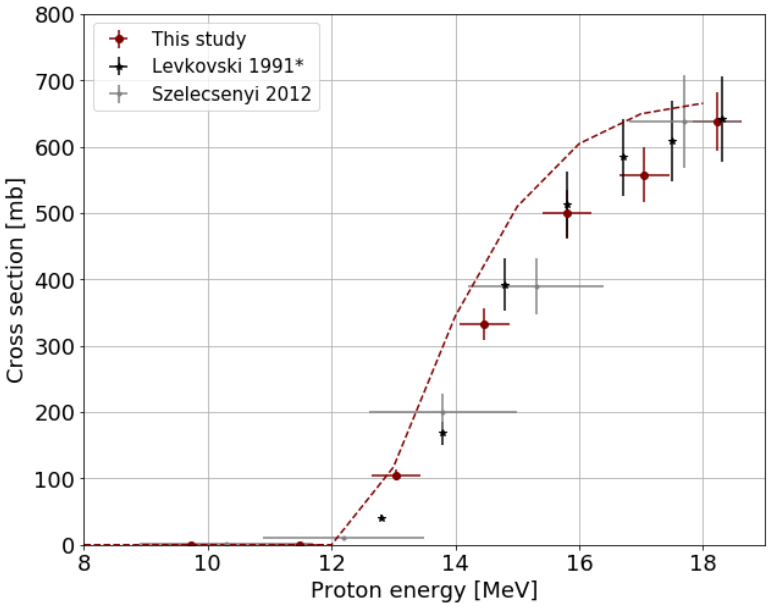

Figure 3.34: ^{68}Zn(p,2n)^{67}Ga reaction cross section.

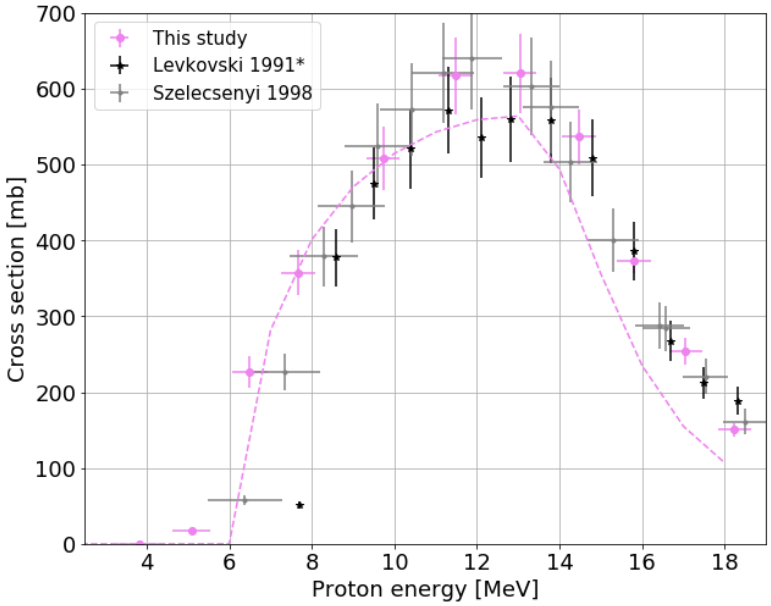

Figure 3.35: ^{66}Zn(p,n)^{66}Ga reaction cross section.

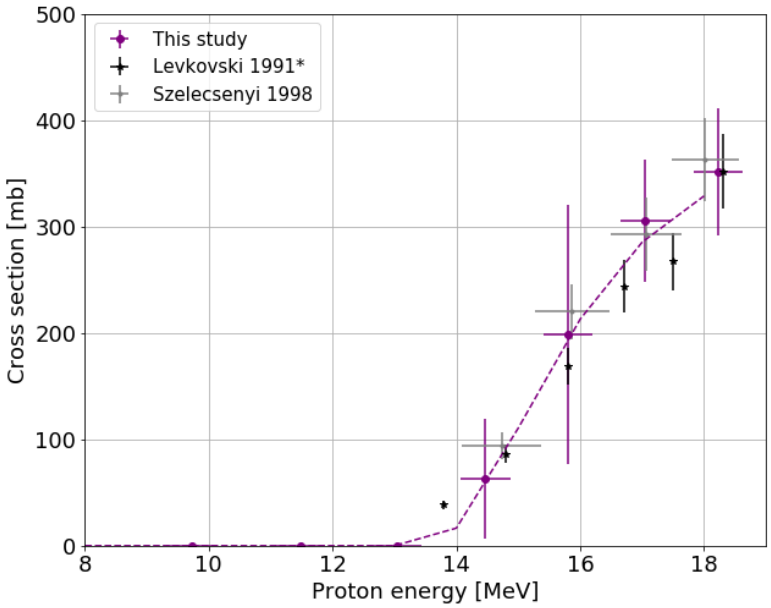

Figure 3.36: ^{67}Zn(p,2n)^{66}Ga reaction cross section.

A study of the TTY was carried out on the basis of the results obtained. Knowing the reaction cross sections, it is possible to calculate the yield for any enriched material. The thick target production yields of ^{68}Ga, ^{67}Ga and ^{66}Ga are reported in Figure 3.37 as a function of proton input energy for the 99.26% enriched ^{68}Zn material (marked as (B) in Table 3.13), used in the production tests.

According to the European Pharmacopoeia requirements, the purity of ^{68}Ga must be above 98% at the time of injection in order to be used in clinical applications [104]. For this to be possible, it is necessary to optimize the radionuclidic purity by setting the beam input energy below 12 MeV, which corresponds to the energy threshold of the ^{68}Zn(p,2n)^{67}Ga reaction.

Assuming an optimal input energy of 11.5 MeV, the radionuclidic purity and the remaining fraction of ^{68}Ga activity can be calculated as a function of time, as shown in Figure 3.38. The ^{68}Ga purity remains above 98% up to more than eight hours after the EoB. The synthesis of the radiopharmaceutical and its subsequent injection into the patient must take place within this time to fulfil the requirements of the European Pharmacopoeia.

To confirm the results on cross section measurements, several production tests were carried out with the STS in the energy range (13-9) MeV by irradiating a 0.5-mm-thick enriched ^{68}Zn pellet. The irradiation parameters and the results obtained are reported in Table 3.14. The ^{68}Ga radionuclidic purity and production yield, calculated in our irradiation conditions, are shown in Figure 3.39 as a function of the proton entry energy and compared with the experimental results.

A more detailed description of the study on ^{68}Ga production with solid targets carried out at the Bern medical cyclotron can be found in Ref.[105], which I co-authored and which is reprinted in Part II of this thesis.

The production of ~13 GBq in about 45 minutes is a promising result in view of the use of medical cyclotrons with solid targets for a wider distribution of ^{68}Ga.

The possibility of producing such high activity would allow smaller hospitals, which have a nuclear medicine department but cannot afford a ^{68}Ge/^{68}Ga generator, to be supplied with unprocessed ^{68}Ga from which they could prepare the radiopharmaceutical doses required for internal patient needs. For this to be possible, the ^{68}Ga produced by proton irradiation of enriched ^{68}Zn solid targets must be in the same chemical form as that produced by generator.
In this regard, a study of the radiochemical dissolution and separation processes of ^{68}Ga produced by cyclotron is currently underway in collaboration with PSI and the results will be published in a forthcoming paper, in which I will be one of the co-authors.

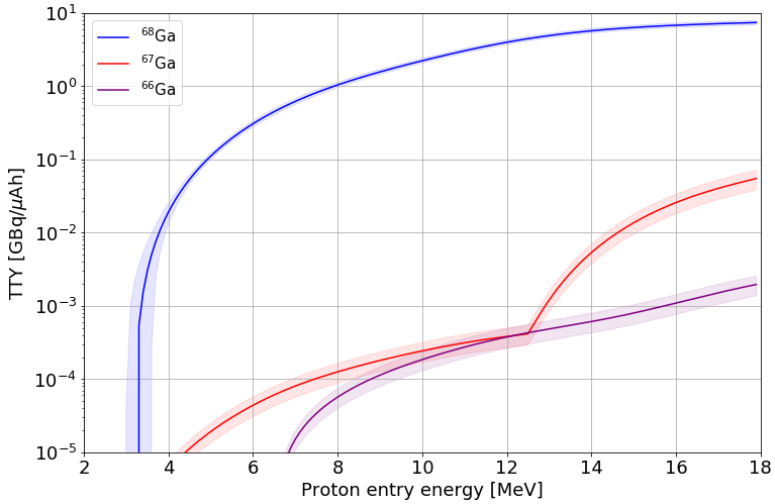

Figure 3.37: ^{68}Ga, ^{67}Ga and ^{66}Ga thick target yields for a 99.26% enriched ^{68}Zn target. The bands correspond to the maximum and minimum yield calculated on the basis of the measured cross sections.

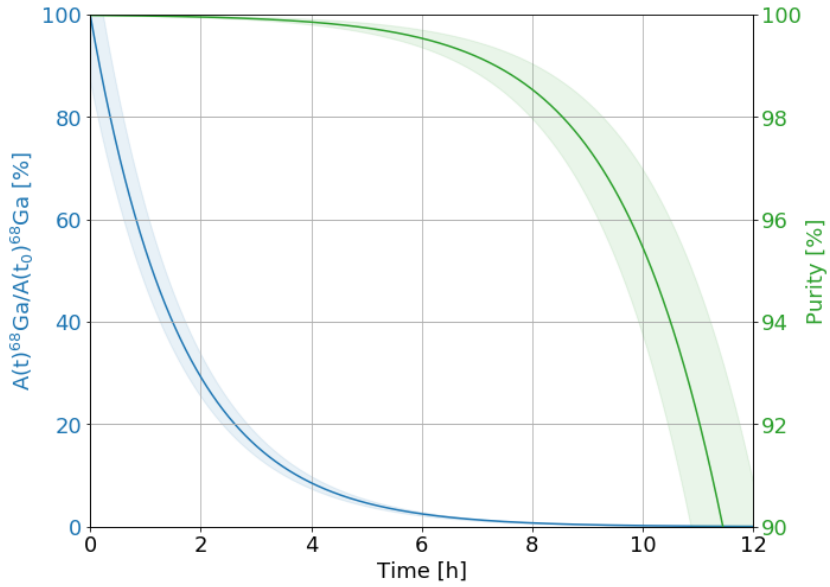

Figure 3.38: ^{68}Ga activity fraction and purity as a function of time, considering a 99.26% enriched ^{68}Zn thick target and an entry energy of 11.5 MeV. The bands correspond to the maximum and minimum yield calculated on the basis of the measured cross sections.

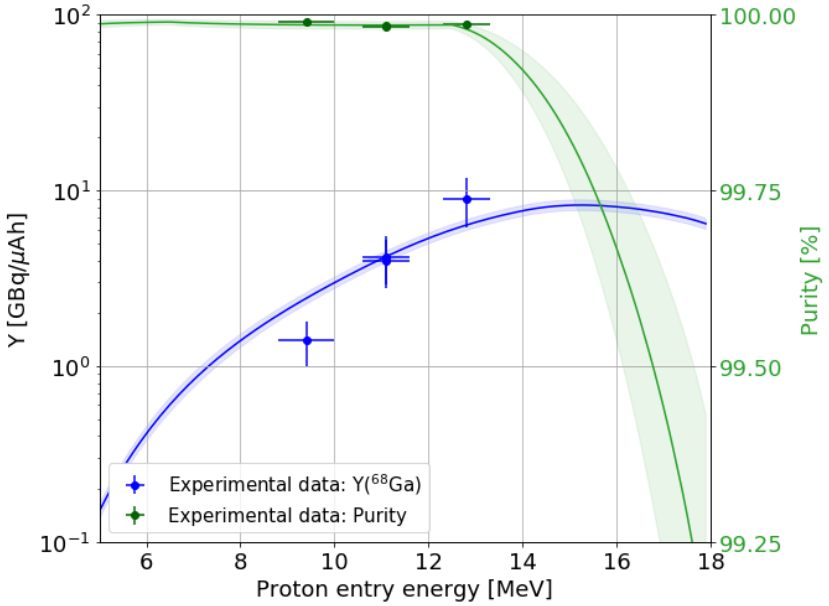

Figure 3.39: ^{68}Ga production yield and purity calculated in our irradiation conditions and the experimental results obtained with the 0.5-mm-thick 99.26% enriched ^{68}Zn pellet. The bands correspond to the maximum and minimum yield calculated on the basis of the measured cross sections.

Irradiation [#]	E_{in} [MeV]	Q [μAh]	Y(^{68}Ga) [GBq/μAh]	P(EoB) [%]
1	9.4 ± 0.6	(0.87 ± 0.26)·10^{-3}	1.4 ± 0.4 *(2.4)*	99.9891 ± 0.0004 *(99.9856)*
2	11.1 ± 0.5	0.56 ± 0.17	4.0 ± 1.2 *(4.7)*	99.9848 ± 0.0010 *(99.9854)*
3	11.1 ± 0.5	3.07 ± 0.92	4.2 ± 1.3 *(4.7)*	99.9834 ± 0.0014 *(99.9854)*
4	12.8 ± 0.5	0.12 ± 0.03	9.0 ± 2.7 *(6.3)*	99.9864 ± 0.0010 *(99.9798)*

Table 3.14: Irradiation parameters, ^{68}Ga yield and purity at the EoB obtained irradiating the 0.5-mm-thick 99.26% enriched ^{68}Zn pellet. The values in parentheses are the yield calculations based on the cross section measurements.

3.4 Technetium-99m

As briefly introduced in Chapter 1, ^{99m}Tc [$t_{1/2}$ = 6.0072 h, IT: 99.9963%, E_γ = 141 keV (89%)] is today the most widely used radionuclide for SPECT imaging examinations. Its relatively short half-life, the high emission of γ-rays of 141 keV and the absence of primary particle radiation make it the ideal diagnostic agent, minimizing the dose absorbed by the patient [106].

Currently, ^{99m}Tc is mainly extracted from generators containing ^{99}Mo [$t_{1/2}$ = 65.924 h, β^-: 100%], which is produced by the fission of ^{235}U targets in nuclear reactors. However, the gradual ageing of nuclear plants for ^{99}Mo production and the resulting frequent shutdowns for long maintenance periods might lead to significant global shortages of ^{99m}Tc, underlining the necessity to find alternative production methods [107]. Among the several proposed accelerator-based routes, one of the most promising is the direct production from enriched ^{100}Mo targets with low-energy cyclotrons [108–110].

As part of a collaboration with the University of Kyiv, Ukraine, aimed at the optimized production of ^{99m}Tc with medical cyclotrons [111], I measured the ^{100}Mo(p,2n)^{99m}Tc reaction cross section by irradiating solid enriched ^{100}Mo targets. The isotopic composition of the target material is reported in Table 3.15. Although the cross section of this reaction is widely reported in the literature [8, 112–124], a considerable spread in the results required further experimental investigations.

	^{92}Mo	^{94}Mo	^{95}Mo	^{96}Mo	^{97}Mo	^{98}Mo	^{100}Mo
Natural Mo [%]	14.649	9.187	15.873	16.673	9.582	24.292	9.744
Enr. ^{100}Mo [%]	0.88	0.57	1.11	1.28	0.8	3.16	92.2

Table 3.15: Isotopic fractions of the natural Mo foil purchased by GoodFellow [35] and the enriched ^{100}Mo powder provided by the University of Kyiv.

Despite the use of highly enriched target material, several Tc radioisotopes are produced during the irradiation (Table 3.16). A precise knowledge of the cross sections of the nuclear reactions involved is therefore of paramount importance for optimizing the radionuclidic purity.

In almost all cases, two nuclear isomers are populated. If the metastable state decays by IT into the ground state, it causes an increase in its activity and complicates the cross section measurement.

Moreover, all Tc impurities, except for ^{93}Tc and ^{93m}Tc, in the energy range of interest are produced by two nuclear reactions. To determine each contribution

Radioisotope	$t_{1/2}$	Decay mode: [%]	E_γ [keV]	BR [%]
^{93}Tc	2.75*(5)* h	ec + β^+: 100	1362.94*(7)*	66.2*(6)*
^{93m}Tc	43.5*(10)* min	IT: 77.4	391.83*(8)*	58.3*(9)*
		ec + β^+: 22.6	943.7*(5)*	2.92*(24)*
^{94}Tc	293*(1)* min	ec + β^+: 100	702.67*(7)*	99.6*(18)*
^{94m}Tc	52.0*(10)* min	ec + β^+: 100	1522.1*(2)*	4.5*(3)*
^{95}Tc	20.0*(1)* h	ec + β^+: 100	765.789*(9)*	93.8*(3)*
^{95m}Tc	61*(2)* d	ec + β^+: 96.12	204.117*(2)*	63.2*(8)*
		IT: 3.88	38.9*(1)*	7.5E-5*(6)*
^{96}Tc	4.28*(7)* d	ec + β^+: 100	812.54*(4)*	82*(3)*
^{96m}Tc	51.5*(10)* min	IT: 98.0	34.20*(5)*	0.0259*(4)*
		ec + β^+: 2.0	778.22*(4)*	1.9*(5)*
^{97}Tc	4.21E+6*(16)* y	ec: 100	-	-
^{97m}Tc	91.0*(6)* d	IT: 96.06	96.5*(1)*	0.321*(3)*
		ec + β^+: 3.94	-	-
^{99}Tc	2.111E+5*(12)* y	β^-: 100	89.5*(2)*	0.00065*(15)*
^{99m}Tc	6.0072*(9)* h	IT: 99.9963	140.511*(1)*	89*(4)*
		β^-: 0.0037	89.6*(3)*	0.00104*(19)*
^{99}Mo	65.924*(6)* h	β^-: 100	739.500*(17)*	12.2*(2)*

Table 3.16: Decay properties and main γ emissions of technetium radioisotopes and ^{99}Mo. The values in parentheses are the uncertainties referred to the last digits of the value.

using the method described in Section 2.2, I measured the cross sections from natural Mo targets (isotopic composition reported in Table 3.15).
For these radioisotopes, data analysis is still ongoing and the results will be presented in a forthcoming paper, of which I will be one of the authors. The preliminary results are presented in this section.

In the case of ^{99m}Tc, it is obtained directly via the ^{100}Mo(p,2n)^{99m}Tc reaction and indirectly via the ^{100}Mo(p,pn)^{99}Mo$\rightarrow^{99m}$Tc reaction, which occurs both during the irradiation and after the EoB during the cooling and measuring time.

To determine the direct production cross section, I considered short irradiation and cooling times. Specifically, the samples were irradiated for less than 10 min and measured within 15 min after the EoB. In addition, I repeatedly measured the samples and analyzed the total activity of ^{99m}Tc over time to verify that it respected the exponential decay (Figure 3.40).

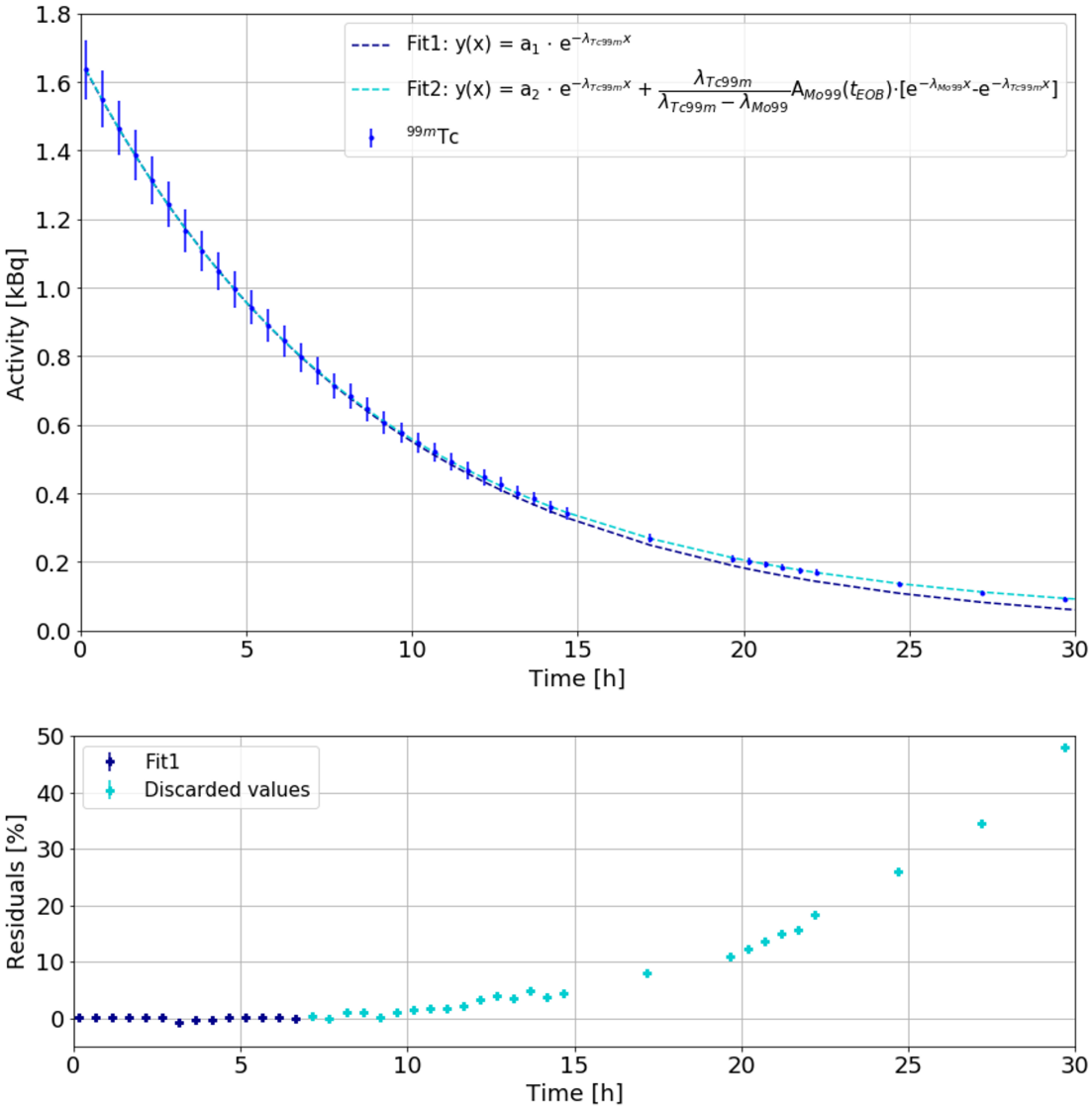

Figure 3.40: Activity of ^{99m}Tc measured over time and fit curves with the corresponding residuals.

For this purpose, I fitted the experimental data with both the exponential decay equation

$$A_{Tc99m}(t) = A_{Tc99m}(t_0)e^{-\lambda_{Tc99m}t} \tag{3.4}$$

and the Bateman equation

$$A_{Tc99m}(t) = A_{Tc99m}(t_0)e^{-\lambda_{Tc99m}t} + \frac{\lambda_{Tc99m}}{\lambda_{Tc99m} - \lambda_{Mo99}} A_{Mo99}(t_0)(e^{-\lambda_{Mo99}} - e^{-\lambda_{Tc99m}}) \tag{3.5}$$

For all samples, I observed that the exponential trend was respected for about 7 h after the EoB.

From the EoB activities provided by the exponential fit, the cross sections were calculated by using Eq. 2.9.

In the energy range of interest, ^{93}Tc and ^{93m}Tc are produced by the reaction (p,2n) from ^{94}Mo. In this case, as the metastable state has a shorter half-life, its contribution to the activity of ^{93}Tc had to be taken into account in the cross section measurements.

To determine the EoB activity of ^{93m}Tc, I fitted the activities measured over time with the exponential decay equation:

$$A_{93m}(t) = A_{93m}(t_0)e^{-\lambda_{93m}t} \tag{3.6}$$

The obtained value was used as a constant parameter in the Bateman equation

$$A_{93}(t) = A_{93}(t_0)e^{-\lambda_{93}t} + \frac{\lambda_{93}}{\lambda_{93} - \lambda_{93m}} A_{93m}(t_0)(e^{-\lambda_{93m}t} - e^{-\lambda_{93}t}) \tag{3.7}$$

to determine the EoB activity of ^{93}Tc.
The experimental data and fit curves are presented in Figure 3.40 with their corresponding residuals.

The measured cross sections are shown in Figure 3.42-Figure 3.45 together with TENDL predictions [5] and the experimental values available in the literature [8, 112–114, 119–124]. For completeness, the measured cross section data are reported in the Appendix.

The study of the Tc radioisotope yields and of the radionuclidic purity as a function of irradiation parameters is foreseen to optimize the production of ^{99m}Tc with medical cyclotrons.

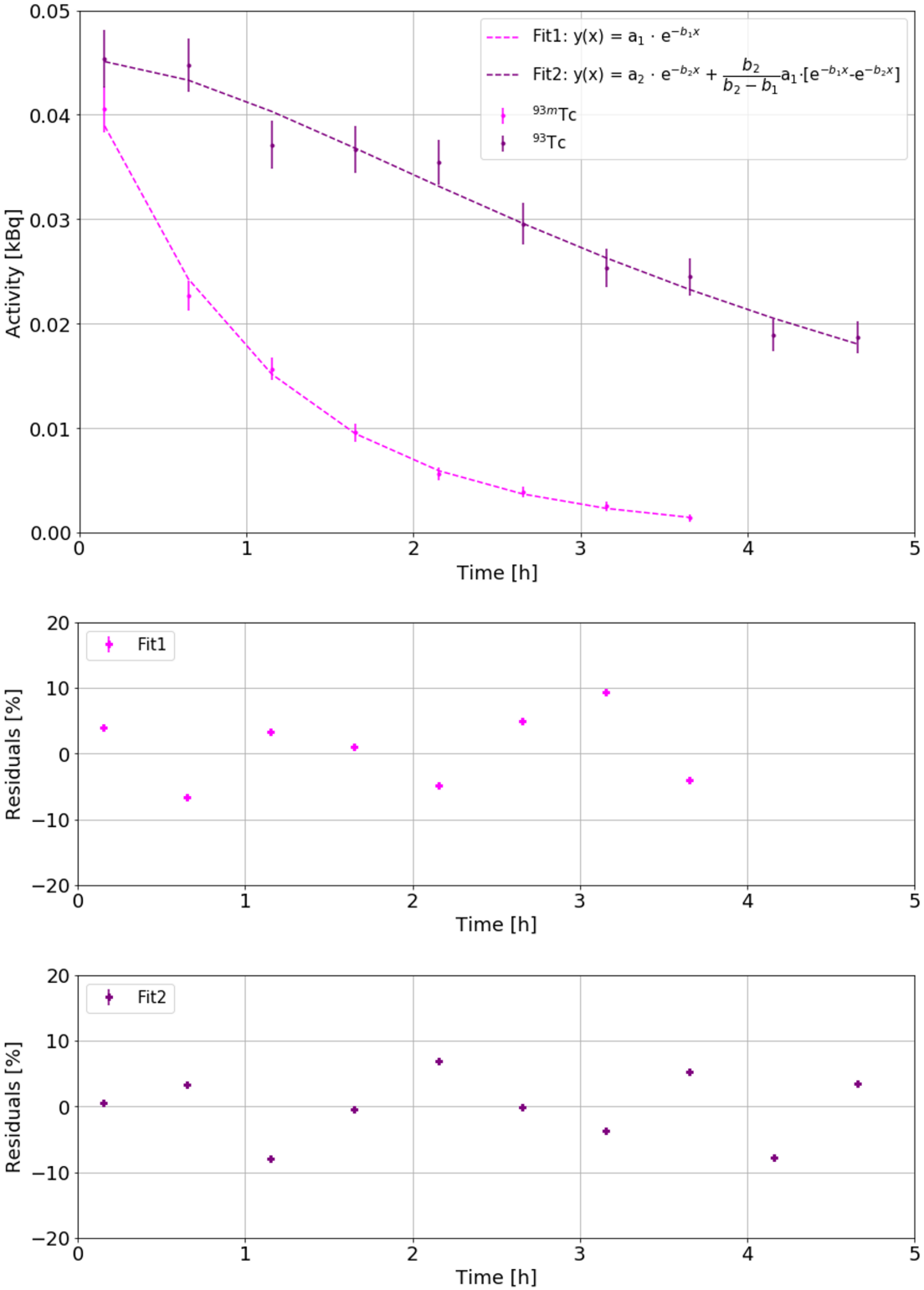

Figure 3.41: Activity of ^{93}Tc and ^{93m}Tc measured over time and fit curves with the corresponding residuals.

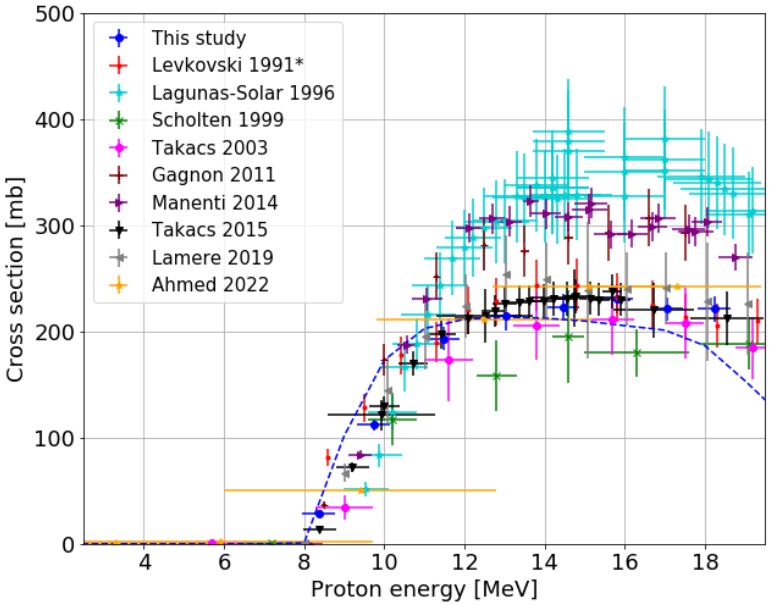

Figure 3.42: ^{100}Mo(p,2n)^{99m}Tc reaction cross section.

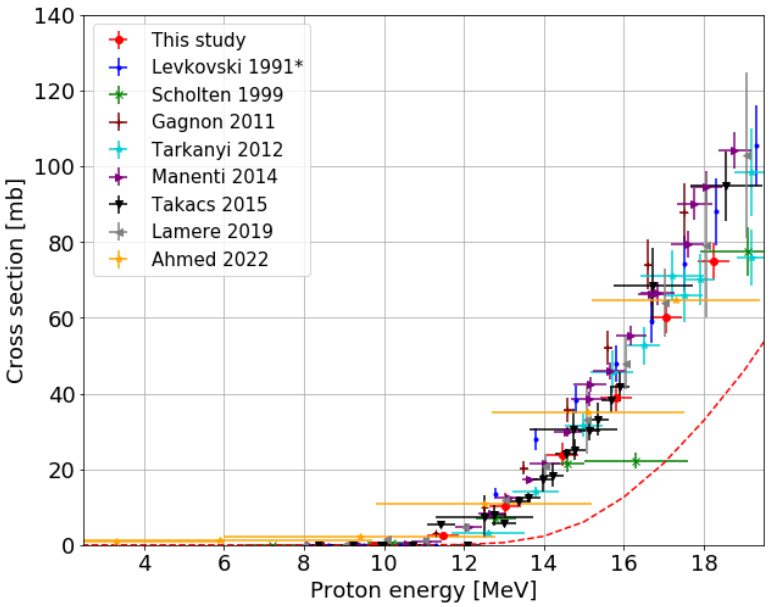

Figure 3.43: ^{100}Mo(p,x)^{99}Mo reaction cross section.

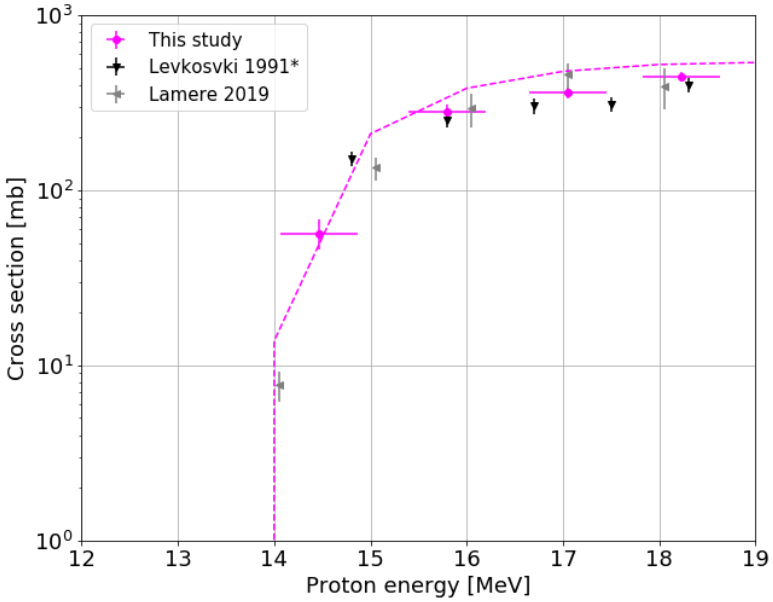

Figure 3.44: ^{94}Mo(p,2n)^{93}Tc reaction cross section.

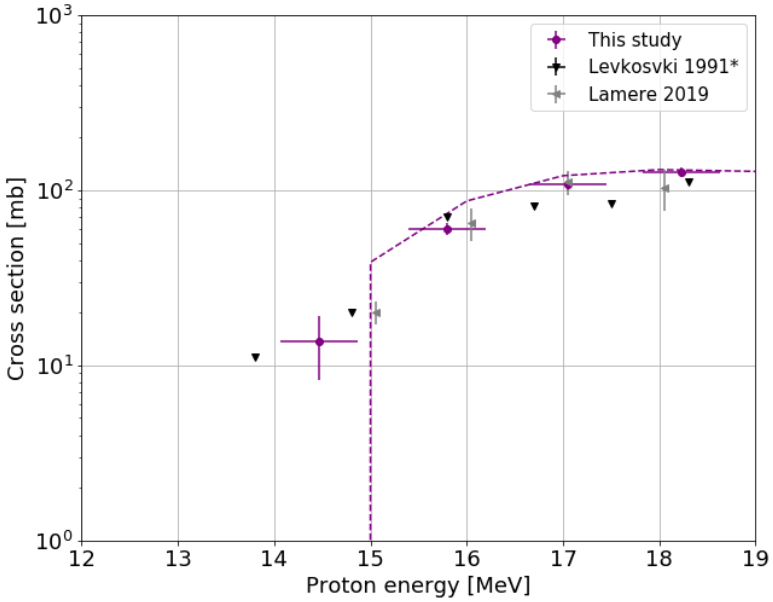

Figure 3.45: ^{94}Mo(p,2n)^{93m}Tc reaction cross section.

3.5 Terbium-155

^{155}Tb [$t_{1/2}$=5.32 d, ec: 100%, E_γ=87 keV (32.0%); 105 keV (25.1%)] is the most promising radiolanthanide for SPECT imaging, as it emits γ-rays with ideal energies for most SPECT cameras with negligible high-energy γ-rays and without β particle emissions. Since its chemical characteristics are very similar to the clinically-established ^{177}Lu and ^{90}Y, ^{155}Tb would be suitable for the study of pre-therapeutic dosimetry [125] and, due to its relatively long half-life, enable the successful following of slow metabolic processes [126]. Finally, ^{155}Tb could be used as a precise diagnostic partner for the α emitter ^{149}Tb and the β^- emitter ^{161}Tb, which are receiving increasing interest for radionuclide therapy.

The production of ^{155}Tb in quantity and quality suitable for medical applications is currently widely studied and several routes are reported in the literature. Most notably, about 200 MBq of ^{155}Tb were produced at ISOLDE (CERN) by proton-induced spallation on tantalum targets, followed by online mass separation [127]. The production of ^{155}Tb was also investigated at ARRONAX in Nantes, France, using 35 MeV deuteron beams [128].

I investigated the ^{155}Tb production with a medical cyclotron, already proposed by Dmitriev et al. in Ref. [129], by irradiating solid gadolinium oxide targets.

Natural Gd_2O_3, enriched $^{155}Gd_2O_3$ and enriched $^{156}Gd_2O_3$ targets (Table 3.17) were used to study the ^{155}Gd(p,n)^{155}Tb and ^{156}Gd(p,2n)^{155}Tb nuclear reactions. Despite the use of highly enriched targets, several terbium impurities are produced during the irradiation (Table 3.18), requiring precise cross section measurements in order to optimize the radionuclidic purity of ^{155}Tb. Some of these cross sections had no previous measurements in the literature.

Particular attention should be paid to ^{154}Tb and ^{156}Tb, for which I developed a special data analysis procedure due to the production of different nuclear isomers.

	^{152}Gd	^{154}Gd	^{155}Gd	^{156}Gd	^{157}Gd	^{158}Gd	^{160}Gd
Natural Gd_2O_3 [%]	0.20	2.18	14.80	20.47	15.65	24.84	21.86
Enr. $^{155}Gd_2O_3$ [%]	<0.02	0.5	91.90	5.87	0.81	0.65	0.27
Enr. $^{156}Gd_2O_3$ [%]	<0.01	0.05	0.87	93.30	4.38	1.08	0.32

Table 3.17: Isotopic fractions of the natural Gd_2O_3 powder purchased by GoodFellow [35], the enriched Gd_2O_3 powders by Isoflex [36].

Radioisotope	$t_{1/2}$	Decay mode: [%]	E_γ [keV]	BR [%]
^{153}Tb	2.34*(1)* d	ec + β^+: 100	212.00*(2)*	28.5*(19)*
^{154}Tb	21.5*(4)* h	ec + β^+: 100	1291.31*(13)*	6.9*(5)*
^{154m1}Tb	9.4*(4)* h	ec + β^+: 78.2	540.18*(6)*	20*(3)*
		IT: 21.8	-	-
^{154m2}Tb	22.7*(5)* h	ec + β^+: 98.2	426.78*(7)*	17.3*(12)*
		IT: 1.8	-	-
^{155}Tb	5.32*(6)* d	ec: 100	105.318*(3)*	25.1*(13)*
^{156}Tb	5.35*(10)* d	ec + β^+: 100	534.29*(6)*	67*(6)*
^{156m1}Tb	24.4*(10)* h	IT: 100	-	-
^{156m2}Tb	5.3*(2)* h	IT: 100	-	-

Table 3.18: Decay properties and main γ emissions of terbium radioisotopes. The values in parentheses are the uncertainties referred to the last digits of the value.

^{156}Tb is the main impurity to keep under control, as it presents an almost identical half-life to ^{155}Tb and cannot be removed from the final product by means of decay time. Besides the ground state, henceforth referred to as ^{156}Tb for clarity, the two metastable states ^{156m1}Tb and ^{156m2}Tb are also populated. They both decay through IT (100%) into ^{156}Tb, causing an increase in its activity over time, without the emission of any γ-ray. This complicated decay chain made the cross section measurements challenging and required the use of two different methods.

In the first case, I measured the total activity of ^{156}Tb after a sufficiently long time for the metastable states to be considered decayed. This is therefore a cumulative approach and the measured cross section is reported as $^{cum-156}$Tb.
In the second case, I developed a method to determine the contribution of the three isomers, based on repeated measurement of the samples.
Thirty-minute measurements were taken on each sample for up to 4 days after the EoB in order to study the evolution of ^{156}Tb activity over time. For all samples, an initial increase in activity was observed (Figure 3.47), due to the decay of ^{156m1}Tb and ^{156m2}Tb. After the equilibrium was reached, the activity started to decrease with the ^{156}Tb characteristic decay constant.
I proved the equilibrium condition by fitting the experimental data with the exponential decay equation:

$$A_{156}(t) = A_{156}(t_0)e^{-\lambda_{156}t} \tag{3.8}$$

named as *Fit 1* in Figure 3.47.
In all cases, the ^{156}Tb decay constant derived from *Fit 1* was compatible within uncertainties with the value reported in the literature.

The same data were then fitted with the Bateman equation:

$$\begin{aligned} A_{156}(t) =& A_{156}(t_0)e^{-\lambda_{156}t}+ \\ &+ \frac{\lambda_{156}}{\lambda_{156}-\lambda_{156m1}}A_{156m1}(t_0)[e^{-\lambda_{156m1}t}-e^{-\lambda_{156}t}]+ \\ &+ \frac{\lambda_{156}}{\lambda_{156}-\lambda_{156m2}}A_{156m2}(t_0)[e^{-\lambda_{156m2}t}-e^{-\lambda_{156}t}] \end{aligned} \tag{3.9}$$

named as *Fit 2* in Figure 3.47, where λ_i (with i = 156, 156m1 and 156m2) are constant parameters equal to the recommended values (Table 3.18).
From the EoB activities provided by the fits, the production cross sections were calculated using Eq. 2.9.

The cumulative ^{156}Tb cross sections obtained from Fit 1 and from the first measurement campaign were find to be compatible within the uncertainties.

Also in the case of ^{154}Tb, the ground state and two metastable states m1 and m2 are populated during the irradiation. ^{154m1}Tb and ^{154m2}Tb decay predominantly into ^{154}Gd by electron capture (78.2% and 98.2%, respectively) with detectable γ-ray emission. In the rest of the cases they decay into the ground state of ^{154}Tb.

From the study of the ^{154}Tb activity over time (Figure 3.46), it was observed that the contributions of the metastable states to ^{154}Tb are negligible, as the latter did not deviate from its characteristic exponential trend.

A detailed description of the data analysis and the results of the production cross sections of terbium radioisotopes can be found in Ref. [130], paper of which I am the first author and that is reprinted in Part II of this thesis.

The same data were analysed at a later stage to determine the nuclear cross sections, using the method based on linear systems of equations described in Section 2.2. This procedure could not be applied for ^{156m1}Tb and ^{156m2}Tb due to the large uncertainty of the production cross sections. In the case of ^{156}Tb, only the cumulative cross section was considered.

The results obtained are shown in Figure 3.48 - Figure 3.53, together with TENDL predictions [5]; for completeness, the measured cross section data are reported in the Appendix.

To the best of my knowledge, no experimental data are reported in the literature for these processes. A paper on this work is currently in preparation.

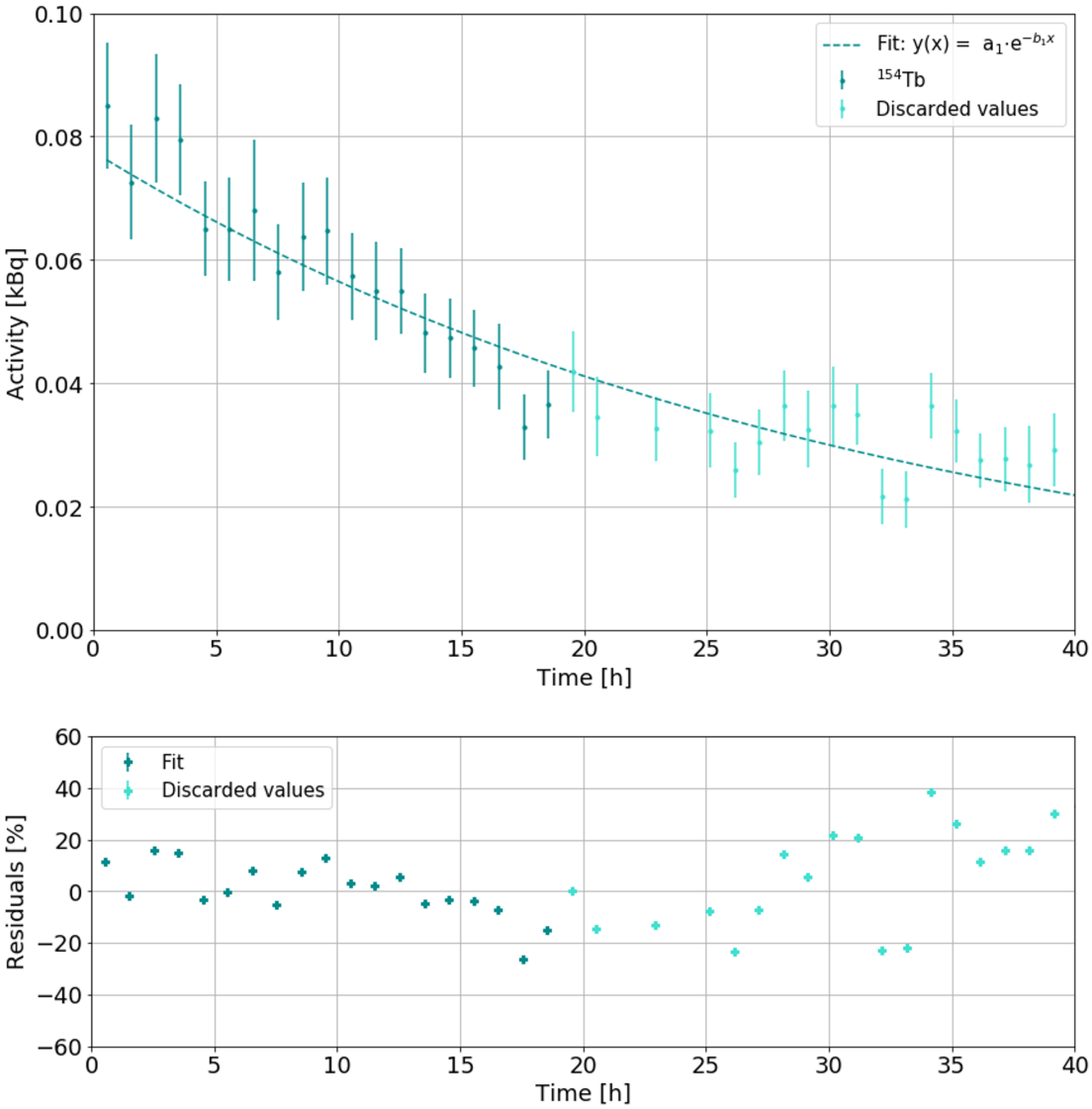

Figure 3.46: ^{154}Tb activity measured over time and exponential fit curve with the corresponding residuals.

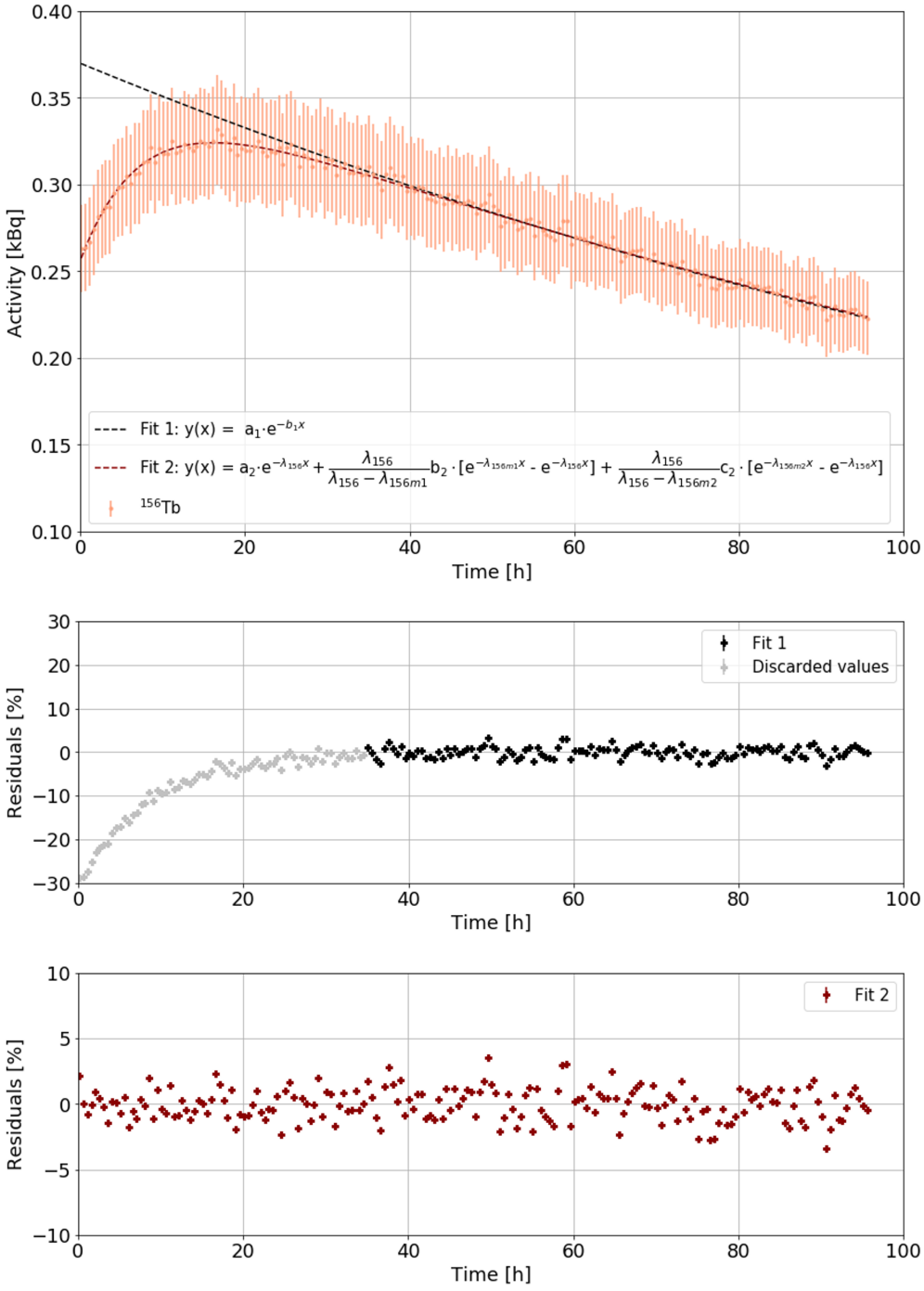

Figure 3.47: ^{156}Tb activity measured over time and fit curves with the corresponding residuals.

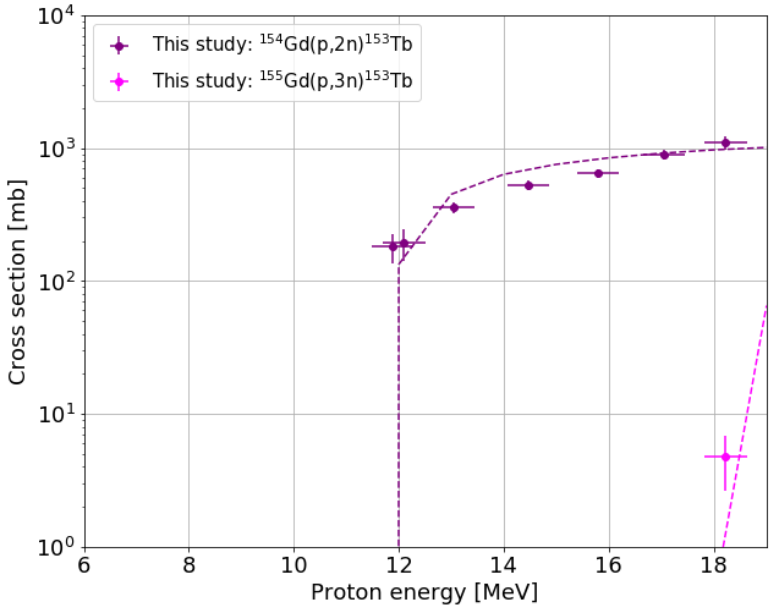

Figure 3.48: ^{154}Gd(p,2n)^{153}Tb and ^{155}Gd(p,3n)^{153}Tb reaction cross sections.

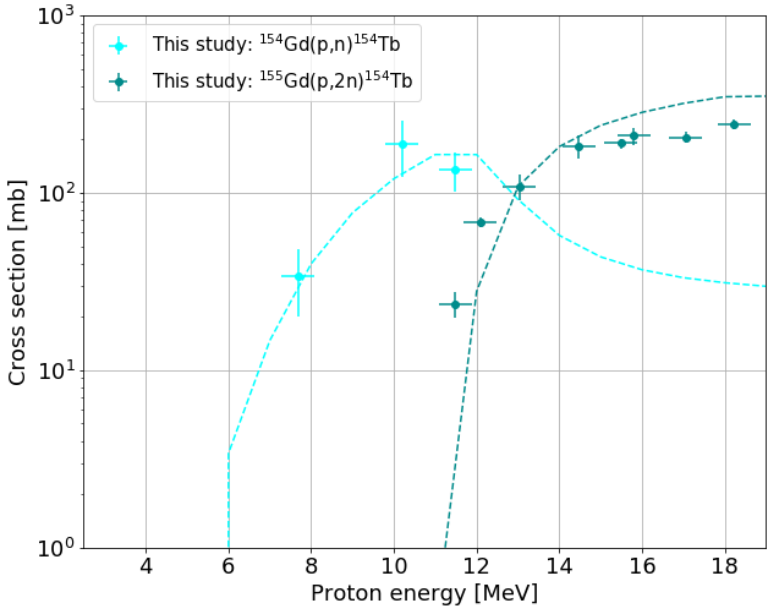

Figure 3.49: ^{154}Gd(p,n)^{154}Tb and ^{155}Gd(p,2n)^{154}Tb reaction cross sections.

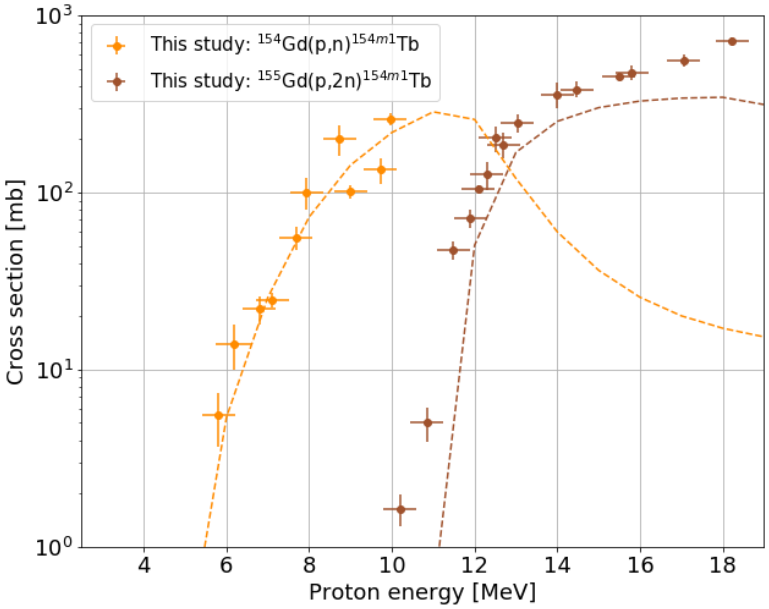

Figure 3.50: ^{154}Gd(p,n)^{154m1}Tb and ^{155}Gd(p,2n)^{154m1}Tb reaction cross sections.

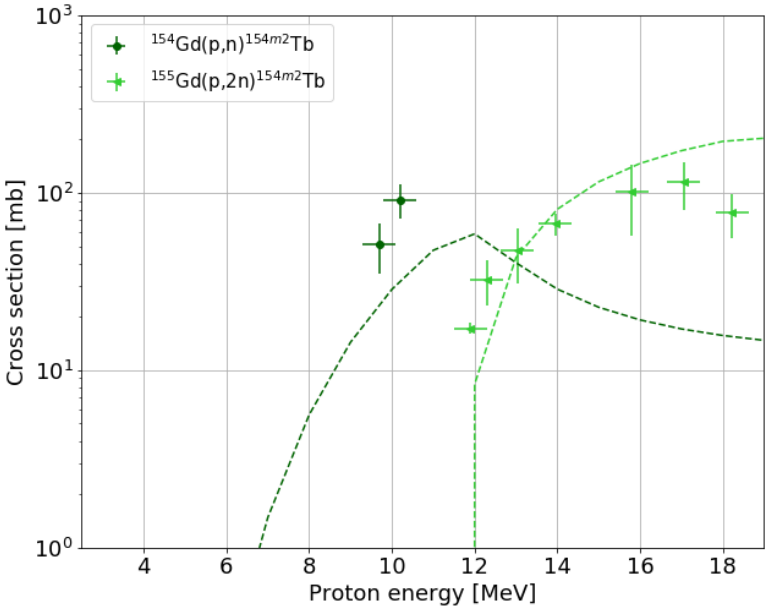

Figure 3.51: ^{154}Gd(p,n)^{154m2}Tb and ^{155}Gd(p,2n)^{154m2}Tb reaction cross sections.

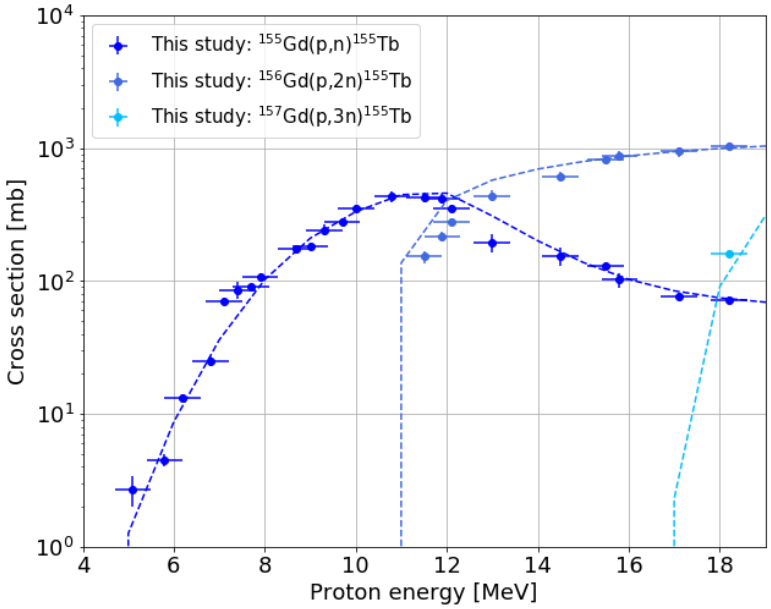

Figure 3.52: ^{155}Gd(p,n)^{155}Tb, ^{156}Gd(p,2n)^{155}Tb and ^{157}Gd(p,3n)^{155}Tb reaction cross sections.

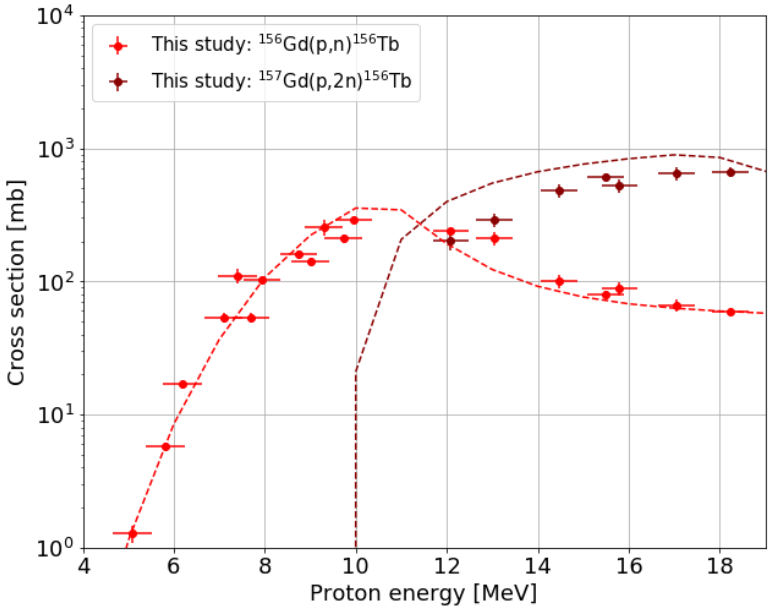

Figure 3.53: Cumulative ^{156}Gd(p,n)^{156}Tb and ^{157}Gd(p,2n)^{156}Tb reaction cross sections.

The production cross section measured from the 91.90% enriched $^{155}Gd_2O_3$ and the 93.30% enriched $^{156}Gd_2O_3$ material, whose isotopic compositions are reported in Table 3.17, are shown in Figure 3.54.

Since most of the observed terbium impurities have shorter half-lives than ^{155}Tb, it is possible to optimize the radionuclidic purity by considering long irradiation times.

Figure 3.55 shows the TTY and radionuclidic purity at saturation, calculated from the cross section measurements for a 91.9% enriched $^{155}Gd_2O_3$ (a) and a 93.3% enriched $^{156}Gd_2O_3$ (b). In the first case, the highest radionuclidic purity is obtained for an input energy of about 11 MeV, corresponding to the threshold energy of the ^{155}Gd(p,2n)^{154}Tb reaction (Figure 3.49 and Figure 3.50). Around this value, a small change in the input energy leads to a significant change in the produced activity of ^{154}Tb and ^{154m1}Tb. The optimal input energy was therefore considered to be 10.5 MeV, leading to a ^{155}Tb yield of 0.54 GBq/μA with a purity of 89% at saturation. In the second case, the highest ^{155}Tb yield and purity can be obtained with the maximum achievable energy. At 17.8 MeV this corresponds to 4.32 GBq/μA with a purity of 63% at saturation.

Short-lived terbium radioisotopes can be removed from the sample by means of decay time, and after about three days ^{156}Tb is the only impurity present, amounting to 7% and 26% for enriched ^{155}Gd and enriched ^{156}Gd, respectively (Figure 3.56). The latter result can be improved by considering cyclotrons capable of delivering more energetic proton beams, as the cross section of the ^{156}Gd(p,2n)^{155}Tb reaction was found to be increasing at 18 MeV, while the production of the main impurity ^{156}Tb has its maximum at around 10 MeV.

A study in collaboration with PSI was carried out to investigate the feasibility of producing high ^{155}Tb activities by proton irradiation of highly-enriched Gd powder and the subsequent radiochemical separation from the target material and impurities.
Two production tests were carried out with the STS at the Bern medical cyclotron, irradiating 38-mg-enriched $^{155}Gd_2O_3$ pellets. The targets were then measured with the HPGe detector to determine the present impurities.

The irradiation parameters and the experimental results are reported in Table 3.19. In Figure 3.57, the experimental results are compared with the predictions based on cross section measurements.

The radiochemical processing of ^{155}Tb and the preclinical studies were performed at PSI [131].

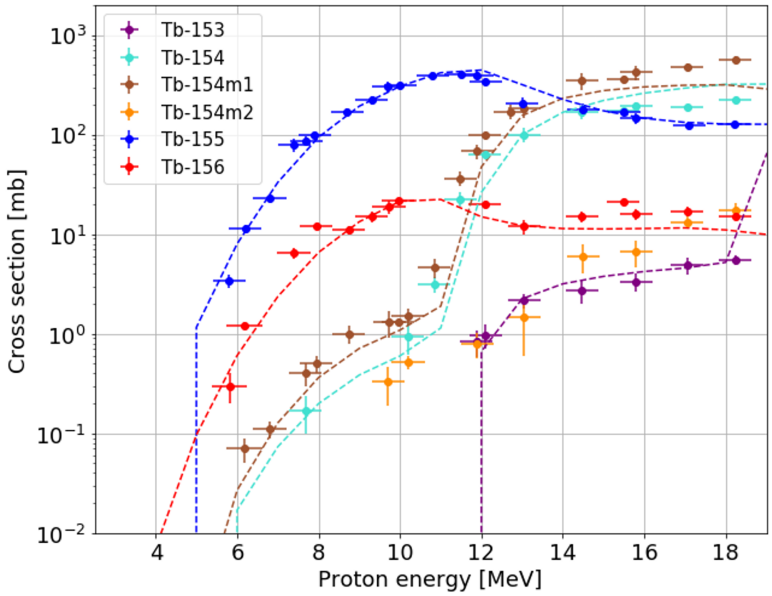

(a)

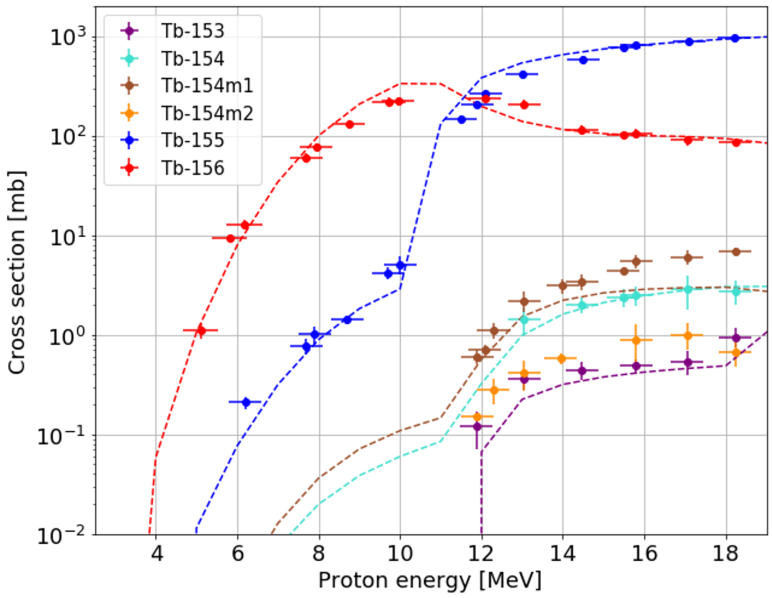

(b)

Figure 3.54: Production cross section of Tb radioisotopes measured from the 91.90% enriched $^{155}Gd_2O_3$ (a) and the 93.30% enriched $^{156}Gd_2O_3$ (b) material.

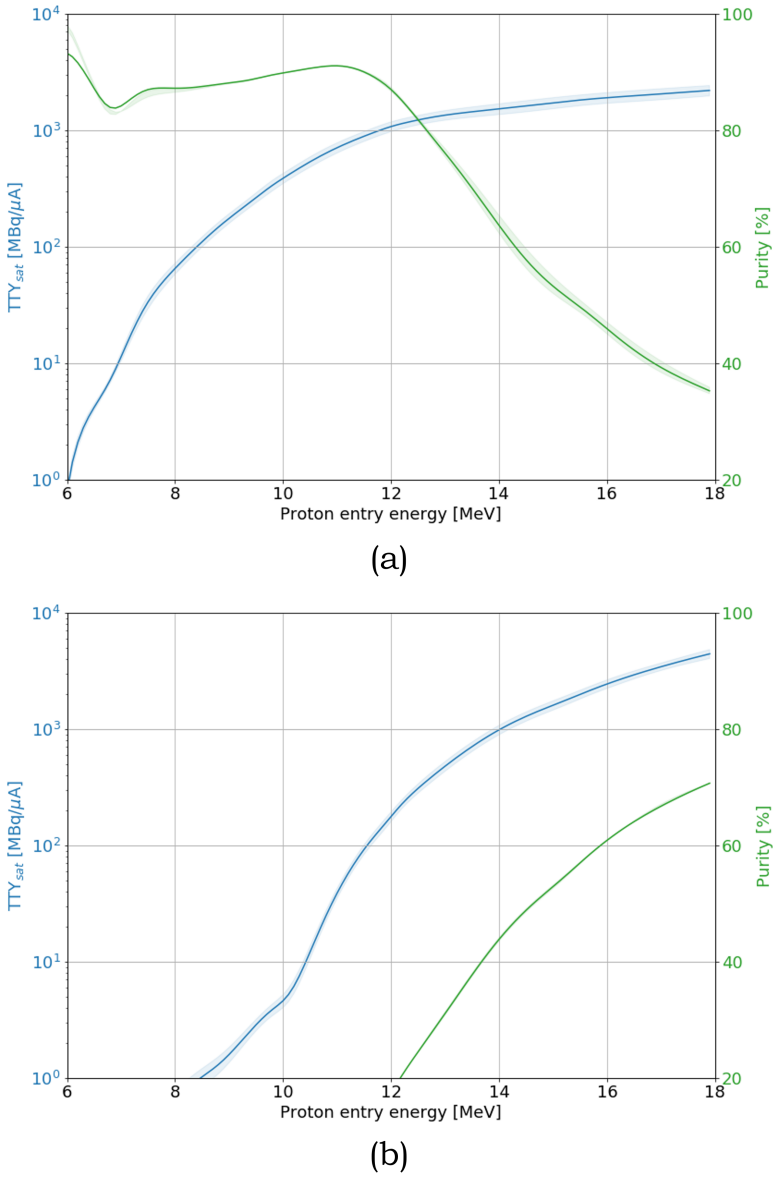

Figure 3.55: ^{155}Tb thick target yield and radionuclidic purity at saturation for a 91.9% enriched $^{155}Gd_2O_3$ (a) and a 93.3% enriched $^{156}Gd_2O_3$ (b) target. The bands correspond to the maximum and minimum yield calculated on the basis of the measured cross sections.

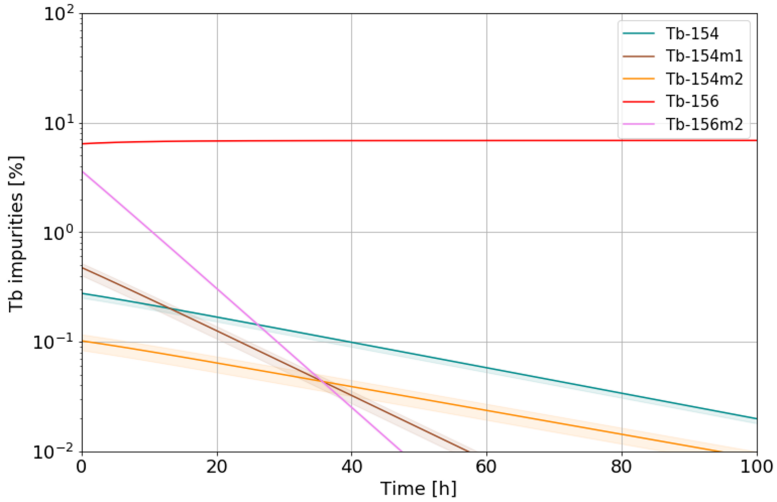

(a)

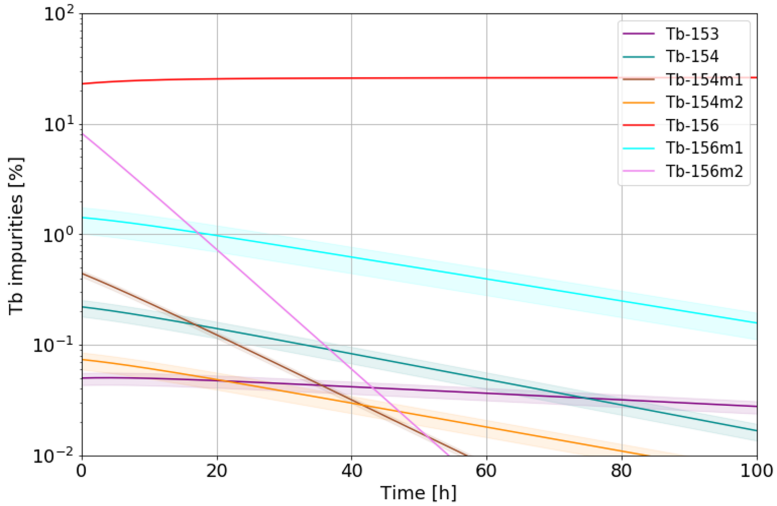

(b)

Figure 3.56: Terbium impurities as a function of time for a 91.9% enriched ^{155}Gd (a) and a 93.3% enriched ^{156}Gd (b) thick target.

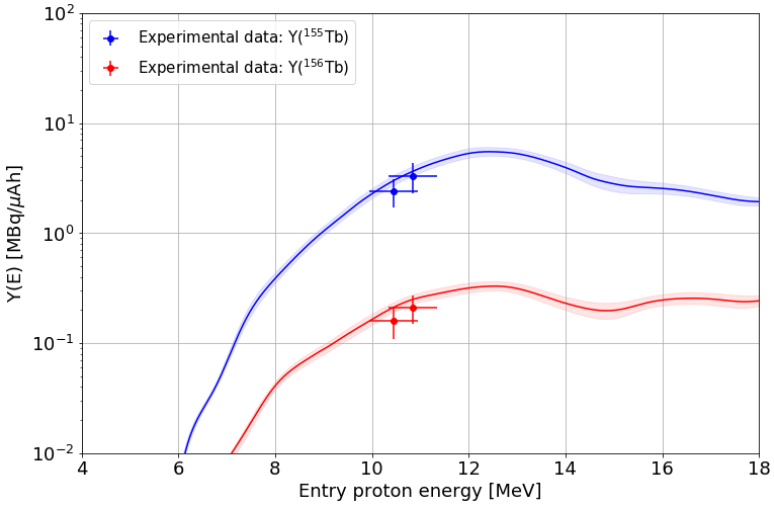

Figure 3.57: ^{155}Tb and ^{156}Tb yields calculated in our irradiation conditions compared to the experimental results. The bands correspond to the maximum and minimum yield derived from the measured cross sections.

Irradiation [#]	E_{in} [MeV]	Q [μAh]	Y(^{155}Tb) [MBq/μAh]	Y(^{156}Tb) [MBq/μAh]	P(96h) [%]
1	(10.9 ± 0.5)	2.4 ± 0.7	3.3 ± 1.0 *(3.6)*	0.21 ± 0.06 *(0.24)*	94.0 ± 0.6 *(93.4)*
2	(10.5 ± 0.5)	0.7 ± 0.2	2.4 ± 0.7 *(3.0)*	0.16 ± 0.05 *(0.21)*	92.1 ± 0.1 *(92.0)*

Table 3.19: Irradiation parameters, ^{155}Tb and ^{156}Tb yields and radionuclidic purity 96 h after the EoB, obtained irradiating the 91.9% enriched $^{155}Gd_2O_3$ pellets. The values in parentheses are the yield calculations based on the cross section measurements.

A three-column procedure allowed the separation of very small amounts of ^{155}Tb (~1 μg) from a massive amount of target material (~40 mg), with a separation yield of 75-90%. This would enable the target mass to be increased in order to produce more activity.

The obtained [^{155}Tb]$TbCl_3$ solution was used for the labelling of somatostatin analogues DOTATOC. It was observed that the activity concentration had a strong impact on the molar activity of the radiolabelling. With the separation, up to 1 GBq of [^{155}Tb]$TbCl_3$ was obtained, which allowed the labelling of biomolecules at 100 MBq/nmol with >99% purity.

The radiotracer was injected into somatostatin positive tumor-bearing mice and SPECT/CT scans were acquired 1, 4 and 24 h after the injection (Figure 3.58). An excellent visualisation of the accumulated radiolabelled compound in the tumours was observed, comparable with that of the same ^{177}Lu- or ^{161}Tb-labelled biomolecule reported in the literature [132].
The successful in vivo SPECT/CT imaging study with ^{155}Tb-DOTATOC demonstrated the applicability of cyclotron-produced ^{155}Tb for imaging purposes.

The detailed description of the production tests, the radiochemical procedures and the preclinical applications of ^{155}Tb-DOTATOC can be found in Ref. [133], which I co-authored.

This study confirmed the excellent prospects of using ^{155}Tb in nuclear medicine and contributed to pave the way towards the use of medical cyclotrons to produce ^{155}Tb for future potential clinical applications. Further studies will be required to establish the impact of ^{156}Tb by investigating how this radioisotope can affect the patient from a dosimetry perspective.

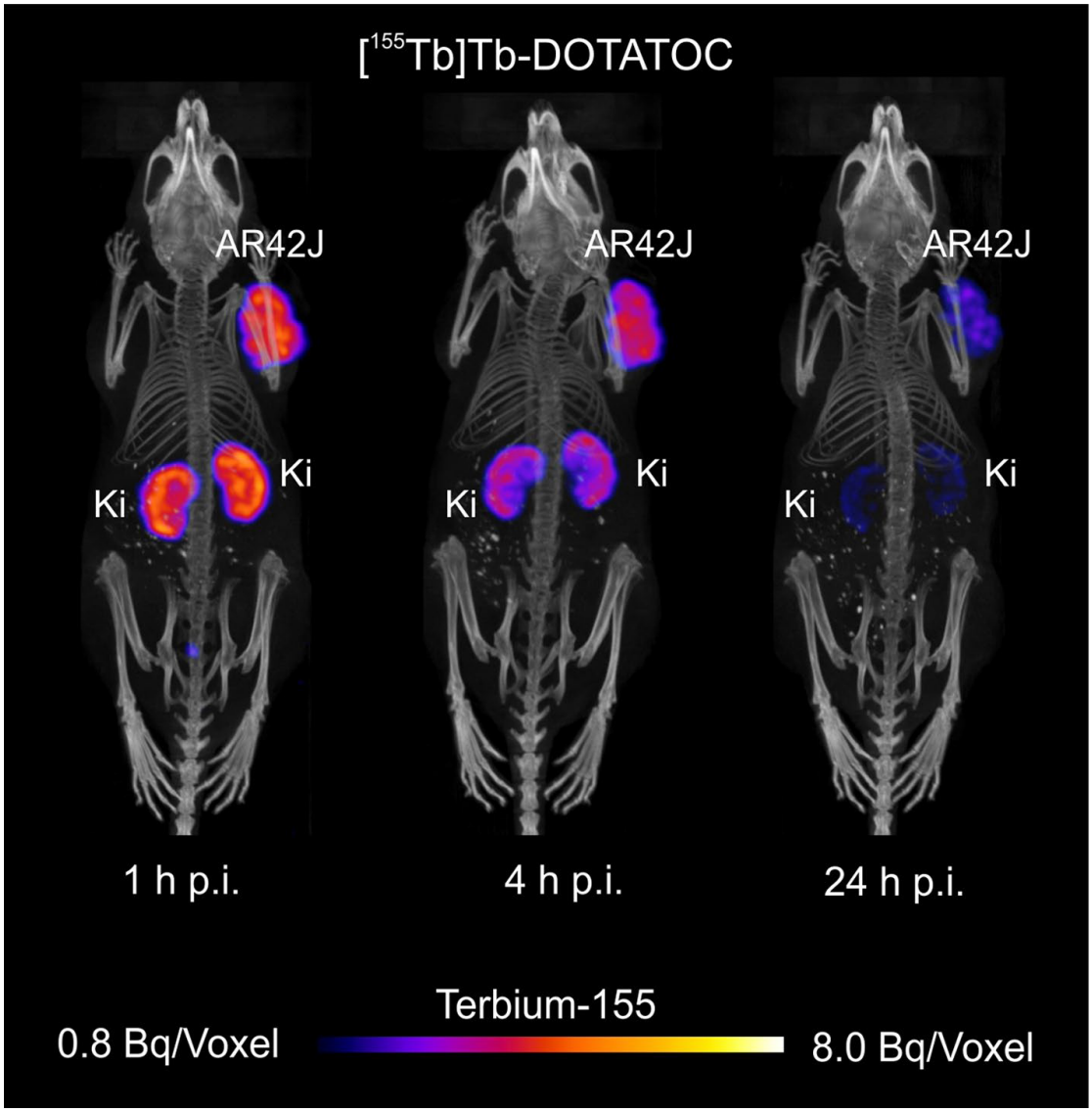

Figure 3.58: In vivo SPECT/CT scans of somatostatin positive tumor-bearing mice injected with [^{155}Tb]Tb-DOTATOC [133]. The scans were acquired 1, 4 and 24 h post injection.

3.6 Erbium-165

Auger electron-emitting radionuclides are receiving increasing interest for the therapeutic advantages they could provide.

In this respect, ^{165}Er [$t_{1/2}$ = 10.36 h, ec: 100%] presents almost ideal characteristics for the treatment of metastatic and disseminated tumours. It decays by electron capture resulting in Auger-electrons emissions of 5.3 keV (65.6%) and 38.4 keV (4.8%), associated with low-energy X-rays [E_X = 47.6 keV (38.1%); 46.7 keV (21.4%)]. The absence of high-energy electrons and γ-ray emissions avoids additional dose absorbed by the patient. The Auger-electron energies emitted by ^{165}Er are similar to those of the intensely studied ^{125}I [$t_{1/2}$ = 59.4 d, ec: 100%], whose highly cytotoxic effects are reported in the literature [134, 135]. However, in contrast to ^{125}I, ^{165}Er has the advantage that it can be coupled to diagnostic partners such as ^{44}Sc for theranostic applications, due to the similar chemical characteristics of rare earth metals [136, 137].

The main ^{165}Er production routes are based on the irradiation with proton or deuterium beams of Ho and Er targets [138–147].
In the framework of a collaboration with PSI, ^{165}Er direct production via the ^{165}Ho(p,n)^{165}Er reaction was previously studied at the Bern medical cyclotron but resulted to be unsuitable for large-scale production do to the presence of non-radioactive Er in large quantities, making the radiolabelling impossible [147].

I investigated the indirect ^{165}Er production via the ^{166}Er(p,2n)^{165}Tm $\rightarrow$ ^{165}Er nuclear reaction, by irradiating natural Er_2O_3 and enriched $^{166}Er_2O_3$ targets, whose isotopic compositions are reported in Table 3.20.

	^{162}Er	^{164}Er	^{166}Er	^{167}Er	^{168}Er	^{170}Er
Natural Er_2O_3 [%]	0.139	1.601	33.503	22.869	26.978	14.910
Enr. $^{166}Er_2O_3$ [%]	<0.01	0.02	98.1	1.33	0.45	0.10

Table 3.20: Isotopic fractions of the natural Er_2O_3 powder purchased by GoodFellow [35] and the enriched $^{166}Er_2O_3$ powder by Isoflex [36].

Despite the use of the highly enriched $^{166}Er_2O_3$ powder, several Tm radioisotopes are produced during the irradiation (Table 3.21), affecting the radionuclidic purity. To optimize the production of ^{165}Tm, I carried out a detailed study of the nuclear reaction cross sections involved in the formation of Tm radioisotopes in the energy range of interest, using the method described in Section 2.2.

Radioisotope	$t_{1/2}$	Decay mode: [%]	E_γ [keV]	BR [%]
^{165}Tm	30.06*(3)* h	ec + β^+: 100	242.917*(7)*	35.5*(17)*
^{166}Tm	7.70*(3)* h	ec + β^+: 100	778.814*(15)*	19.1*(12)*
^{167}Tm	9.25*(2)* d	ec: 100	207.801*(15)*	42*(8)*
^{168}Tm	93.1*(2)* d	ec + β^+: 99.990	198.251*(2)*	54.49*(16)*
^{170}Tm	128.6*(3)* d	β^-: 99.869	84.25474*(8)*	2.48*(6)*

Table 3.21: Decay properties of thulium radioisotopes. The values in parentheses are the uncertainties referred to the last digits of the value.

In the case of radionuclides produced by three reactions, such as ^{165}Tm and ^{167}Tm, a third enriched material had to be included to solve the linear system of equations. For this purpose, the cross sections measured from enriched $^{167}Er_2O_3$ and enriched $^{168}Er_2O_3$ as part of a study on the production of ^{167}Tm (Section 3.7) were considered.

The results of the nuclear cross section measurements are shown in Figure 3.59-Figure 3.63, together with TENDL predictions [5] and the experimental data available in the literature [148, 149]. For completeness, the measured cross section data are reported in the Appendix.

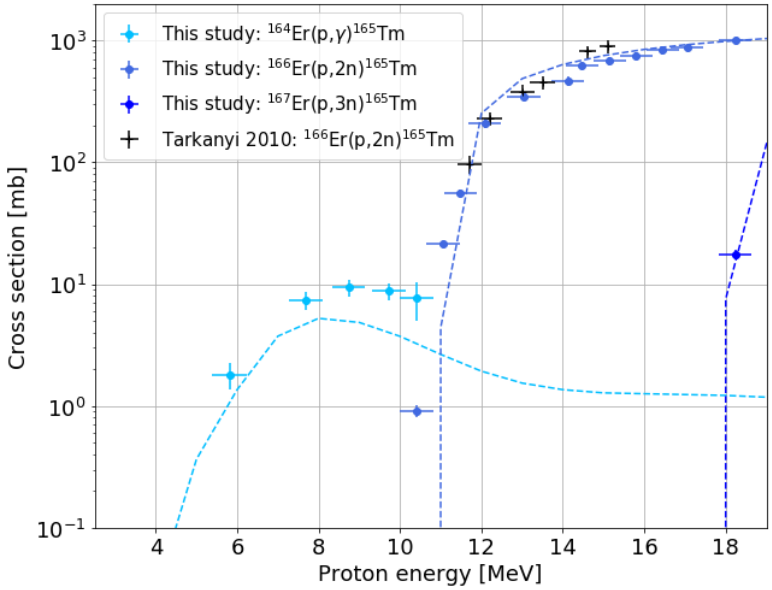

Figure 3.59: ^{164}Er(p,γ)^{165}Tm, ^{166}Er(p,2n)^{165}Tm and ^{167}Er(p,3n)^{165}Tm reaction cross sections.

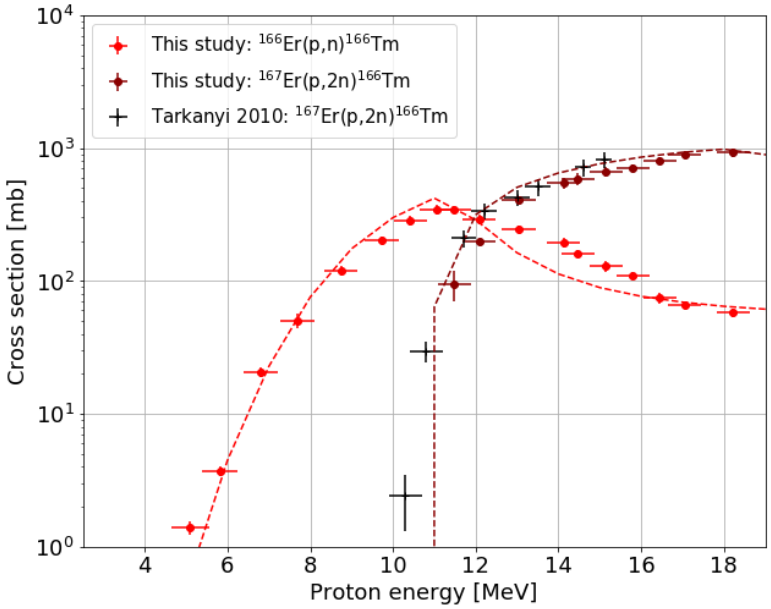

Figure 3.60: ^{166}Er(p,n)^{166}Tm and ^{167}Er(p,2n)^{166}Tm reaction cross sections.

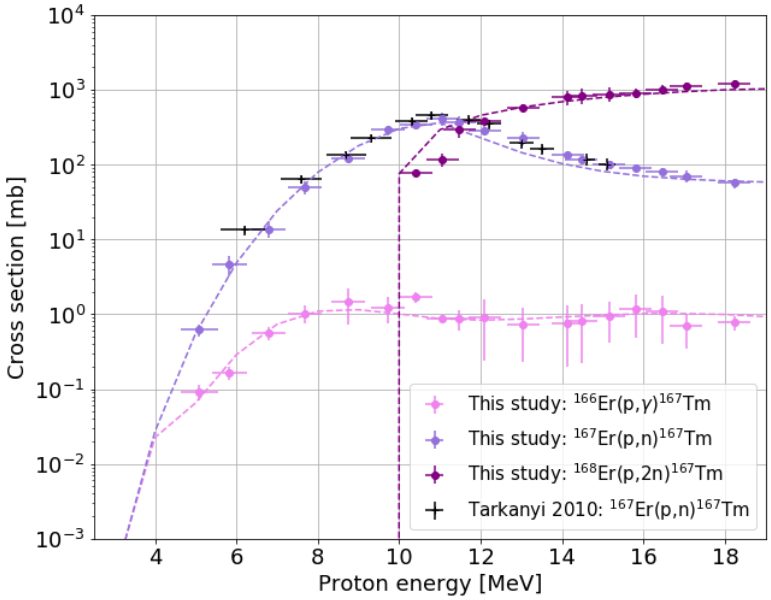

Figure 3.61: ^{166}Er(p,γ)^{167}Tm, ^{167}Er(p,n)^{167}Tm and ^{168}Er(p,2n)^{167}Tm reaction cross sections.

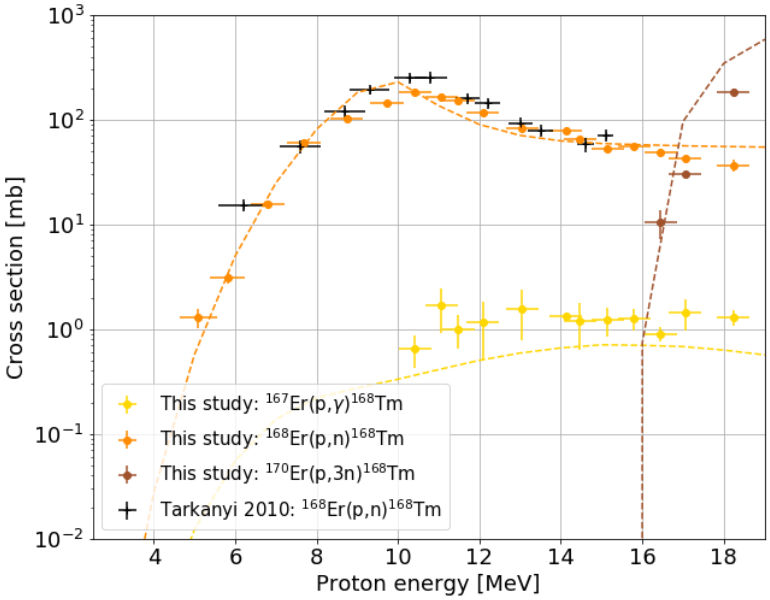

Figure 3.62: ^{167}Er(p,γ)^{168}Tm, ^{168}Er(p,n)^{168}Tm and ^{170}Er(p,3n)^{168}Tm reaction cross sections.

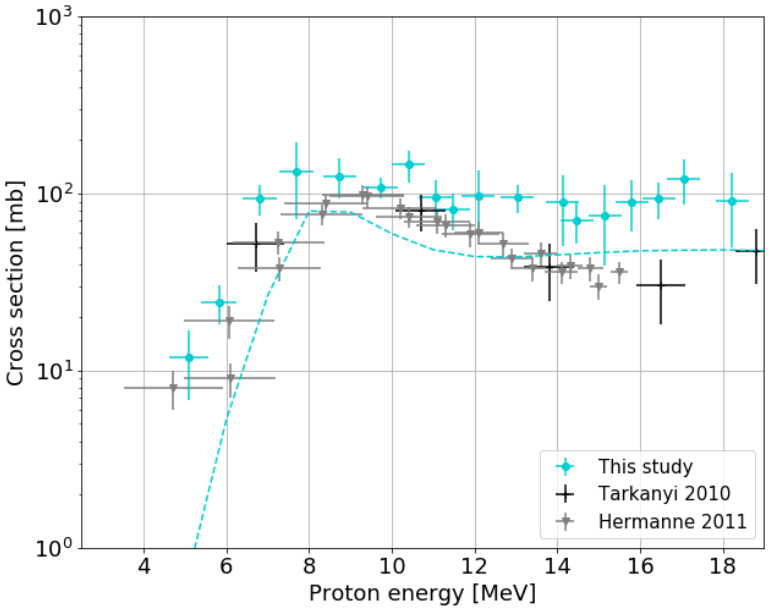

Figure 3.63: ^{170}Er(p,n)^{170}Tm reaction cross sections.

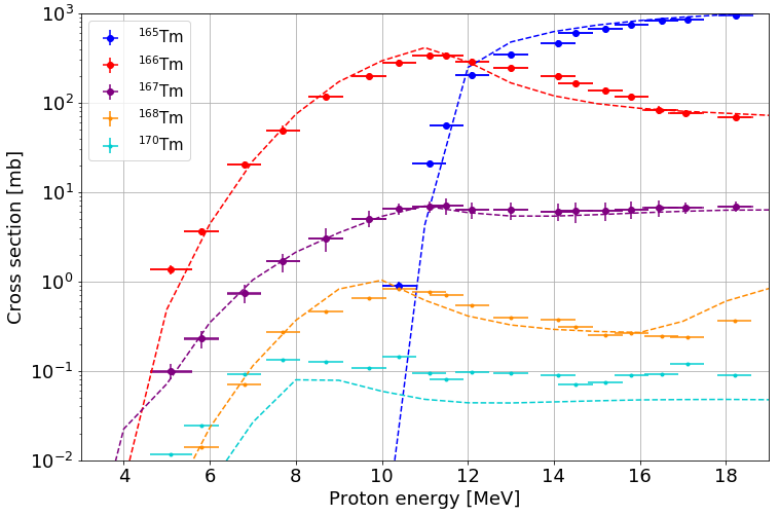

Figure 3.64: Production cross section of Tm radioisotopes for the 98.1% enriched $^{166}Er_2O_3$ material.

Figure 3.64 shows the production cross sections measured from the enriched $^{166}Er_2O_3$ material. In the case of ^{168}Tm and ^{170}Tm, the cross sections could not be measured directly due to the low isotopic percentage of ^{168}Er and ^{170}Er in the target material and were therefore derived from the nuclear cross sections.

The highest ^{165}Tm production yield can be achieved with the maximum available energy. The energy range, and thus the target thickness, must be carefully chosen to minimize the production of ^{166}Tm, whose cross section exhibits a maximum at about 11 MeV. Since ^{166}Tm has a shorter half-life than ^{165}Tm, long irradiation times can be evaluated to further reduce its contribution. In this case, however, it is necessary to keep under control the other long-lived Tm impurities.

Setting the input energy at 17.8 MeV, I studied the Tm radioisotope yields and the radionuclidic purity as a function of the target thickness for different irradiation times (Figure 3.65).

Despite a larger production of ^{167}Tm, ^{168}Tm and ^{170}Tm was observed, the radionuclidic purity was found to increase for longer irradiation times and is optimized by a target thickness of about 200 μm. However, it has been observed that for the pellet to be robust enough to handle, it must present a thickness of at least 240 μm. This leads to an output energy of 15.9 MeV.

Under these conditions, a ^{165}Tm production yield of about 1 GBq/μA with a purity of 84% can be achieved for an irradiation time of 30 h.

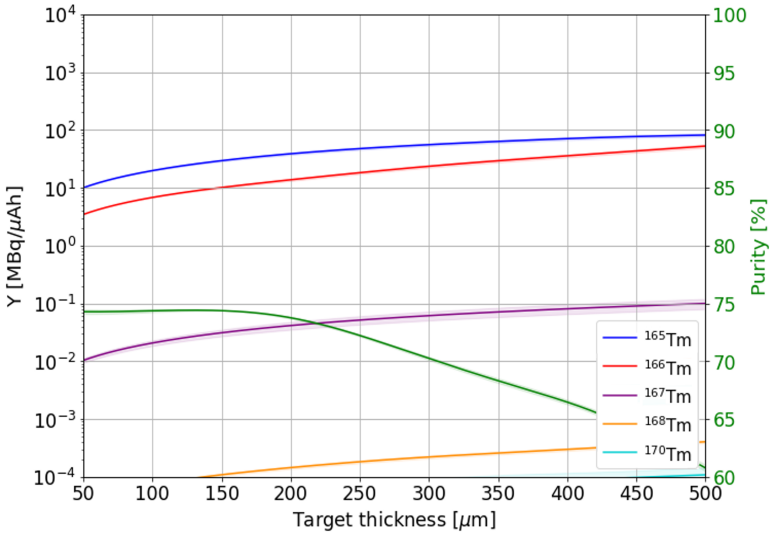

(a)

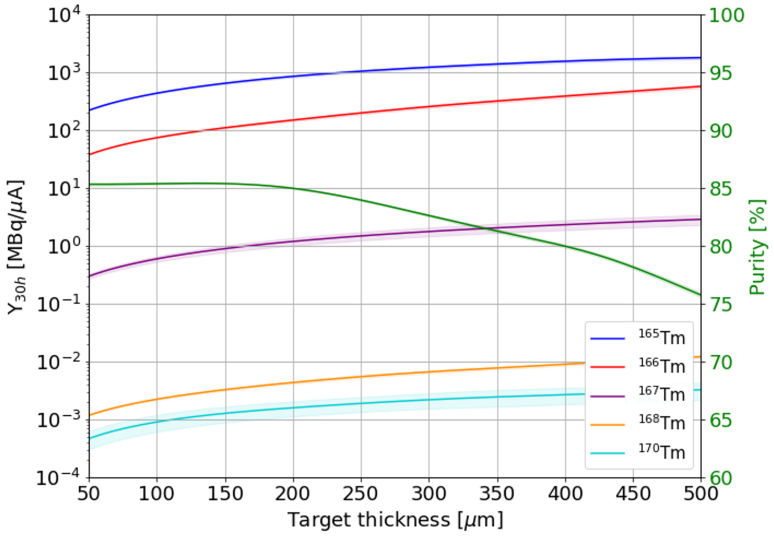

(b)

Figure 3.65: Tm radioisotope yields and radionuclidic purity as a function of the target thickness for an irradiation time of 1 h (a) and 30 h (b). The input energy is set to 17.8 MeV. The bands correspond to the maximum and minimum yield calculated on the basis of the measured cross sections.

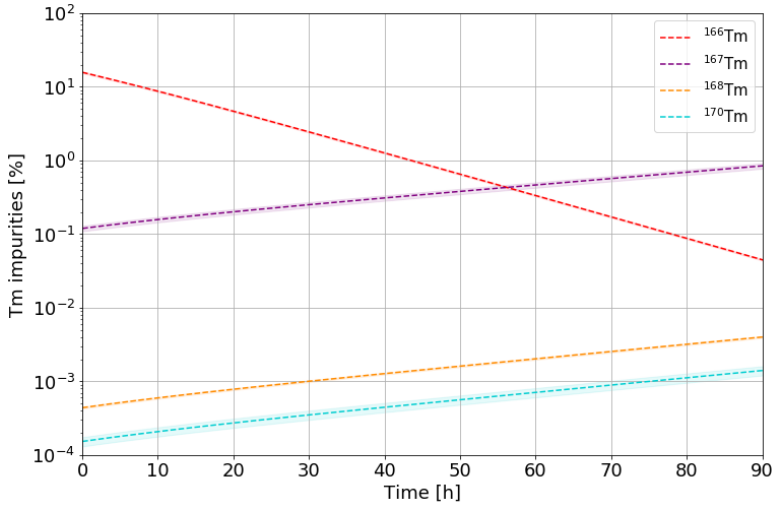

Figure 3.66: Thulium impurities as a function of decay time, considering an irradiation time of 30 h in the energy range 17.8-15.9 MeV. The bands correspond to the maximum and minimum yield calculated on the basis of the measured cross sections.

^{166}Tm is the main impurity, accounting for about 15.7%. Its amount can be reduced by letting the sample decay, as shown in Figure 3.66.

On the basis of these data, it is necessary to investigate the best timing for performing the radiochemical separation and fixing the Tm mother radioisotopes on the generator column in order to minimize the presence of Er carriers, produced by the decay of Tm radioisotopes. In this respect, it is important to underline that all thulium impurities decay into stable isotopes of Er.

A decay time of about 30 h results in a radionuclidic purity of more than 97%, retaining almost 50% of the produced ^{165}Tm activity (Figure 3.67). Considering an ^{165}Er in-growth time of 1.012 d, as suggested by Tarkányi et al. in Ref. [143], it is possible to obtain a specific activity of $11{\cdot}10^3$ TBq/μA.mmol$_{Er}$, assuming a 100% efficiency of the chemical separation and elution procedures.
The effective purity of the product depends on the actual efficiency of radiochemical processes, not easy in the case of lanthanides.

To confirm the calculations based on cross section measurements, I performed two production tests in the BTL, in order to achieve a higher input energy. I irradiated two enriched $^{166}Er_2O_3$ pellets, 0.24 mm and 0.46 mm thick, to verify the impact of the target thickness on radionuclidic purity. The pellets were placed in the same version of the coin used for the production of ^{47}Sc (Section 3.1), resulting in an input energy of (18.2 ± 0.4) MeV.

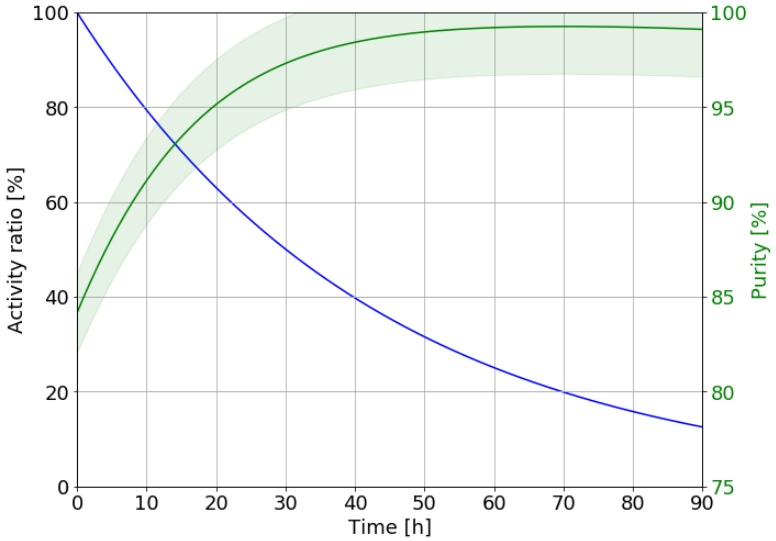

Figure 3.67: ^{165}Tm activity ratio and radionuclidic purity as a function of the decay time, considering an irradiation time of 30 h in the energy range 17.8-15.9 MeV. The bands correspond to the maximum and minimum yield calculated on the basis of the measured cross sections.

The irradiation parameters and the measured ^{165}Tm yield and radionuclidic purity are reported in Table 3.22. In Figure 3.68, the experimental results are compared with the predictions based on cross section measurements.

Since, according to TENDL [5], the ^{166}Er(p,2n)^{165}Tm reaction cross section has a maximum at about 20 MeV, the use of 24 MeV cyclotrons could be considered in order to achieve higher yields. In this case, however, the ^{170}Er(p,3n)^{168}Tm reaction, which causes an increase in the production of the long-lived ^{168}Tm, must be taken into account. The use of materials with higher isotopic enrichment can be evaluated to reduce this contribution.

A paper about this work, of which I am the first author, will be submitted to Applied Radiation and Isotopes [150]. Further studies are being carried out at PSI to investigate radiochemical procedures that optimize the generator preparation.

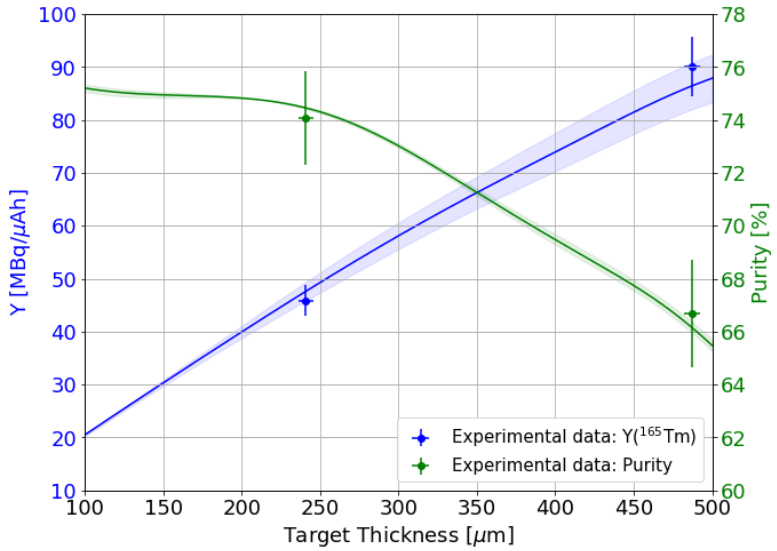

Figure 3.68: ^{165}Tm production yield and purity calculated in our irradiation conditions compared to the experimental results. The bands correspond to the maximum and minimum yield derived from the measured cross sections.

Irradiation [#]	Δx pellet [μm]	E_{in} [MeV]	Q 10^{-3} [μAh]	Y(^{165}Tm) [MBq/μAh]	P(EoB) [%]
1	0.49 ± 0.01	18.2 ± 0.4	0.86 ± 0.09	90 ± 6 *(86)*	67 ± 2 *(67)*
2	0.24 ± 0.01	18.2 ± 0.4	0.94 ± 0.04	46 ± 3 *(47)*	74 ± 2 *(75)*

Table 3.22: Irradiation parameters, ^{165}Tm yield and radionuclidic purity at the EoB, obtained irradiating 91.9% enriched $^{166}Er_2O_3$ pellets. The values in parentheses are the yield calculations based on the cross section measurements.

3.7 Thulium-167

^{167}Tm [$t_{1/2}$ = 9.25 d, ec: 100%, E_γ = 208 keV (42%)] is a potential radionuclide for both medical diagnostics and therapy. It exhibits high soft electron emission [5.5 keV (114%), 39.7 keV (5.8%), 47.3 keV (19%)], making it suitable for Auger-electron therapy [151], and a 208-keV γ-ray emission, which enables SPECT imaging [152, 153]. Dosimetric calculations showed a relatively high tumour-to-normal-tissue dose rate value [154, 155], however, the accompanying radiobiological effects still need to be investigated.

Several production routes based on charged particles are reported in the literature [148, 156–160]. In particular, a collaboration between CERN-MEDICIS and PSI investigated the mass separation process of ^{167}Tm produced by proton irradiation of natural Er_2O_3, achieving a collection efficiency of 11-20% [161].

As part of a project ongoing at PSI aimed at the production of ^{167}Tm, I investigated the ^{167}Er(p,n)^{167}Tm and ^{168}Er(p,2n)^{167}Tm reactions at the Bern medical cyclotron, by irradiating erbium oxides enriched in ^{167}Er and in ^{168}Er. The isotopic composition of the materials used for cross section measurements are reported in Table 3.23. The $^{168}Er_2O_3$ is marked as (A).

	^{162}Er	^{164}Er	^{166}Er	^{167}Er	^{168}Er	^{170}Er
Enr. $^{167}Er_2O_3$ [%]	0	0.01	0.96	96.30	2.57	0.16
Enr. $^{168}Er_2O_3$ (A) [%]	-	-	0.37	0.72	98.30	0.61
Enr. $^{168}Er_2O_3$ (B) [%]	0.002	0.022	0.433	1.121	97.243	1.179

Table 3.23: Isotopic fractions of the enriched Er_2O_3 powders purchased by Isoflex [36].

As mentioned in Section 3.6, the results obtained in this study for ^{165}Tm, ^{167}Tm and ^{168}Tm from enriched $^{167}Er_2O_3$ and for ^{168}Tm from enriched $^{168}Er_2O_3$ were used to derive the nuclear cross sections of Tm radioisotopes.

The measured production cross sections are shown in Figure 3.69. In case of ^{170}Tm, the cross sections could not be measured directly due to the low isotopic percentage of ^{170}Er in the target material and were therefore derived from the nuclear cross sections.

In the case of enriched $^{167}Er_2O_3$ the optimal proton input energy is about 12.5 MeV, a compromise to maximize the production of ^{167}Tm while minimizing ^{166}Tm and ^{168}Tm. For the enriched $^{168}Er_2O_3$ material, the maximum ^{167}Tm activity is achievable for the highest reachable energy.

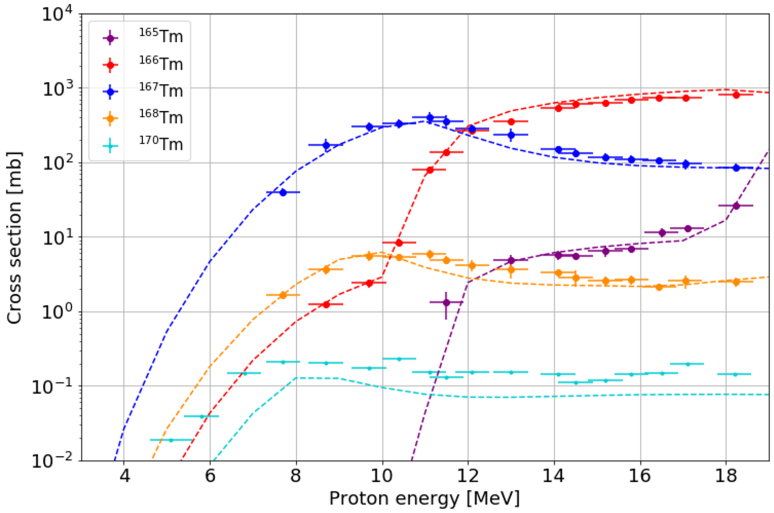

(a)

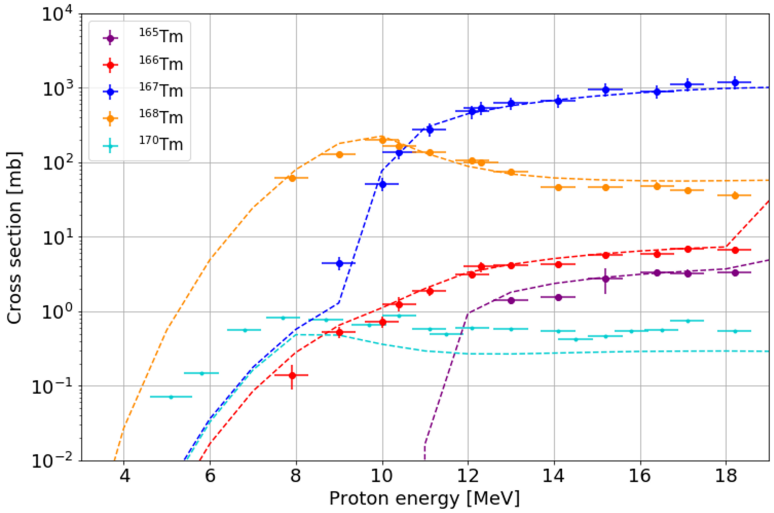

(b)

Figure 3.69: Production cross sections of Tm radioisotopes measured from the 96.3% enriched $^{167}Er_2O_3$ (a) and the 98.1% enriched $^{168}Er_2O_3$ (b) material.

Particular attention must be paid to ^{168}Tm and ^{170}Tm, which have half-lives of 93.1 d and 129 d, respectively. The presence of these radioisotopes increases for very long irradiation times and can cause a decrease in purity after the EoB, limiting the application period of the ^{167}Tm-labelled radiopharmaceutical.

Considering a target thickness of 275 μm and setting the entry energy at the optimal value, I investigated the thulium impurities as a function of the irradiation time (Figure 3.70).

In case of $^{167}Er_2O_3$, the main impurity is the short-lived ^{166}Tm, which can be eliminated from the sample by means of decay time and, under saturation conditions, becomes less than 1% after about 40 h after the EoB (Figure 3.71-a). In the case of $^{168}Er_2O_3$, the main impurity in saturation conditions is the long-lived ^{168}Tm, which remains almost constant at 1% until about 90 h after the EoB (Figure 3.71-b).

As expected from the cross section measurements, the ^{168}Er(p,2n) production route results in a higher ^{167}Tm activity than the ^{167}Er(p,n) (about 2.8 GBq/μA vs. 0.85 GBq/μA in saturation condition), but with lower radionuclidic purity after an appropriate cooling time due to the co-production of ^{168}Tm (98.6% vs. 99.4% after 5 days).

To confirm the calculations based on cross section measurements, two production tests for each material were performed in the BTL.
In the case of $^{168}Er_2O_3$, the irradiation were performed using another batch of material respect to the one used for cross section measurements, presenting a different isotopic composition (marked as (B) in Table 3.23).
To estimate the production yields of thulium radioisotopes were therefore used the nuclear cross sections reported in Section 3.6.

The irradiation parameters and the measured ^{167}Tm yield and purity are reported in Table 3.24 and Table 3.25 for the enriched $^{167}Er_2O_3$ and the $^{168}Er_2O_3$, respectively.
The long-lived ^{170}Tm was not observed in any production test. In case of $^{167}Er_2O_3$, the difference observed for^{166}Tm between the experimental and the expected yield may be due to the uncertainty in the energy of the protons leaving the target, which is close to the threshold of the ^{167}Er(p,2n)^{166}Tm reaction (Figure 3.60).

Further tests are planned to evaluate the best production route. A paper on this work, of which I will be co-author, is in preparation.

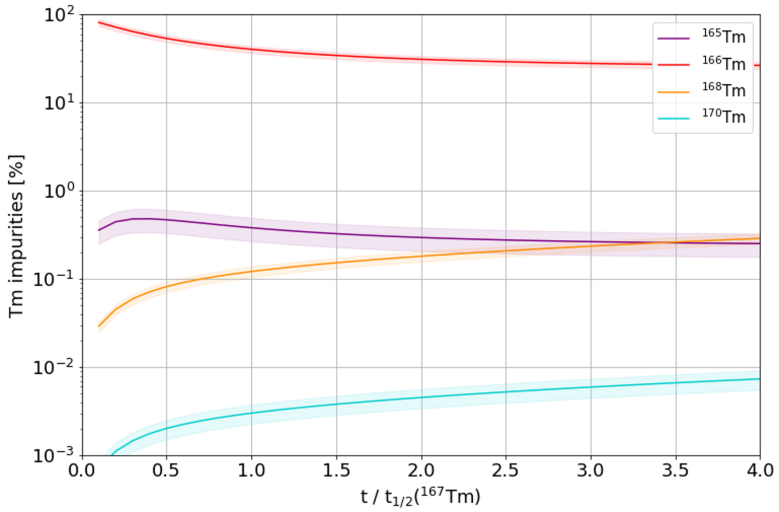

(a)

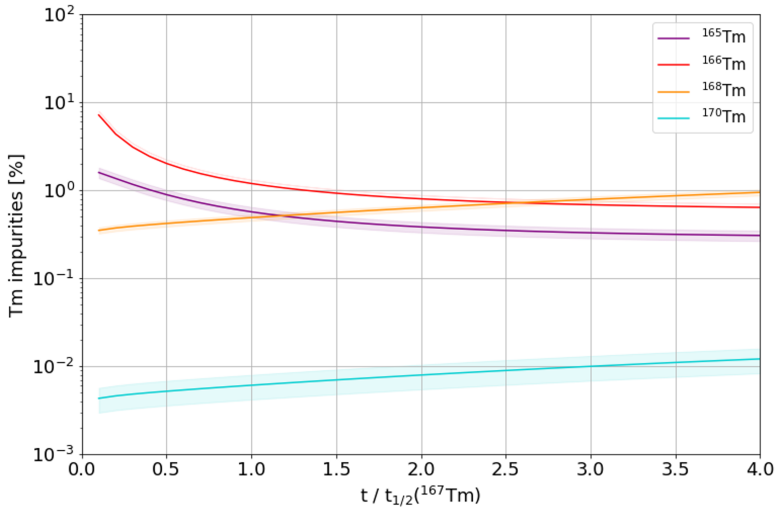

(b)

Figure 3.70: Tm impurities as a function of the irradiation time for a 275-µm 96.3% enriched $^{167}Er_2O_3$ (a) and a 275-µm 98.1% enriched $^{168}Er_2O_3$ (b) target. The irradiation time is expressed as multiple of $t_{1/2}(^{167}Tm)$.

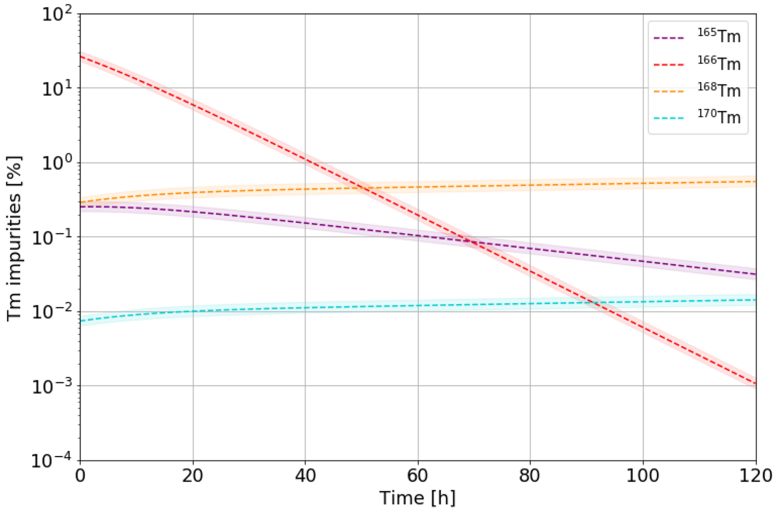

(a)

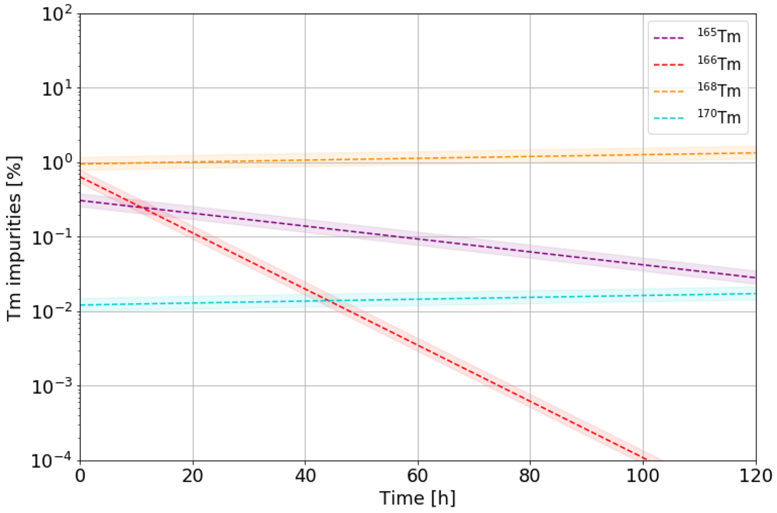

(b)

Figure 3.71: Tm impurities over time EoB for a 275-μm 96.3% enriched $^{167}Er_2O_3$ (a) and a 275-μm 98.3% enriched $^{168}Er_2O_3$ (b) target. The impurities EoB are calculated in saturation conditions.

Irradiation [#]	Δx pellet [μm]	E_{in} [MeV]	Q 10^{-3} [μAh]	Y(^{167}Tm) [MBq/μAh]	P(EoB) [%]	P(5 d) [%]
1	0.26 ± 0.01	12.7 ± 0.4	0.85 ± 0.04	2.3 ± 0.5 *(2.6)*	6 ± 1 *(10)*	99.5 ± 0.1 *(99.6)*
2	0.28 ± 0.01	12.7 ± 0.4	0.85 ± 0.04	2.6 ± 0.5 *(3.0)*	6 ± 1 *(11)*	99.6 ± 0.1 *(99.6)*

Table 3.24: Irradiation parameters, ^{167}Tm yield and radionuclidic purity EoB, obtained irradiating 96.3% enriched $^{167}Er_2O_3$ pellets. The values in parentheses are the yield calculations based on the cross section measurements.

Irradiation [#]	Δx pellet [μm]	E_{in} [MeV]	Q 10^{-3} [μAh]	Y(^{167}Tm) [MBq/μAh]	P(EoB) [%]	P(5 d) [%]
1	0.28 ± 0.01	18.2 ± 0.4	0.83 ± 0.04	8.2 ± 1.6 *(9.9)*	72 ± 4 *(77)*	99.1 ± 0.2 *(99.2)*
2	0.29 ± 0.01	18.2 ± 0.4	0.97 ± 0.05	8.5 ± 1.7 *(10.4)*	74 ± 4 *(77)*	98.8 ± 0.4 *(99.2)*

Table 3.25: Irradiation parameters, ^{167}Tm yield and radionuclidic purity EoB, obtained irradiating 97.243% enriched $^{168}Er_2O_3$ pellets. The values in parentheses are the yield calculations based on the cross section measurements.

3.8 Summary

In the framework of my PhD work, several non-standard radioisotopes have been investigated at the Bern medical cyclotron. By accurately measuring the nuclear cross sections involved, it was possible to determine the irradiation parameters that maximize production yield and radionuclidic purity.
A summary of the obtained results is given in Table 3.26.

Isotope	Reaction	Target	Mass [mg]	Charge [μAh]	Y [MBq/μAh]
^{44}Sc	(p,n)	$^{enr-44}$CaO pellet	30	27	600
^{47}Sc	(p,α)	$^{enr-50}TiO_2$ pellet	35	3.9 E-3	1
^{61}Cu	(p,α)	$^{enr-64}$Zn pellet	40	2.7 E-4	140
^{64}Cu	(p,n)	$^{enr-65}$Cu pellet	30	1.3 E-3	70
	(p,α)	$^{enr-67}$ZnO pellet	59	2.7 E-4	16
^{67}Cu	(p,α)	$^{enr-70}$ZnO pellet	34	1.7 E-3	1
^{68}Ga	(p,n)	$^{enr-68}$Zn pellet	40	0.24	4500
^{155}Tb	(p,n)	$^{enr-155}Gd_2O_3$ pellet	40	1.1 E-3	4
	(p,2n)	$^{enr-156}Gd_2O_3$ pellet	40	1.1 E-3	14
^{165}Tm	(p,2n)	$^{enr-166}Er_2O_3$ pellet	49	0.9 E-3	90
^{167}Tm	(p,n)	$^{enr-167}Er_2O_3$ pellet	40	0.85 E-3	3
	(p,2n)	$^{enr-168}Er_2O_3$ pellet	40	1.0 E-3	9

Table 3.26: Main achievements in non-standard radioisotope production obtained at the Bern medical cyclotron in the framework of this thesis. The integrated current corresponds to the amount of protons hitting the target material.

References

[1] Z. Talip et al. "A Step-by-Step Guide for the Novel Radiometal Production for Medical Applications: Case Studies with ^{68}Ga, ^{44}Sc, ^{177}Lu and ^{161}Tb". In: *Molecules* 25.4 (2020), pp. 966–995. DOI: 10.3390/molecules25040966.

[2] B. Gutfilen et al. "Copper-64: a real theranostic agent". In: *Drug Des Devel Ther* 2.12 (2018), pp. 3235–3245. DOI: 10.2147/DDDT.S170879.

[3] IAEA. *Live Chart of Nuclides, available online*. Last access 10 January 2023. URL: https://nds.iaea.org/relnsd/vcharthtml/VChartHTML.html.

[4] CIAAW. *Isotopic Composition of the Elements*. Last access 10 January 2023. URL: https://www.ciaaw.org/isotopic-abundances.htm.

[5] A. J. Koning and D. Rochman. "Modern Nuclear Data Evaluation With The TALYS Code System". In: *Nuclear Data Sheets* 113 (2012), pp. 2841–1934. DOI: doi.org/10.1016/j.nds.2012.11.002.

[6] IAEA. *Experimental Nuclear Reaction Data (EXFOR)*. Last access 10 January 2023. URL: https://www-nds.iaea.org/exfor/.

[7] S. Takács et al. "Investigation of the ^{nat}Mo(p,x)^{96mg}Tc nuclear reaction to monitor proton beams: New measurements and consequences on the earlier reported data". In: *Nuclear Instruments and Methods in Physics Research B* 198 (2002), pp. 183–196.

[8] V. N. Levkowskij. "Activation Cross Sections for the Nuclides of Medium Mass Region (A=40-100) with Protons and α-particles at Medium (E=10-50 MeV) energies". In: *Inter-Vesti, Moscow* (1991).

[9] T. S. Carzaniga et al. "Measurement of ^{43}Sc and ^{44}Sc production cross-section with an 18 MeV medical PET cyclotron". In: *Applied Radiation and Isotopes* 129 (2017), pp. 96 –102. DOI: 10.1016/j.apradiso.2017.08.013.

[10] N. P. van der Meulen et al. "Cyclotron production of ^{44}Sc: From bench to bedside". In: *Nuclear Medicine and Biology* 42.9 (2015), pp. 745–751. DOI: 10.1016/j.nucmedbio.2015.05.005.

[11] C. Müller et al. "Promises of Cyclotron-Produced ^{44}Sc as a Diagnostic Match for Trivalent β^--emitters: In Vitro and In Vivo Study of a ^{44}Sc-DOTA-Folate Conjugate". In: *Journal of Nuclear Medicine* 54.12 (2013), pp. 2168–2174. DOI: 10.2967/jnumed.113.123810.

[12] C. Grignon et al. "Nuclear medical imaging using $\beta^+\gamma$ coincidences from ^{44}Sc radio-nuclide with liquid xenon as detection medium". In: *Nuclear Instruments and Methods in Physics Research Section A: Accelerators, Spectrometers, Detectors and Associated Equipment* 571.1 (2007), pp. 142–145. DOI: 10.1016/j.nima.2006.10.048.

[13] S. Krajewski et al. "Cyclotron production of ^{44}Sc for clinical application". In: *Radiochimica Acta* 101.5 (2013), pp. 333–338. DOI: 10.1524/ract.2013.2032.

[14] C. Müller et al. "Promising Prospects for ^{44}Sc-/^{47}Sc-Based Theragnostics: Application of ^{47}Sc for Radionuclide Tumor Therapy in Mice". In: *Journal of Nuclear Medicine* 55.10 (2014), pp. 1658–1664. DOI: 10.2967/jnumed.114.141614.

[15] T. S. Carzaniga and S. Braccini. "Cross-section measurement of ^{44m}Sc, ^{47}Sc, ^{48}Sc and ^{47}Ca for an optimized ^{47}Sc production with an 18 MeV medical PET cyclotron". In: *Applied Radiation and Isotopes* 143 (2019), pp. 18–23. DOI: 10.1016/j.apradiso.2018.10.015.

[16] M. Sitarz et al. "Production of Sc medical radioisotopes with proton and deuteron beams". In: *Applied Radiation and Isotopes* 142 (2018), pp. 104–112. DOI: 10.1016/j.apradiso.2018.09.025.

[17] R. Misiak et al. "^{47}Sc production development by cyclotron irradiation of ^{48}Ca". In: *Journal of Radioanalytical and Nuclear Chemistry* 313 (2017), pp. 429–434. ISSN: 2. DOI: 10.1007/s10967-017-5321-z.

[18] C. Shaun Loveless et al. "Cyclotron Production and Separation of Scandium Radionuclides from Natural Titanium Metal and Titanium Dioxide Targets". In: *Journal of Nuclear Medicine* 62.1 (2021), pp. 131–136. DOI: 10.2967/jnumed.120.242941.

[19] F. Roesch. "Scandium-44: benefits of a long-lived PET radionuclide available from the ^{44}Ti/^{44}Sc generator system." In: *Current radiopharmaceuticals* 5.3 (2012), pp. 187–201. DOI: 10.2174/1874471011205030187.

[20] V. Radchenko et al. "Separation of ^{44}Ti from proton irradiated scandium by using solid-phase extraction chromatography and design of ^{44}Ti/^{44}Sc generator system". In: *Journal of Chromatography A* 1477 (2016), pp. 39–46. DOI: 10.1016/j.chroma.2016.11.047.

[21] K. Szkliniarz et al. "Production of medical Sc radioisotopes with an alpha particle beam". In: *Applied Radiation and Isotopes* 118 (2016), pp. 182–189. DOI: 10.1016/j.apradiso.2016.07.001.

[22] K. Minegishi et al. "Production of scandium-43 and -47 from a powdery calcium oxide target via the $^{nat/44}$Ca(α,x)-channel". In: *Applied Radiation and Isotopes* 116 (2016), pp. 8–12. DOI: 10.1016/j.apradiso.2016.07.017.

[23] V. Starovoitova et al. “Accelerator-based photoproduction of promising beta-emitters ^{67}Cu and ^{47}Sc”. In: *Journal of Radioanalytical and Nuclear Chemistry* (Mar. 2015). DOI: 10.1007/s10967-015-4039-z.

[24] M. Yagi and K. Kondo. “Preparation of carrier-free ^{47}Sc by the ^{48}Ti(γ,p) reaction”. In: *The International Journal of Applied Radiation and Isotopes* 28.5 (1977), pp. 463–468. DOI: 10.1016/0020-708X(77)90178-8.

[25] M. Mamtimin et al. “Sc-47 production from titanium targets using electron linacs”. In: *Applied Radiation and Isotopes* 102 (2015), pp. 1–4. ISSN: 0969-8043. DOI: 10.1016/j.apradiso.2015.04.012.

[26] K. A. Domnanich et al. “^{47}Sc as useful $\beta^{\{}$-emitter for the radiotheragnostic paradigm: a comparative study of feasible production routes”. In: *EJNMMI Radiopharmacy and Chemistry* 2 (2017). DOI: 10.1186/s41181-017-0024-x.

[27] K. L. Kolsky et al. “Radiochemical purification of no-carrier-added scandium-47 for radioimmunotherapy.” In: *Appl Radiat Isot.* 12 (1998), pp. 1541–1549. ISSN: 49. DOI: 10.1016/s0969-8043(98)00016-5.

[28] S. F. Hosseini et al. “Theoretical assessment and targeted modeling of TiO_2 in reactor towards the scandium radioisotopes estimation”. In: *Applied Radiation and Isotopes* 127 (2017), pp. 116–121. DOI: 10.1016/j.apradiso.2017.05.016.

[29] M. Benešová et al. “Albumin-Binding PSMA Ligands: Optimization of the Tissue Distribution Profile”. In: *Molecular Pharmaceutics* 15 (3 2018), pp. 934–946. DOI: 10.1021/acs.molpharmaceut.7b00877.

[30] C. A. Umbricht et al. “^{44}Sc-PSMA-617 for radiotheragnostics in tandem with ^{177}Lu-PSMA-617—preclinical investigations in comparison with ^{68}Ga-PSMA-11 and ^{68}Ga-PSMA-617”. In: *EJNMMI Research* 7.9 (2017). DOI: 10.1186/s13550-017-0257-4.

[31] N. P. van der Meulen et al. “Developments toward the implementation of ^{44}Sc production at a medical cyclotron”. In: *Molecules* 25 (2020), pp. 1–16. DOI: 10.3390/molecules25204706.

[32] M. T. Durán et al. “Half-life measurement of ^{44}Sc and ^{44m}Sc”. In: *Applied Radiation and Isotopes* 190 (2022), p. 110507. DOI: 10.1016/j.apradiso.2022.110507.

[33] F. Juget et al. “Activity measurement of ^{44}Sc and calibration of activity measurement instruments on production sites and clinics”. In: *Molecules* 28 (2023), p. 1345. DOI: 10.3390/molecules28031345.

[34] E. Gadioli et al. “Emission of alpha particles in the interaction of 10-85 MeV protons with ^{48,50}Ti”. In: *Zeitschrift fur Physik A Hadrons and Nuclei* 301.4 (1981), pp. 289–300. DOI: 10.1007/BF01421692.

[35] *GoodFellow: Your global supplier for materials*. https://www.goodfellow.com/.

[36] *ISOFLEX: Isotopes for Science, Medicine and Industry*. https://www.isoflex.com/.

[37] G. Dellepiane et al. "^{47}Sc and ^{46}Sc cross-section measurement for an optimized ^{47}Sc production with an 18 MeV medical PET cyclotron". In: *Applied Radiation and Isotopes* 189 (2022), p. 110428. DOI: 10.1016/j.apradiso.2022.110428.

[38] H. A. Williams et al. "A comparison of PET imaging characteristics of various copper radioisotopes". In: *European Journal of Nuclear Medicine and Molecular Imaging* 32.12 (2005). DOI: 10.1007/s00259-005-1906-9.

[39] *Production of Emerging Radionuclides towards Theranostic Applications: Copper-61, Scandium-43 and -44, and Yttrium-86*. TECDOC Series 1955. Vienna: INTERNATIONAL ATOMIC ENERGY AGENCY, 2021. ISBN: 978-92-0-107321-1. URL: https://www.iaea.org/publications/14857/production-of-emerging-radionuclides-towards-theranostic-applications-copper-61-scandium-43-and-44-and-yttrium-86.

[40] P. Rowshanfarzad et al. "An overview of copper radionuclides and production of 61Cu by proton irradiation of natZn at a medical cyclotron". In: *Applied Radiation and Isotopes* 64.12 (2006), pp. 1563–1573. ISSN: 0969-8043. DOI: 10.1016/j.apradiso.2005.11.012.

[41] C. Champion et al. "Comparison between Three Promising β^--emitting Radionuclides, ^{67}Cu, ^{47}Sc and ^{161}Tb, with Emphasis on Doses Delivered to Minimal Residual Disease". In: *Theranostics* 6(10) (2016), pp. 1611–1618. DOI: 10.7150/thno.15132.

[42] F. Szelecsényi et al. "Excitation functions of proton induced nuclear reactions on enriched ^{61}Ni and ^{64}Ni: Possibility of production of no-carrier-added ^{61}Cu and ^{64}Cu at a small cyclotron". In: *Applied Radiation and Isotopes* 44.3 (1993), pp. 575–580. DOI: 10.1016/0969-8043(93)90172-7.

[43] D. W. McCarthy et al. "High purity production and potential applications of copper-60 and copper-61". In: *Nucl Med Biol.* 26.4 (1999), pp. 351–358. DOI: 10.1016/s0969-8051(98)00113-9.

[44] F. Szelecsényi et al. "Production possibility of ^{61}Cu using proton induced nuclear reactions on zinc for PET studies". In: *Journal of Radioanalytical and Nuclear Chemistry* 263 (2005), pp. 539–546. ISSN: 2. DOI: 10.1007/s10967-005-0089-y.

[45] A. H. Asad et al. "Cyclotron production of ^{61}Cu using natural Zn enriched ^{64}Zn targets". In: *AIP Conference Proceedings* 1509.91 (2012), pp. 91–95. DOI: 10.1063/1.4773947.

[46] S. J. C. do Carmo et al. “Fast and cost-effective cyclotron production of 61Cu using a natZn liquid target: an opportunity for radiopharmaceutical production and RD”. In: *Dalton Trans.* 46.42 (2017), pp. 14556–14560. DOI: 10.1039/c7dt01836c.

[47] D. W. McCarthy et al. “Efficient production of high specific activity ^{64}Cu using a biomedical cyclotron”. In: *Nuclear Medicine and Biology* 24.1 (1997), pp. 35–43. DOI: 10.1016/S0969-8051(96)00157-6.

[48] F. Szelecsényi et al. “Investigation of the ^{66}Zn(p,2pn)^{64}Cu and ^{68}Zn(p,x)^{64}Cu nuclear processes up to 100 MeV: Production of ^{64}Cu”. In: *Nuclear Instruments and Methods in Physics Research Section B: Beam Interactions with Materials and Atoms* 240.3 (2005), pp. 625–637. DOI: 10.1016/j.nimb.2005.05.057.

[49] F. Szelecsényi et al. “Excitation function of (p,α) nuclear reaction on enriched ^{67}Zn: possibility of production of ^{64}Cu at low energy cyclotron”. In: *Radiochimica Acta* 102.6 (2014), pp. 465–472. DOI: doi:10.1515/ract-2013-2145.

[50] K. Hilgers et al. “Cross-section measurements of the nuclear reactions ^{nat}Zn(d,x)^{64}Cu, ^{66}Zn(d,α)^{64}Cu and ^{68}Zn(p,αn)^{64}Cu for production of ^{64}Cu and technical developments for small-scale production of ^{67}Cu via the ^{70}Zn(p,α)^{67}Cu process”. In: *Appl Radiat Isot.* 59 (2003), pp. 343–351. DOI: 10.1016/s0969-8043(03)00199-4.

[51] T. Stoll et al. “Excitation functions of proton induced reactions on ^{68}Zn from threshold up to 71 MeV, with specific reference to the production of ^{67}Cu”. In: *Radiochimica Acta* 90.6 (2002), pp. 309–313. DOI: 10.1524/ract.2002.90.6.309.

[52] F. Szelecsényi et al. “Investigation of the ^{68}Zn(p, 2p)^{67}Cu nuclear reaction: New measurements up to 40 MeV and compilation up to 100 MeV”. In: *Nuclear Instruments Methods in Physics Research Section B-beam Interactions With Materials and Atoms* 267 (June 2009), pp. 1877–1881. DOI: 10.1016/j.nimb.2009.03.097.

[53] S. Kastleiner et al. “Possibility of production of ^{67}Cu at a small-sized cyclotron via the (p,α)-reaction on enriched ^{67}Zn”. In: *Radiochim. Acta* 84 (1999), pp. 107–110.

[54] G. Pupillo et al. “Production of ^{67}Cu by enriched ^{70}Zn targets: first measurements of formation cross sections of ^{67}Cu, ^{64}Cu, ^{67}Ga ^{66}Ga, ^{69m}Zn and ^{65}Zn in interactions of ^{70}Zn with protons above 45 MeV”. In: *Radiochimica Acta* 108.8 (2020), pp. 593–602. DOI: 10.1515/ract-2019-3199.

[55] L. Mou et al. “A method and a target for the production of ^{67}Cu”. In: *European Patent* EP3794615 (2021).

[56] S. Takács et al. “Activation Cross Section Measurements of Deuteron Induced Reactions on ^{nat}Ni with Special Reference to Beam Monitoring and Production of for ^{61}Cu Medical Purpose”. In: *Radiochimica Acta* 76.1-2 (1997), pp. 15–24. DOI: 10.1524/ract.1997.76.12.15.

[57] J. Kozempel et al. “Preparation of ^{67}Cu via deuteron irradiation of ^{70}Zn”. In: *Radiochimica Acta* 100.7 (2012), pp. 419–424. DOI: 10.1524/ract.2012.1939.

[58] E. Nigron et al. “Is ^{70}Zn(d,x)^{67}Cu the Best Way to Produce ^{67}Cu for Medical Applications?” In: *Frontiers in Medicine* 8 (2021). DOI: 10.3389/fmed.2021.674617.

[59] H. Muramatsu et al. “Alpha particle bombardment of natural nickel target for the production of ^{61}Cu”. In: *The International Journal of Applied Radiation and Isotopes* 29.11 (1978), 611–614. DOI: 10.1016/0020-708x(78)90094-7.

[60] F. Szelecsényi et al. “Production possibility of ^{60,61,62}Cu radioisotopes by alpha induced reactions on cobalt for PET studies”. In: *Nuclear Instruments and Methods in Physics Research Section B: Beam Interactions with Materials and Atoms* 187.2 (2002), pp. 153–163. DOI: 10.1016/S0168-583X(01)00923-5.

[61] T. Fukumura et al. “Practical production of ^{61}Cu using natural Co target and its simple purification with a chelating resin for ^{61}Cu-ATSM”. In: *Radiochimica Acta* 92.4-6 (2004), pp. 209–214. DOI: 10.1524/ract.92.4.209.35593.

[62] Y. Skakun and S. M. Qaim. “Excitation function of the ^{64}Ni(α,p)^{67}Cu reaction for production of ^{67}Cu”. In: *Applied Radiation and Isotopes* 60.1 (2004), pp. 33–39. DOI: 10.1016/j.apradiso.2003.09.003.

[63] O. S. Deiev et al. “Photonuclear reactions ^{65}Cu(γ,n)^{64}Cu and ^{63}Cu(γ,xn)$^{63-x}$Cu cross-sections in the energy range $E_{\gamma max}$ = 35–94 MeV”. In: *Chinese Physics C* (2022).

[64] V. Starovoitova et al. “^{67}Cu photonuclear production”. In: *AIP Conference Proceedings* 1336 (2011), pp. 189–196. DOI: 10.1063/1.3586150.

[65] R. A. Aliev et al. “Photonuclear production and radiochemical separation of medically relevant radionuclides: ^{67}Cu”. In: *Journal of Radioanalytical and Nuclear Chemistry* 321 (2019), pp. 125–132. DOI: 10.1007/s10967-019-06576-9.

[66] G. H. Hovhannisyan et al. “Photonuclear production of the medical isotope ^{67}Cu”. In: *Nuclear Instruments and Methods in Physics Research Section B: Beam Interactions with Materials and Atoms* 498 (2021), pp. 48–51. DOI: 10.1016/j.nimb.2021.04.016.

[67] T. H. Bokhari et al. “Production of low and high specific activity ^{64}Cu in a reactor”. In: *Journal of Radioanalytical and Nuclear Chemistry* 284.2 (2010), pp. 265–271. DOI: 10.1007/s10967-010-0519-3.

[68] T. Kin et al. “New Production Routes for Medical Isotopes ^{64}Cu and ^{67}Cu Using Accelerator Neutrons”. In: *Journal of the Physical Society of Japan* 82 (2013), pp. 4201–. DOI: 10.7566/JPSJ.82.034201.

[69] M. S. Uddin et al. “Radiochemical measurement of neutron-spectrum averaged cross sections for the formation of ^{64}Cu and ^{67}Cu via the (n,p) reaction at a TRIGA Mark-II reactor: Feasibility of simultaneous production of the theragnostic pair ^{64}Cu/^{67}Cu”. In: *Radiochimica Acta* 102.6 (2014), pp. 473–480. DOI: 10.1515/ract-2013-2199.

[70] M. Kawabata et al. “Production and separation of ^{64}Cu and ^{67}Cu using 14 MeV neutrons”. In: *Journal of Radioanalytical and Nuclear Chemistry* 303 (Feb. 2015), pp. 1205–1209. DOI: 10.1007/s10967-014-3488-0.

[71] A. M. Johnsen et al. “Reactor production of ^{64}Cu and ^{67}Cu using enriched zinc target material”. In: *J Radioanal Nucl Chem* 305 (2015), 61—71. DOI: 10.1007/s10967-015-4032-6.

[72] M. Capogni et al. “^{64}Cu production by 14 MeV neutron beam”. In: *Journal of Neutron Research* 22.2-3 (2020), pp. 257–264. DOI: 10.3233/JNR-190140.

[73] G. Dellepiane. “Activity measurement of a ^{64}Cu sample activated by a 14 MeV neutron beam”. In: *IL NUOVO CIMENTO C* 45 (04 2022). DOI: 10.1393/ncc/i2022-22084-9.

[74] R. Chakravarty et al. “Reactor produced [^{64}Cu]$CuCl_2$ as a PET radiopharmaceutical for cancer imaging: from radiochemistry laboratory to nuclear medicine clinic”. In: *Annals of Nuclear Medicine* 34 (12 2020), pp. 899–910. DOI: 10.1007/s12149-020-01522-2.

[75] S. Mirzadeh et al. “Production of no-carrier added ^{67}Cu”. In: *International Journal of Radiation Applications and Instrumentation. Part A. Applied Radiation and Isotopes* 37.1 (1986), pp. 29–36. DOI: 10.1016/0883-2889(86)90192-9.

[76] *TRACE Science International*. http://www.tracesciences.com/.

[77] *CortecNet*. https://cortecnet.com/.

[78] B. L. Cohen et al. “(p,pn) and (p, αn) Excitation Functions”. In: *Phys. Rev.* 94 (3 1954), pp. 620–625. DOI: 10.1103/PhysRev.94.620.

[79] M. S. Uddin et al. “Excitation functions of the proton induced nuclear reactions on natZn up to 40 MeV”. In: *Nuclear Instruments and Methods in Physics Research Section B: Beam Interactions with Materials and Atoms* 258.2 (2007), pp. 313–320. ISSN: 0168-583X. DOI: 10.1016/j.nimb.2007.02.089.

[80] A. H. Asad et al. “Excitation functions of natZn(p,x) nuclear reactions with proton beam energy below 18 MeV”. In: *Applied Radiation and Isotopes* 94 (2014), pp. 67–71. ISSN: 0969-8043. DOI: 10.1016/j.apradiso.2014.07.008.

[81] J. W. Meadows. “Excitation Functions for Proton-Induced Reactions with Copper”. In: *Phys. Rev.* 91 (4 1953), pp. 885–889. DOI: 10.1103/PhysRev.91.885.

[82] G. A. Brinkman et al. “Nickel and copper foils as monitors for cyclotron beam intensities”. In: *Radiochemical and Radioanalytical Letters* 28.1 (1977), pp. 9–19.

[83] R. Collé et al. “^{65}Cu(p,pn)^{64}Cu excitation function in the energy range 13–25 MeV”. In: *Journal of Inorganic and Nuclear Chemistry* 38.1 (1976), pp. 23–25. ISSN: 0022-1902. DOI: https://doi.org/10.1016/0022-1902(76)80042-5.

[84] G. Dellepiane et al. “Cross-section measurement for an optimized ^{61}Cu production at an 18 MeV medical cyclotron from natural Zn and enriched ^{64}Zn solid targets”. In: *Applied Radiation and Isotopes* 190 (2022), p. 110466. DOI: 10.1016/j.apradiso.2022.110466.

[85] N. Zandi. “^{61}Cu/^{67}Cu theranostic pair production, chemical separation and radiolabeling”. PhD thesis. University of Bern, Switzerland, 2021.

[86] H. Zhang et al. “Positron Emission Tomography of Human Hepatocellular Carcinoma Xenografts in Mice Using Copper (II)-64 Chloride as a Tracer”. In: *Academic Radiology* 18 (12 2011), pp. 1561–1568. DOI: 10.1016/j.acra.2011.08.006.

[87] C. Qin et al. “Theranostics of Malignant Melanoma with $^{64}CuCl_2$”. In: *Journal of Nuclear Medicine* 55.5 (2014), pp. 812–817. ISSN: 0161-5505. DOI: 10.2967/jnumed.113.133850.

[88] R. Chakravarty et al. “$^{64}Cu^{2+}$ Ions as PET Probe: An Emerging Paradigm in Molecular Imaging of Cancer”. In: *Molecular Pharmaceutics* 13 (11 2016), pp. 3601–3612. DOI: 10.1021/acs.molpharmaceut.6b00582.

[89] E. Capasso et al. “Role of $^{64}CuCl_2$ PET/CT in staging of prostate cancer”. In: *Ann Nucl Med* 29.6 (2015), pp. 482–488. DOI: 10.1007/s12149-015-0968-4.

[90] M. A. Avila-Rodriguez et al. “Biodistribution and radiation dosimetry of [^{64}Cu]copper dichloride: first-in-human study in healthy volunteers”. In: *EJNMMI Research* 7.1 (2017), pp. 98–104. DOI: 10.1186/s13550-017-0346-4.

[91] P. J. Aggett. “An overview of the metabolism of copper”. In: *Eur J Med Res* 4 (1999), pp. 214–216.

[92] J. L. Humm et al. “Radium-223 in the Treatment of Osteoblastic Metastases: A Critical Clinical Review”. In: *International Journal of Radiation Oncology*Biology*Physics* 91.5 (2015), pp. 898–906. ISSN: 0360-3016. DOI: 10.1016/j.ijrobp.2014.12.061.

[93] G. Dellepiane et al. “Alternative routes for ^{64}Cu production using an 18 MeV medical cyclotron in view of theranostic applications”. In: *Applied Radiation and Isotopes* 191 (2023), p. 110518. DOI: 10.1016/j.apradiso.2022.110518.

[94] C. Ferrari et al. “Copper-64 Dichloride as Theranostic Agent for Glioblastoma Multiforme: A Preclinical Study”. In: *BioMed Research International* 2015 (2015), pp. 1–6. DOI: 10.1155/2015/129764.

[95] L. Mou et al. “^{67}Cu Production Capabilities: A Mini Review”. In: *Molecules* 27 (5 2022), p. 1501. DOI: 10.3390/molecules27051501.

[96] G. Dellepiane et al. “Study of ^{67}Cu optimised production based on cross-section measurements of ^{67}Cu and ^{64}Cu using an 18 MeV medical cyclotron”. In: *Applied Radiation and Isotopes* 195 (2023), p. 110737. DOI: 10.1016/j.apradiso.2023.110737.

[97] IAEA. *Gallium-68 Cyclotron Production*. TECDOC Series 1863. Vienna, 2019. ISBN: 978-92-0-100819-0.

[98] F. Alves et al. “Cyclotron production of ^{68}Ga for human use from liquid targets: From theory to practice”. In: *AIP Conference Proceedings 1845* 1 (2017), p. 020001. DOI: 10.1063/1.4983532.

[99] S. Riga et al. “Production of ^{68}Ga with a General Electric PETtrace cyclotron by liquid target”. In: *Physica Medica* 55 (2018), pp. 116–126. DOI: 10.1016/j.ejmp.2018.10.018.

[100] B. J. B. Nelson et al. “Taking cyclotron ^{68}Ga production to the next level: Expeditious solid target production of ^{68}Ga for preparation of radiotracers”. In: *Nuclear Medicine and Biology* 80-81 (2020), pp. 24–31. DOI: 10.1016/j.nucmedbio.2020.01.005.

[101] A. H. Alnahwi et al. “Automated radiosynthesis of ^{68}Ga for large-scale routine production using ^{68}Zn pressed target”. In: *Applied Radiation and Isotopes* 156 (2020), p. 109014. DOI: 10.1016/j.apradiso.2019.109014.

[102] F. Szelecsényi et al. “Evaluated cross section and thick target yield data bases of Zn + p processes for practical applications”. In: *Applied Radiation and Isotopes* 49.8 (1998), pp. 1005 –1032. DOI: 10.1016/S0969-8043(97)10103-8.

[103] F. Szelecsényi et al. “Investigation of direct production of ^{68}Ga with low energy multiparticle accelerator”. In: *Radiochimica Acta* 100.1 (2012), pp. 5 –11. DOI: 10.1524/ract.2011.1896.

[104] "Gallium (^{68}Ga) Chloride (accelerator-produced) solution for radiolabelling". In: *European Pharmacopoeia* 10.3 (2021), pp. 4864–4865.

[105] S. Braccini et al. "Optimization of ^{68}Ga production at an 18 MeV medical cyclotron with solid targets by means of cross-section measurement of ^{66}Ga, ^{67}Ga and ^{68}Ga". In: *Applied Radiation and Isotopes* (2022), p. 110252. ISSN: 0969-8043. DOI: https://doi.org/10.1016/j.apradiso.2022.110252.

[106] A. Gottschalk. "Technetium-99m in Clinical Nuclear Medicine". In: *Annual Review of Medicine* 20.1 (1969), pp. 131–139. DOI: 10.1146/annurev.me.20.020169.001023.

[107] T. J. Ruth. "The Shortage of Technetium-99m and Possible Solutions". In: *Annual Review of Nuclear and Particle Science* 70.1 (2020), pp. 77–94. DOI: 10.1146/annurev-nucl-032020-021829.

[108] J. E. Beaver and H. B. Hupf. "Production of ^{99m}Tc on a Medical Cyclotron: A Feasibility Study". In: *Journal of Nuclear Medicine* 12.11 (1971), pp. 739–741. ISSN: 0161-5505.

[109] *Cyclotron Based Production of Technetium-99m*. Radioisotopes and Radiopharmaceuticals Reports 2. Vienna: INTERNATIONAL ATOMIC ENERGY AGENCY, 2017. ISBN: 978-92-0-102916-4. URL: https://www.iaea.org/publications/10990/cyclotron-based-production-of-technetium-99m.

[110] P. Martini et al. "In-house cyclotron production of high-purity Tc-99m and Tc-99m radiopharmaceuticals". In: *Applied Radiation and Isotopes* 139 (2018), pp. 325–331. DOI: 10.1016/j.apradiso.2018.05.033.

[111] B. M. Bondar et al. "Determination of the experimental yield of ^{99m}Tc in (p,2n) nuclear reaction on enriched 100Mo sample with application of 11 MeV medical cyclotron". In: *Applied Radiation and Isotopes* 189 (2022), p. 110431. DOI: 10.1016/j.apradiso.2022.110431.

[112] M. C. Lagunas-Solar et al. "An update on the direct production of ^{99m}Tc with proton beams and enriched ^{100}Mo targets". In: *Transactions of the American Nuclear Society* 74.137 (Dec. 1996).

[113] B. Scholten et al. "Excitation functions for the cyclotron production of ^{99m}Tc and ^{99}Mo". In: *Applied Radiation and Isotopes* 51.1 (1999), pp. 69–80. DOI: 10.1016/S0969-8043(98)00153-5.

[114] S. Takács et al. "Evaluation of proton induced reactions on 100Mo: New cross sections for production of ^{99m}Tc and ^{99}Mo". In: *Journal of Radioanalytical and Nuclear Chemistry* 257 (1 2003), pp. 195–201.

[115] M. U. Khandaker et al. “Measurement of cross-sections for the (p,xn) reactions in natural molybdenum”. In: *Nuclear Instruments and Methods in Physics Research Section B: Beam Interactions with Materials and Atoms* 262.2 (2007), pp. 171–181. DOI: 10.1016/j.nimb.2007.05.028.

[116] M. B. Challan et al. “Thin target yields and Empire-II predictions on the accelerator production of technetium-99m”. In: *Nuclear and Radiation Physics* 2 (1 2007).

[117] O. Lebeda and M.Pruszyński. “New measurement of excitation functions for (p,x) reactions on ^{nat}Mo with special regard to the formation of ^{95m}Tc, $^{96m+g}$Tc, ^{99m}Tc and ^{99}Mo”. In: *Applied Radiation and Isotopes* 68.12 (2010), pp. 2355–2365. DOI: 10.1016/j.apradiso.2010.05.011.

[118] A. Alharbi et al. *Medical Radioisotopes Production: A Comprehensive Cross-Section Study for the Production of Mo and Tc Radioisotopes Via Proton Induced Nuclear Reactions on ^{nat}Mo*. IntechOpen, Nov. 2011. ISBN: 978-953-307-748-2. DOI: 10.5772/20598.

[119] K. Gagnon et al. “Cyclotron production of ^{99m}Tc: Experimental measurement of the ^{100}Mo(p,x)^{99}Mo, ^{99m}Tc and ^{99g}Tc excitation functions from 8 to 18 MeV”. In: *Nuclear Medicine and Biology* 38.6 (2011), pp. 907–916. DOI: 10.1016/j.nucmedbio.2011.02.010.

[120] F. Tárkányi et al. “Investigation of activation cross-sections of proton induced nuclear reactions on ^{nat}Mo up to 40 MeV: New data and evaluation”. In: *Nuclear Instruments and Methods in Physics Research Section B: Beam Interactions with Materials and Atoms* 280 (2012), pp. 45–73. DOI: 10.1016/j.nimb.2012.02.029.

[121] S. Manenti et al. “The excitation functions of ^{100}Mo(p,x)^{99}Mo and ^{100}Mo(p,2n)^{99m}Tc”. In: *Applied Radiation and Isotopes* 94 (2014), pp. 344–348. DOI: 10.1016/j.apradiso.2014.09.010.

[122] S. Takács et al. “Reexamination of cross sections of the ^{100}Mo(p,2n)^{99m}Tc reaction”. In: *Nuclear Instruments and Methods in Physics Research Section B: Beam Interactions with Materials and Atoms* 347 (2015), pp. 26–38. DOI: 10.1016/j.nimb.2015.01.056.

[123] E. Lamere et al. “Proton-induced reactions on molybdenum”. In: *Physical Review C* 100.3 (2019), p. 034614. DOI: 10.1103/PhysRevC.100.034614.

[124] A. A. Ahmed et al. “Study of ^{99}Mo and long-lived impurities produced through (p,x) reactions in the ^{nat}Mo”. In: *Radiation Physics and Chemistry* 190 (2022), p. 109774. DOI: 10.1016/j.radphyschem.2021.109774.

[125] C. Müller et al. “Future prospects for SPECT imaging using the radiolanthanide terbium-155 — production and preclinical evaluation in tumor-bearing mice”. In: *Nuclear Medicine and Biology* 41 (2014), e58–e65. ISSN: 0969-8051. DOI: 10.1016/j.nucmedbio.2013.11.002.

[126] C. Vermeulen et al. “Cross sections of proton-induced reactions on ^{nat}Gd with special emphasis on the production possibilities of ^{152}Tb and ^{155}Tb”. In: *Nuclear Instruments and Methods in Physics Research B* 275 (2012), pp. 24–32. DOI: 10.1016/j.nimb.2011.12.064.

[127] C. Müller et al. “A Unique Matched Quadruplet of Terbium Radioisotopes for PET and SPECT and for α^- and β^--Radionuclide Therapy: An In Vivo Proof-of-Concept Study with a New Receptor-Targeted Folate Derivative”. In: *Journal of Nuclear Medicine* 53 (2012), pp. 1951–1959. DOI: 10.2967/jnumed.112.107540.

[128] Y. Wang. “Development of enriched gadolinium target for cross section measurement and future production of terbium for nuclear medicine”. PhD thesis. University of Nantes, France, 2022.

[129] P. P. Dmitriev et al. “Production of ^{155}Tb for nuclear medicine by reactions ^{155}Gd(p,n), ^{156}Gd(p,2n), ^{155}Gd(d2n)”. In: *Atomnaya Ehnergiya* 66 (1989), pp. 419–421. ISSN: 6.

[130] G. Dellepiane et al. “Cross section measurement of terbium radioisotopes for an optimized ^{155}Tb production with an 18 MeV medical PET cyclotron”. In: *Applied Radiation and Isotopes* 184 (2022), p. 110175. DOI: 10.1016/j.apradiso.2022.110175.

[131] C. Favaretto. “Development of terbium radioisotopes towards clinical theragnostics applications in nuclear medicine”. PhD thesis. ETH Zürich, Switzerland, 2022.

[132] F. Borgna et al. “Simultaneous Visualization of ^{161}Tb- and ^{177}Lu-Labeled Somatostatin Analogues Using Dual-Isotope SPECT Imaging”. In: *Pharmaceutics* 13.4 (2021), pp. 536–549. DOI: 10.3390/pharmaceutics13040536.

[133] C. Favaretto et al. “Cyclotron production and radiochemical purification of terbium-155 for SPECT imaging”. In: *EJNMMI Radiopharmacy and Chemistry* 6 (2021), p. 37. DOI: 10.1186/s41181-021-00153-w.

[134] L. Yasui et al. “Relative biological effectiveness of accumulated ^{125}IdU and ^{125}I-estrogen decays in estrogen receptor-expressing MCF-7 human breast cancer cells”. In: *Radiat Res* 155.2 (2001), pp. 328–334. DOI: 10.1667/0033-7587.

[135] A. I. Kassis. “The amazing world of auger electrons”. In: *Int J Radiat Biol* 80.11-12 (2004), pp. 789–803. DOI: 10.1080/09553000400017663.

[136] S. Cotton. "Coordination Chemistry of the Lanthanides". In: *Lanthanide and Actinide Chemistry*. John Wiley Sons, Ltd, 2006. Chap. 4, pp. 35–60. ISBN: 9780470010082. DOI: https://doi.org/10.1002/0470010088.ch4.

[137] A. W. E. Sadler et al. "Cutting edge rare earth radiometals: prospects for cancer theranostics". In: *EJNMMI Radiopharm Chem* 7.1 (2022), p. 21. DOI: 10.1186/s41181-022-00173-0.

[138] G. J. Beyer et al. "The Auger-electron emitter ^{165}Er: excitation function of the ^{165}Ho(p, n)^{165}Er process". In: *Radiochimica Acta* 92.4-6 (2004), pp. 219–222. DOI: 10.4236/jmp.2010.14033.

[139] F. Tárkányi et al. "Study of activation cross-sections of deuteron induced reactions on erbium: Production of radioisotopes for practical applications". In: *Nuclear Instruments and Methods in Physics Research Section B: Beam Interactions with Materials and Atoms* 259.2 (2007), pp. 829–835. DOI: 10.1016/j.nimb.2007.01.287.

[140] F. Tárkányi et al. "Study of activation cross sections of proton induced reactions on erbium for practical applications". In: *Nuclear Instruments and Methods in Physics Research Section B: Beam Interactions with Materials and Atoms* 266.22 (2008), pp. 4872–4876. DOI: 10.1016/j.nimb.2008.08.005.

[141] F. Tárkányi et al. "Experimental study of the ^{165}Ho(p,n) nuclear reaction for production of the therapeutic radioisotope ^{165}Er". In: *Nuclear Instruments and Methods in Physics Research Section B: Beam Interactions with Materials and Atoms* 266.15 (2008), pp. 3346–3352. DOI: 10.1016/j.nimb.2008.05.005.

[142] F. Tárkányi et al. "Experimental study of the ^{165}Ho(d,2n) and ^{165}Ho(d,p) nuclear reactions up to 20 MeV for production of the therapeutic radioisotopes ^{165}Er and ^{166g}Ho". In: *Nuclear Instruments and Methods in Physics Research Section B: Beam Interactions with Materials and Atoms* 266.16 (2008), pp. 3529–3534. DOI: 10.1016/j.nimb.2008.05.123.

[143] F. Tárkányi et al. "Investigation of production of the therapeutic radioisotope ^{165}Er by proton induced reactions on erbium in comparison with other production routes". In: *Applied Radiation and Isotopes* 67.2 (2009), pp. 243–247. DOI: 10.1016/j.apradiso.2008.10.006.

[144] M. Sadeghi et al. "Nuclear Model Calculations on the Production of Auger Emitter ^{165}Er for Targeted Radionuclide Therapy". In: *Journal of Modern Physics* 1.4 (2010), pp. 217–225. DOI: 10.4236/jmp.2010.14033.

[145] N. Zandi et al. "Evaluation of the cyclotron production of ^{165}Er by different reactions". In: *Journal of Radioanalytical and Nuclear Chemistry* 295 (2 2013), pp. 923–928. DOI: 10.1007/s10967-012-2116-0.

[146] A. Hermanne et al. “Deuteron induced reactions on Ho and La: Experimental excitation functions and comparison with code results”. In: *Nuclear Instruments and Methods in Physics Research Section B: Beam Interactions with Materials and Atoms* 311 (2013), pp. 102–111. DOI: 10.1016/j.nimb.2013.06.014.

[147] N. Gracheva et al. “^{165}Er: A new candidate for Auger electron therapy and its possible cyclotron production from natural holmium targets”. In: *Applied Radiation and Isotopes* 159 (2020), p. 109079. DOI: 10.1016/j.apradiso.2020.109079.

[148] F. Tárkányi et al. “Study of excitation functions of alpha-particle induced nuclear reactions on holmium for ^{167}Tm production”. In: *Applied Radiation and Isotopes* 68.3 (2010), pp. 404–411. DOI: 10.1016/j.apradiso.2009.11.043.

[149] A. Hermanne et al. “Cross sections for production of longer lived ^{170,168,167}Tm in 16 MeV proton irradiation of ^{nat}Er”. In: *Nuclear Instruments and Methods in Physics Research Section B: Beam Interactions with Materials and Atoms* 269.7 (2011), pp. 695–699. DOI: 10.1016/j.nimb.2011.01.130.

[150] G. Dellepiane et al. “Cross-section measurement of thulium radioisotopes with an 18 MeV medical PET cyclotron for an optimized ^{165}Er production”. In: *to be submitted to Applied Radiation and Isotopes* (2023).

[151] D. Filosofov et al. “Potent candidates for Targeted Auger Therapy: Production and radiochemical considerations”. In: *Nuclear Medicine and Biology* 94 (2021), pp. 1–19. DOI: 10.1016/j.nucmedbio.2020.12.001.

[152] R. Chandra et al. “Evaluation of ^{167}Tm HEDTA as a bone scanning agent in humans and its comparison with ^{18}F”. In: *The British Journal of Radiology* 47.553 (1974), pp. 51–53. DOI: 10.1259/0007-1285-47-553-51.

[153] A. Ando et al. “Affinity of ^{167}Tm-citrate for tumor and liver tissue”. In: *European Journal of Nuclear Medicine* 8 (10 1983), pp. 440–446. DOI: doi.org/10.1007/BF00252943.

[154] H. Uusijärvi et al. “Electron- and positron-emitting radiolanthanides for therapy: aspects of dosimetry and production”. In: *Journal of Nuclear Medicine* 47.5 (2006), pp. 807–814.

[155] H. Uusijärvi et al. “Dosimetric characterization of radionuclides for systemic tumor therapy: influence of particle range, photon emission, and subcellular distribution”. In: *Medical Physics* 33.9 (2006), pp. 3260–3269. DOI: 10.1118/1.2229428.

[156] G. J. Beyer et al. “Comparative kinetic studies of simultaneously injected ^{167}Tm- and ^{67}Ga-Citrate in Normal and Tumour bearing mice”. In: *The International Journal of Applied Radiation and Isotopes* 29.11 (1978), pp. 673–681. DOI: 10.1016/0020-708X(78)90105-9.

[157] Y. Homma et al. “Cyclotron production of ^{167}Tm from natural erbium and natural holmium”. In: *The International Journal of Applied Radiation and Isotopes* 31.8 (1980), pp. 505–508. DOI: 10.1016/0020-708X(80)90314-2.

[158] F. Tárkányi et al. “Experimental study of the excitation functions of proton induced nuclear reactions on 167Er for production of medically relevant 167Tm”. In: *Applied Radiation and Isotopes* 68.2 (2010), pp. 250–255. DOI: 10.1016/j.apradiso.2009.10.043.

[159] A. Hermanne et al. “High yield production of the medical radioisotope ^{167}Tm by the ^{167}Er(d,2n) reaction”. In: *Applied Radiation and Isotopes* 69.2 (2011), pp. 475–481. DOI: 10.1016/j.apradiso.2010.10.003.

[160] R. A. Aliev et al. “Production of medical radioisotope ^{167}Tm by photonuclear reactions on natural ytterbium”. In: *Nuclear Instruments and Methods in Physics Research Section B: Beam Interactions with Materials and Atoms* 508 (2021), pp. 19–23. DOI: 10.1016/j.nimb.2021.10.004.

[161] R. Heinke et al. “Efficient Production of High Specific Activity Thulium-167 at Paul Scherrer Institute and CERN-MEDICIS”. In: *Frontiers in Medicine* 8 (2021). DOI: 10.3389/fmed.2021.712374.

Conclusions and Outlook

The purpose of my PhD work was to investigate theranostic and non-standard radionuclides in view of their application in modern nuclear medicine, by means of instruments and methods derived from nuclear and particle physics. These novel radioisotopes, in fact, are often obtained by irradiating expensive isotopically enriched powders, making the irradiation procedure challenging. In addition, the coproduction of radioisotopic impurities leads to the need for precisely knowing the nuclear cross sections involved.

The experiments reported in this thesis were carried out at the Bern medical cyclotron laboratory, where an 18 MeV cyclotron is in operation together with a Beam Transport Line (BTL) and a Solid Target Station (STS) for research purposes.

The BTL, together with the instrumentation and the methodologies developed by our group, allows an almost complete control of the beam characteristics, enabling the production cross section measurement as a function of the proton input energy.

Because more than one reaction often participates in radionuclide production, I developed a method to disentangle the different nuclear contributions. This method, based on solving linear systems of equations, involves the measurement of production cross sections from as many materials with different isotopic percentages as there are reactions contributing to the radionuclide production.

During my PhD I measured the cross sections of many nuclear reactions, namely:
^{47}Ti(p,αn)^{43}Sc, ^{47}Ti(p,α)^{44}Sc, ^{47}Ti(p,α)^{44m}Sc, ^{49}Ti(p,α)^{46}Sc, ^{50}Ti(p,α)^{47}Sc, ^{64}Zn(p,αn)^{60}Cu, ^{64}Zn(p,α)^{61}Cu, ^{67}Zn(p,α)^{64}Cu, ^{68}Zn(p,αn)^{64}Cu, ^{65}Cu(p,pn)^{64}Cu, ^{70}Zn(p,α)^{67}Cu, ^{68}Zn(p,n)^{68}Ga, ^{67}Zn(p,n)^{67}Ga, ^{68}Zn(p,2n)^{67}Ga, ^{66}Zn(p,n)^{66}Ga, ^{67}Zn(p,2n)^{66}Ga, ^{94}Mo(p,2n)^{93}Tc, ^{94}Mo(p,2n)^{93m}Tc, ^{100}Mo(p,2n)^{99m}Tc,

^{100}Mo(p,x)^{99}Mo, ^{154}Gd(p,2n)^{153}Tb, ^{154}Gd(p,n)^{154}Tb, ^{155}Gd(p,2n)^{154}Tb, ^{155}Gd(p,n)^{155}Tb, ^{156}Gd(p,2n)^{155}Tb, ^{156}Gd(p,n)^{156}Tb, ^{157}Gd(p,2n)^{156}Tb, ^{164}Er(p,γ)^{165}Tm, ^{166}Er(p,2n)^{165}Tm, ^{166}Er(p,n)^{166}Tm, ^{167}Er(p,2n)^{166}Tm, ^{166}Er(p,γ)^{167}Tm, ^{167}Er(p,n)^{167}Tm, ^{168}Er(p,2n)^{167}Er, ^{167}Er(p,γ)^{168}Tm, ^{168}Er(p,n)^{168}Tm, ^{170}Er(p,3n)^{168}Tm and ^{170}Er(p,n)^{170}Tm.

For some of these reactions there were no experimental data available in the literature in the energy range considered. My work has thus contributed substantially to enhance the knowledge of nuclear data needed for the production of novel radionuclides for medical applications.

On the basis of the obtained results, I determined the irradiation parameters that optimize the production of ^{68}Ga, ^{44}Sc, ^{47}Sc, ^{61}Cu, ^{64}Cu, ^{67}Cu, ^{155}Tb, ^{165}Tm and ^{167}Tm by means of solid targets. These predictions were confirmed by performing several production tests with the STS.

In particular, the possibility of reproducible production of ^{155}Tb with a medical cyclotron in quantity and quality suitable for preclinical applications was demonstrated for the first time. The radiochemical separation procedures developed at PSI yielded a [^{155}Tb]$TbCl_3$ solution with high chemical purity, ensuring radiolabelling of the tumour-targeting molecules. The resulting ^{155}Tb-DOTATOC was successfully used for an in vivo SPECT/CT imaging study in tumour-bearing mice, proving the applicability of cyclotron-produced ^{155}Tb for diagnostic purposes.

For productions in the STS to be successful, it is necessary to have a good understanding of the characteristics of the extracted beam, namely energy, position and shape. In this regard, I played an important role in the development of a new method to measure the beam energy, based on the stacked-foil technique.
Natural Ti foils, separated by Nb degraders, were inserted into a special version of the coin and irradiated to exploit the ^{nat}Ti(p,x)^{48}V monitor reaction. By measuring the activity produced by means of γ spectrometry and comparing them with the expected values, the beam energy could be determined for several stripper angles.

To improve the irradiation procedure using the novel Automatic Focusing System (AFS) developed by our group, I contributed to fine-tune the alignment of the STS. I also contributed to the setting of the stripper angle and of the Mini-PET Beamline (MBL) parameters that maximize the current on target. The effective current hitting the 6-mm-diameter pellet was determined by using a gafchromic film.

My work suggested some further improvements. The beam extraction depends on the position of the sources and strippers within the cyclotron and can slightly change after each maintenance intervention. In order to quickly restore the optimal alignment of the system, a motorized bellow has been recently installed to change the STS position with respect to the AFS horizontally and vertically with a submillimetric precision. This will make it possible to fully exploit the beam focusing and steering capabilities of the AFS, optimizing the current on the target. Furthermore, I believe that a Monte Carlo simulation of the beam configuration would help to assess the limits of the target capsule named "coin", that I contributed to develop. A new geometry of the two magnetic parts could also be evaluated, featuring ribs to form a locally inclined surface in order to take full advantage of the cooling system.
These modifications will enable the irradiation of targets with higher currents, making it possible to achieve larger radioisotope activities for theranostic applications in nuclear medicine.

The developments I performed and the results I obtained in the framework of this PhD thesis are at the basis of future studies and projects, some of them already ongoing. My achievements contributed to pave the way towards the implementation of theranostics in nuclear personalized medicine.

Appendix
Unpublished cross section Data

Scandium radioisotopes

E [MeV]	σ [mbarn]	E [MeV]	σ [mbarn]
7.7 ± 0.4	No Signal	14.5 ± 0.4	No Signal
8.7 ± 0.4	No Signal	15.8 ± 0.4	No Signal
9.7 ± 0.4	No Signal	17.1 ± 0.4	0.15 ± 0.09
11.5 ± 0.4	No Signal	18.2 ± 0.4	1.0 ± 0.2
13.0 ± 0.4	No Signal		

Table 3.27: ^{47}Ti(p,αn)^{43}Sc nuclear cross section data.

E [MeV]	σ [mbarn]	E [MeV]	σ [mbarn]
7.7 ± 0.4	2.2 ± 0.2	14.5 ± 0.4	46 ± 4
8.7 ± 0.4	7.2 ± 0.6	15.8 ± 0.4	48 ± 3
9.7 ± 0.4	15 ± 1	17.1 ± 0.4	50 ± 2
11.5 ± 0.4	28 ± 2	18.2 ± 0.4	45 ± 2
13.0 ± 0.4	37 ± 3		

Table 3.28: ^{47}Ti(p,α)^{44}Sc nuclear cross section data.

E [MeV]	σ [mbarn]	E [MeV]	σ [mbarn]
7.7 ± 0.4	No Signal	14.5 ± 0.4	12 ± 1
8.7 ± 0.4	0.8 ± 0.2	15.8 ± 0.4	12.9 ± 0.8
9.7 ± 0.4	1.9 ± 0.3	17.1 ± 0.4	16.0 ± 0.7
11.5 ± 0.4	4.4 ± 0.4	18.2 ± 0.4	17.5 ± 0.7
13.0 ± 0.4	8.2 ± 0.8		

Table 3.29: ^{47}Ti(p,α)^{44m}Sc nuclear cross section data.

E [MeV]	σ [mbarn]	E [MeV]	σ [mbarn]
7.7 ± 0.4	No Signal	14.5 ± 0.4	1.6 ± 0.4
8.7 ± 0.4	No Signal	15.8 ± 0.4	3.5 ± 0.6
9.7 ± 0.4	No Signal	17.1 ± 0.4	8.5 ± 0.5
11.5 ± 0.4	No Signal	18.2 ± 0.4	18 ± 1
13.0 ± 0.4	No Signal		

Table 3.30: ^{47}Ti(p,2p)^{46}Sc nuclear cross section data.

E [MeV]	σ [mbarn]	E [MeV]	σ [mbarn]
7.7 ± 0.4	No Signal	14.5 ± 0.4	No Signal
8.7 ± 0.4	No Signal	15.8 ± 0.4	No Signal
9.7 ± 0.4	No Signal	17.1 ± 0.4	2 ± 1
11.5 ± 0.4	No Signal	18.2 ± 0.4	3.7 ± 0.5
13.0 ± 0.4	No Signal		

Table 3.31: ^{48}Ti(p,2p)^{47}Sc nuclear cross section data.

Technetium-99m

E [MeV]	σ [mbarn]	E [MeV]	σ [mbarn]
8.2 ± 0.4	No Signal	14.5 ± 0.4	57 ± 11
9.7 ± 0.4	No Signal	15.8 ± 0.4	282 ± 24
11.5 ± 0.4	No Signal	17.1 ± 0.4	361 ± 25
13.0 ± 0.4	No Signal	18.2 ± 0.4	447 ± 27

Table 3.32: ^{94}Mo(p,2n)^{93}Tc nuclear cross section data.

E [MeV]	σ [mbarn]	E [MeV]	σ [mbarn]
8.2 ± 0.4	No Signal	14.5 ± 0.4	14 ± 5
9.7 ± 0.4	No Signal	15.8 ± 0.4	60 ± 5
11.5 ± 0.4	No Signal	17.1 ± 0.4	107 ± 7
13.0 ± 0.4	No Signal	18.2 ± 0.4	127 ± 8

Table 3.33: ^{94}Mo(p,2n)^{93m}Tc nuclear cross section data.

E [MeV]	σ [mbarn]	E [MeV]	σ [mbarn]
8.2 ± 0.4	29 ± 2	14.5 ± 0.4	223 ± 13
9.7 ± 0.4	112 ± 6	15.8 ± 0.4	231 ± 14
11.5 ± 0.4	193 ± 11	17.1 ± 0.4	221 ± 11
13.0 ± 0.4	214 ± 13	18.2 ± 0.4	222 ± 12

Table 3.34: ^{100}Mo(p,2n)^{99m}Tc nuclear cross section data.

E [MeV]	σ [mbarn]	E [MeV]	σ [mbarn]
8.2 ± 0.4	No Signal	14.5 ± 0.4	24 ± 3
9.7 ± 0.4	No Signal	15.8 ± 0.4	39 ± 3
11.5 ± 0.4	2.4 ± 0.4	17.1 ± 0.4	60 ± 4
13.0 ± 0.4	10 ± 3	18.2 ± 0.4	75 ± 5

Table 3.35: ^{100}Mo(p,x)^{99}Mo nuclear cross section data.

Terbium-155

E [MeV]	σ [mbarn]	E [MeV]	σ [mbarn]
11.9 ± 0.4	181 ± 45	15.8 ± 0.4	648 ± 51
12.1 ± 0.4	194 ± 52	17.1 ± 0.4	901 ± 72
13.0 ± 0.4	358 ± 33	18.2 ± 0.4	1098 ± 118
14.5 ± 0.4	528 ± 44		

Table 3.36: ^{154}Gd(p,2n)^{153}Tb nuclear cross section data.

E [MeV]	σ [mbarn]	E [MeV]	σ [mbarn]
11.9 ± 0.4	No Signal	15.8 ± 0.4	No Signal
12.1 ± 0.4	No Signal	17.1 ± 0.4	No Signal
13.0 ± 0.4	No Signal	18.2 ± 0.4	5 ± 2
14.5 ± 0.4	No Signal		

Table 3.37: ^{155}Gd(p,3n)^{153}Tb nuclear cross section data.

E [MeV]	σ [mbarn]	E [MeV]	σ [mbarn]
7.7 ± 0.4	34 ± 14	14.5 ± 0.4	No Signal
10.2 ± 0.4	189 ± 66	15.5 ± 0.4	No Signal
11.5 ± 0.4	135 ± 33	15.8 ± 0.4	No Signal
12.1 ± 0.4	No Signal	17.1 ± 0.4	No Signal
13.0 ± 0.4	No Signal	18.2 ± 0.4	No Signal

Table 3.38: ^{154}Gd(p,n)^{154}Tb nuclear cross section data.

E [MeV]	σ [mbarn]	E [MeV]	σ [mbarn]
7.7 ± 0.4	No Signal	14.5 ± 0.4	183 ± 26
10.2 ± 0.4	No Signal	15.5 ± 0.4	190 ± 12
11.5 ± 0.4	24 ± 4	15.8 ± 0.4	209 ± 24
12.1 ± 0.4	68 ± 4	17.1 ± 0.4	205 ± 14
13.0 ± 0.4	108 ± 18	18.2 ± 0.4	243 ± 15

Table 3.39: ^{155}Gd(p,2n)^{154}Tb nuclear cross section data.

E [MeV]	σ [mbarn]	E [MeV]	σ [mbarn]
5.8 ± 0.4	6 ± 2	8.7 ± 0.4	200 ± 40
6.2 ± 0.4	14 ± 4	9.0 ± 0.4	101 ± 9
6.8 ± 0.4	22 ± 4	9.7 ± 0.4	134 ± 22
7.1 ± 0.4	25 ± 2	10.0 ± 0.4	260 ± 20
7.7 ± 0.4	56 ± 8	10.2 ± 0.4	No Signal
7.9 ± 0.4	100 ± 20	10.8 ± 0.4	No Signal

Table 3.40: ^{154}Gd(p,n)^{154m1}Tb nuclear cross section data.

E [MeV]	σ [mbarn]	E [MeV]	σ [mbarn]
9.7 ± 0.4	No Signal	12.7 ± 0.4	186 ± 32
10.0 ± 0.4	No Signal	13.0 ± 0.4	247 ± 28
10.2 ± 0.4	1.6 ± 0.3	14.0 ± 0.4	356 ± 57
10.8 ± 0.4	5 ± 1	14.5 ± 0.4	381 ± 39
11.5 ± 0.4	47 ± 6	15.5 ± 0.4	452 ± 19
11.9 ± 0.4	71 ± 8	15.8 ± 0.4	475 ± 46
12.1 ± 0.4	104 ± 5	17.1 ± 0.4	557 ± 42
12.3 ± 0.4	126 ± 23	18.2 ± 0.4	721 ± 31
12.5 ± 0.4	203 ± 34		

Table 3.41: ^{155}Gd(p,2n)^{154m1}Tb nuclear cross section data.

E [MeV]	σ [mbarn]	E [MeV]	σ [mbarn]
5.1 ± 0.4	2.7 ± 0.7	10.0 ± 0.4	350 ± 22
5.8 ± 0.4	4.5 ± 0.5	10.8 ± 0.4	431 ± 38
6.2 ± 0.4	13.1 ± 0.8	11.5 ± 0.4	428 ± 39
6.8 ± 0.4	25 ± 2	11.9 ± 0.4	418 ± 39
7.1 ± 0.4	71 ± 5	12.1 ± 0.4	351 ± 23
7.4 ± 0.4	86 ± 13	13.0 ± 0.4	194 ± 31
7.7 ± 0.4	90 ± 5	14.5 ± 0.4	154 ± 25
7.9 ± 0.4	108 ± 7	15.5 ± 0.4	130 ± 6
8.7 ± 0.4	174 ± 12	15.8 ± 0.4	102 ± 13
9.0 ± 0.4	182 ± 14	17.1 ± 0.4	76 ± 5
9.3 ± 0.4	242 ± 23	18.2 ± 0.4	72 ± 5
9.7 ± 0.4	280 ± 18		

Table 3.42: ^{155}Gd(p,n)^{155}Tb nuclear cross section data.

E [MeV]	σ [mbarn]	E [MeV]	σ [mbarn]
10.8 ± 0.4	No Signal	14.5 ± 0.4	616 ± 53
11.5 ± 0.4	153 ± 16	15.5 ± 0.4	820 ± 42
11.9 ± 0.4	218 ± 19	15.8 ± 0.4	872 ± 76
12.1 ± 0.4	281 ± 15	17.1 ± 0.4	943 ± 78
13.0 ± 0.4	439 ± 40	18.2 ± 0.4	1035 ± 65

Table 3.43: ^{156}Gd(p,2n)^{155}Tb nuclear cross section data.

E [MeV]	σ [mbarn]	E [MeV]	σ [mbarn]
10.8 ± 0.4	No Signal	14.5 ± 0.4	No Signal
11.5 ± 0.4	No Signal	15.5 ± 0.4	No Signal
11.9 ± 0.4	No Signal	15.8 ± 0.4	No Signal
12.1 ± 0.4	No Signal	17.1 ± 0.4	No Signal
13.0 ± 0.4	No Signal	18.2 ± 0.4	161.5 ± 0.4

Table 3.44: ^{157}Gd(p,3n)^{155}Tb nuclear cross section data.

E [MeV]	σ [mbarn]	E [MeV]	σ [mbarn]
5.1 ± 0.4	1.3 ± 0.2	9.7 ± 0.4	211 ± 15
5.8 ± 0.4	5.8 ± 0.4	10.0 ± 0.4	289 ± 10
6.2 ± 0.4	17 ± 1	12.1 ± 0.4	241 ± 11
7.1 ± 0.4	54 ± 5	13.0 ± 0.4	209 ± 24
7.4 ± 0.4	111 ± 14	14.5 ± 0.4	101 ± 11
7.7 ± 0.4	53 ± 4	15.5 ± 0.4	80 ± 5
7.9 ± 0.4	103 ± 5	15.8 ± 0.4	89 ± 10
8.7 ± 0.4	160 ± 11	17.1 ± 0.4	66 ± 7
9.0 ± 0.4	142 ± 10	18.2 ± 0.4	60 ± 3
9.3 ± 0.4	256 ± 34		

Table 3.45: ^{156}Gd(p,n)^{156}Tb nuclear cross section data.

E [MeV]	σ [mbarn]	E [MeV]	σ [mbarn]
8.7 ± 0.4	No Signal	13.0 ± 0.4	288 ± 32
9.0 ± 0.4	No Signal	14.5 ± 0.4	482 ± 55
9.3 ± 0.4	No Signal	15.5 ± 0.4	605 ± 32
9.7 ± 0.4	No Signal	15.8 ± 0.4	522 ± 57
10.0 ± 0.4	No Signal	17.1 ± 0.4	648 ± 74
12.1 ± 0.4	202 ± 30	18.2 ± 0.4	670 ± 54

Table 3.46: ^{157}Gd(p,2n)^{156}Tb nuclear cross section data.

Erbium-165

E [MeV]	σ [mbarn]	E [MeV]	σ [mbarn]
5.8 ± 0.4	1.8 ± 0.4	13.0 ± 0.4	No Signal
7.7 ± 0.4	7 ± 1	14.1 ± 0.4	No Signal
8.7 ± 0.4	9 ± 1	14.5 ± 0.4	No Signal
9.7 ± 0.4	9 ± 1	15.2 ± 0.4	No Signal
10.4 ± 0.4	8 ± 3	15.8 ± 0.4	No Signal
11.1 ± 0.4	No Signal	16.5 ± 0.4	No Signal
11.5 ± 0.4	No Signal	17.1 ± 0.4	No Signal
12.1 ± 0.4	No Signal	18.2 ± 0.4	No Signal

Table 3.47: ^{164}Er(p,γ)^{165}Tm nuclear cross section data.

E [MeV]	σ [mbarn]	E [MeV]	σ [mbarn]
5.8 ± 0.4	No Signal	13.0 ± 0.4	349 ± 20
7.7 ± 0.4	No Signal	14.1 ± 0.4	467 ± 38
8.7 ± 0.4	No Signal	14.5 ± 0.4	618 ± 35
9.7 ± 0.4	No Signal	15.2 ± 0.4	680 ± 55
10.4 ± 0.4	0.9 ± 0.1	15.8 ± 0.4	752 ± 43
11.1 ± 0.4	21 ± 1	16.5 ± 0.4	835 ± 68
11.5 ± 0.4	56 ± 3	17.1 ± 0.4	870 ± 41
12.1 ± 0.4	210 ± 18	18.2 ± 0.4	1005 ± 56

Table 3.48: ^{166}Er(p,2n)^{165}Tm nuclear cross section data.

E [MeV]	σ [mbarn]	E [MeV]	σ [mbarn]
5.8 ± 0.4	No Signal	13.0 ± 0.4	No Signal
7.7 ± 0.4	No Signal	14.1 ± 0.4	No Signal
8.7 ± 0.4	No Signal	14.5 ± 0.4	No Signal
9.7 ± 0.4	No Signal	15.2 ± 0.4	No Signal
10.4 ± 0.4	No Signal	15.8 ± 0.4	No Signal
11.1 ± 0.4	No Signal	16.5 ± 0.4	No Signal
11.5 ± 0.4	No Signal	17.1 ± 0.4	No Signal
12.1 ± 0.4	No Signal	18.2 ± 0.4	18 ± 1

Table 3.49: ^{167}Er(p,3n)^{165}Tm nuclear cross section data.

E [MeV]	σ [mbarn]	E [MeV]	σ [mbarn]
5.1 ± 0.5	1.4 ± 0.2	12.1 ± 0.4	290 ± 26
5.8 ± 0.4	3.7 ± 0.3	13.0 ± 0.4	245 ± 15
6.8 ± 0.4	21 ± 2	14.1 ± 0.4	194 ± 17
7.7 ± 0.4	50 ± 6	14.5 ± 0.4	161 ± 10
8.7 ± 0.4	120 ± 11	15.2 ± 0.4	129 ± 11
9.7 ± 0.4	203 ± 13	15.8 ± 0.4	109 ± 7
10.4 ± 0.4	287 ± 25	16.5 ± 0.4	74 ± 7
11.1 ± 0.4	343 ± 30	17.1 ± 0.4	66 ± 3
11.5 ± 0.4	346 ± 21	18.2 ± 0.4	58 ± 4

Table 3.50: ^{166}Er(p,n)^{166}Tm nuclear cross section data.

E [MeV]	σ [mbarn]	E [MeV]	σ [mbarn]
5.1 ± 0.5	No Signal	12.1 ± 0.4	200 ± 14
5.8 ± 0.4	No Signal	13.0 ± 0.4	408 ± 30
6.8 ± 0.4	No Signal	14.1 ± 0.4	545 ± 47
7.7 ± 0.4	No Signal	14.5 ± 0.4	588 ± 62
8.7 ± 0.4	No Signal	15.2 ± 0.4	664 ± 57
9.7 ± 0.4	No Signal	15.8 ± 0.4	703 ± 45
10.4 ± 0.4	No Signal	16.5 ± 0.4	805 ± 45
11.1 ± 0.4	No Signal	17.1 ± 0.4	892 ± 60
11.5 ± 0.4	95 ± 25	18.2 ± 0.4	925 ± 63

Table 3.51: ^{167}Er(p,2n)^{166}Tm nuclear cross section data.

E [MeV]	σ [mbarn]	E [MeV]	σ [mbarn]
5.1 ± 0.5	0.09 ± 0.02	12.1 ± 0.4	0.9 ± 0.7
5.8 ± 0.4	0.17 ± 0.03	13.0 ± 0.4	0.7 ± 0.5
6.8 ± 0.4	0.6 ± 0.1	14.1 ± 0.4	0.8 ± 0.6
7.7 ± 0.4	1.0 ± 0.3	14.5 ± 0.4	0.8 ± 0.6
8.7 ± 0.4	1.5 ± 0.7	15.2 ± 0.4	0.9 ± 0.5
9.7 ± 0.4	1.2 ± 0.5	15.8 ± 0.4	1.2 ± 0.7
10.4 ± 0.4	1.7 ± 0.3	16.5 ± 0.4	1.1 ± 0.7
11.1 ± 0.4	0.9 ± 0.3	17.1 ± 0.4	0.7 ± 0.3
11.5 ± 0.4	0.9 ± 0.3	18.2 ± 0.4	0.8 ± 0.2

Table 3.52: ^{166}Er(p,γ)^{167}Tm nuclear cross section data.

E [MeV]	σ [mbarn]	E [MeV]	σ [mbarn]
5.1 ± 0.5	0.6 ± 0.1	12.1 ± 0.4	285 ± 43
5.8 ± 0.4	5 ± 1	13.0 ± 0.4	226 ± 47
6.8 ± 0.4	14 ± 4	14.1 ± 0.4	133 ± 2
7.7 ± 0.4	50 ± 10	14.5 ± 0.4	117 ± 13
8.7 ± 0.4	122 ± 12	15.2 ± 0.4	100 ± 10
9.7 ± 0.4	290 ± 44	15.8 ± 0.4	90 ± 10
10.4 ± 0.4	339 ± 49	16.5 ± 0.4	82 ± 8
11.1 ± 0.4	411 ± 84	17.1 ± 0.4	70 ± 13
11.5 ± 0.4	366 ± 74	18.2 ± 0.4	57 ± 8

Table 3.53: ^{167}Er(p,n)^{167}Tm nuclear cross section data.

E [MeV]	σ [mbarn]	E [MeV]	σ [mbarn]
5.1 ± 0.5	No Signal	12.1 ± 0.4	375 ± 28
5.8 ± 0.4	No Signal	13.0 ± 0.4	571 ± 73
6.8 ± 0.4	No Signal	14.1 ± 0.4	794 ± 186
7.7 ± 0.4	No Signal	14.5 ± 0.4	838 ± 189
8.7 ± 0.4	No Signal	15.2 ± 0.4	878 ± 188
9.7 ± 0.4	No Signal	15.8 ± 0.4	899 ± 134
10.4 ± 0.4	77 ± 1	16.5 ± 0.4	1000 ± 146
11.1 ± 0.4	116 ± 24	17.1 ± 0.4	1121 ± 111
11.5 ± 0.4	293 ± 62	18.2 ± 0.4	1204 ± 127

Table 3.54: ^{168}Er(p,2n)^{167}Tm nuclear cross section data.

E [MeV]	σ [mbarn]	E [MeV]	σ [mbarn]
5.1 ± 0.5	No Signal	12.1 ± 0.4	1.2 ± 0.7
5.8 ± 0.4	No Signal	13.0 ± 0.4	1.6 ± 0.8
6.8 ± 0.4	No Signal	14.1 ± 0.4	1.3 ± 0.1
7.7 ± 0.4	No Signal	14.5 ± 0.4	1.2 ± 0.6
8.7 ± 0.4	No Signal	15.2 ± 0.4	1.2 ± 0.4
9.7 ± 0.4	No Signal	15.8 ± 0.4	1.3 ± 0.3
10.4 ± 0.4	0.7 ± 0.2	16.5 ± 0.4	0.9 ± 0.1
11.1 ± 0.4	1.7 ± 0.8	17.1 ± 0.4	1.5 ± 0.5
11.5 ± 0.4	1.0 ± 0.4	18.2 ± 0.4	1.3 ± 0.2

Table 3.55: ^{167}Er(p,γ)^{168}Tm nuclear cross section data.

E [MeV]	σ [mbarn]	E [MeV]	σ [mbarn]
5.1 ± 0.5	1.3 ± 0.3	12.1 ± 0.4	118 ± 4
5.8 ± 0.4	3.1 ± 0.4	13.0 ± 0.4	82 ± 5
6.8 ± 0.4	16 ± 1	14.1 ± 0.4	79 ± 6
7.7 ± 0.4	60 ± 5	14.5 ± 0.4	65 ± 4
8.7 ± 0.4	103 ± 7	15.2 ± 0.4	53 ± 2
9.7 ± 0.4	145 ± 7	15.8 ± 0.4	55 ± 3
10.4 ± 0.4	184 ± 7	16.5 ± 0.4	49 ± 5
11.1 ± 0.4	166 ± 6	17.1 ± 0.4	43 ± 3
11.5 ± 0.4	153 ± 10	18.2 ± 0.4	37 ± 5

Table 3.56: ^{168}Er(p,n)^{168}Tm nuclear cross section data.

E [MeV]	σ [mbarn]	E [MeV]	σ [mbarn]
5.1 ± 0.5	No Signal	12.1 ± 0.4	No Signal
5.8 ± 0.4	No Signal	13.0 ± 0.4	No Signal
6.8 ± 0.4	No Signal	14.1 ± 0.4	No Signal
7.7 ± 0.4	No Signal	14.5 ± 0.4	No Signal
8.7 ± 0.4	No Signal	15.2 ± 0.4	No Signal
9.7 ± 0.4	No Signal	15.8 ± 0.4	No Signal
10.4 ± 0.4	No Signal	16.5 ± 0.4	10 ± 3
11.1 ± 0.4	No Signal	17.1 ± 0.4	30 ± 1
11.5 ± 0.4	No Signal	18.2 ± 0.4	185 ± 2

Table 3.57: ^{170}Er(p,3n)^{168}Tm nuclear cross section data.

E [MeV]	σ [mbarn]	E [MeV]	σ [mbarn]
5.1 ± 0.5	12 ± 5	12.1 ± 0.4	97 ± 38
5.8 ± 0.4	24 ± 6	13.0 ± 0.4	95 ± 17
6.8 ± 0.4	93 ± 19	14.1 ± 0.4	89 ± 38
7.7 ± 0.4	133 ± 62	14.5 ± 0.4	70 ± 19
8.7 ± 0.4	126 ± 32	15.2 ± 0.4	75 ± 36
9.7 ± 0.4	108 ± 15	15.8 ± 0.4	90 ± 29
10.4 ± 0.4	145 ± 30	16.5 ± 0.4	93 ± 22
11.1 ± 0.4	95 ± 23	17.1 ± 0.4	121 ± 34
11.5 ± 0.4	81 ± 19	18.2 ± 0.4	91 ± 41

Table 3.58: ^{170}Er(p,n)^{170}Tm nuclear cross section data.

List of Figures

List of Tables

PART

II

Selected Publications

1. **G. Dellepiane**, P. Casolaro, C. Favaretto, P. V. Grundler, I. Mateu, P. Scampoli, Z. Talip, N. P. van der Meulen and S. Braccini, *Cross section measurements of terbium radioisotopes for an optimized ^{155}Tb production with an 18 MeV medical PET cyclotron*, Applied Radiation and Isotopes, 184 (2022); 110175.

2. S. Braccini, T. S. Carzaniga, **G. Dellepiane**, P. V. Grundler, P. Scampoli, N. P. van der Meulen and D. Wüthrich, *Optimization of ^{68}Ga production at an 18 MeV medical cyclotron with solid targets by means of cross section measurements of ^{66}Ga, ^{67}Ga and ^{68}Ga*, Applied Radiation and Isotopes, 186 (2022); 110252.

3. **G. Dellepiane**, P. Casolaro, I. Mateu, P. Scampoli, N. Voeten and S. Braccini, *^{47}Sc and ^{46}Sc cross section measurements for an optimized ^{47}Sc production with an 18 MeV medical PET cyclotron*, Applied Radiation and Isotopes, 189 (2022); 110428.

4. **G. Dellepiane**, P. Casolaro, I. Mateu, P. Scampoli, N. Voeten and S. Braccini, *Cross section measurements for an optimized ^{61}Cu production at an 18 MeV medical cyclotron from natural Zn and enriched ^{64}Zn solid targets*, Applied Radiation and Isotopes, 190 (2022); 110466.

5. **G. Dellepiane**, P. Casolaro, I. Mateu, P. Scampoli and S. Braccini, *Alternative routes for ^{64}Cu production using an 18 MeV medical cyclotron in view of theranostic applications*, Applied Radiation and Isotopes, 191 (2023); 110518.

6. **G. Dellepiane**, P. Casolaro, A. Gottstein, I. Mateu, P. Scampoli and S. Braccini, *Study of ^{67}Cu optimized production based on cross section measurements of ^{67}Cu and ^{64}Cu using an 18 MeV medical cyclotron*, Applied Radiation and Isotopes, 195 (2023); 110737.

Funding Sources

This research was financially supported by the Swiss National Science Foundation by means of the sinergia project

PHOtonuclear Reactions (PHOR): Breakthrough Research in Radionuclides for Theranostics.

Grant CRSII5 180352

Declaration of consent

on the basis of Article 18 of the PromR Phil.-nat. 19

Name/First Name: Dellepiane Gaia

Registration Number: 18-136-838

Study program: Doktorat PHIL-NAT

Bachelor ☐ Master ☐ Dissertation ☑

Title of the thesis: New Radionuclides for Theranostics at the Bern Medical Cyclotron

Supervisor: Prof. Dr. Saverio Braccini

I declare herewith that this thesis is my own work and that I have not used any sources other than those stated. I have indicated the adoption of quotations as well as thoughts taken from other authors as such in the thesis. I am aware that the Senate pursuant to Article 36 paragraph 1 litera r of the University Act of September 5th, 1996 and Article 69 of the University Statute of June 7th, 2011 is authorized to revoke the doctoral degree awarded on the basis of this thesis.
For the purposes of evaluation and verification of compliance with the declaration of originality and the regulations governing plagiarism, I hereby grant the University of Bern the right to process my personal data and to perform the acts of use this requires, in particular, to reproduce the written thesis and to store it permanently in a database, and to use said database, or to make said database available, to enable comparison with theses submitted by others.

Bern, 07.02.2023

Place/Date

Signature